ISSN : 2582-7405

Transaction on Biomedical Engineering Applications and Healthcare

Volume No. 6

Issue No. 2

May - August 2025

ENRICHED PUBLICATIONS PVT. LTD

JE-18, Gupta Colony, Khirki, Extn, Malviya Nagar, New Delhi-110017
PHONE : - + 91-8877340707
E-Mail : info@enrichedpublications.com

ISSN : 2582-7405

Transaction on Biomedical Engineering Applications and Healthcare

Aims and Scope

The primary objective of the **Transaction on Biomedical Engineering Applications And Healthcare journal,** popularly known as the TBEAH journal, is to serve as a comprehensive, open-access platform that is dedicated solely to facilitating the progress and advancement of the field of Biomedical Engineering by -

offering gifted and talented researchers engaged within the domain of Biomedical Engineering a unique setting for them to get their work published and elevate their reputations/standing within the global community, as well as,

providing professionals, students, academics, and scholars free access to the latest and most advanced research outcomes, findings, and studies, being carried out in the field of Biomedical Engineering, all across the world.

Subject Area

RELATED TOPICS:

1. Biomedical signal processing
2. Biomedical imaging and image processing
3. Bioinstrumentation
4. Biosensors
5. Bio-micro/nano technology
6. Bioinformatics and Computational Biology
7. Biomedical modeling and computing
8. Cardiovascular Engineering
9. Neural and Rehabilitation Engineering
10. Biomechanics
11. Robotics
12. Therapeutic and diagnostic systems, devices and technologies
13. Clinical Engineering
14. Healthcare information systems and telemedicine
15. Other emerging topics in biomedical engineering

ISSN : 2582-7405

Editor-in-Chief

Managing Editor

Editorial Board Members

ISSN : 2582-7405

ISSN : 2582-7405

Transaction on Biomedical Engineering Applications and Healthcare

(Volume No. 6, Issue No. 2, May - August 2025)

Contents

ISSN : 2582-7405

Comparison of Propagation Models and Forward Calculation Methods on Cellular, Tissue and Organ Scale Atrial Electrophysiology

Claudia Nagel , Cristian Barrios Espinosa Gernot Plank , Olaf Dössel , Karli Gillette, Matthias A.F. Gsell , and Axel Loewe , Jorge Sánchez , Senior Member, IEEE

ABSTRACT

Objective: The bidomain model and the f inite element method are an established standard to mathematically describe cardiac electrophysiology, but are both suboptimal choices for fast and large-scale simulations due to high computational costs. We investigate to what extent simplified approaches for propagation models (monodomain, reaction-Eikonal and Eikonal) and forward calculation (boundary element and infinite volume conductor) deliver markedly accelerated, yet physiologically accurate simulation results in atrial electrophysiology. Methods: We compared action potential durations, local activation times (LATs), and electrocardio grams (ECGs) for sinus rhythm simulations on healthy and f ibrotically infiltrated atrial models. Results: All simplified model solutions yielded LATs and P waves in accurate accordance with the bidomain results. Only for the Eikonal modelwithpre-computedactionpotential templates shifted in time to derive transmembrane voltages, repolarization behavior notably deviated from the bidomain results. ECGs calculated with the boundary element method were characterized by correlation coefficients >0.9 compared to the finite element method. The infinite volume conductor method led to lower correlation coefficients caused predominantly by systematic overestimations of P wave amplitudes in the precordial leads. Conclusion: Our results demonstrate that the Eikonal model yields accurate LATs and combined with the boundary element method precise ECGs compared to markedly more expensive full bidomain simulations. However, for an accurate representation of atrial repolarization dynamics, diffusion terms must be accounted for in simplified models. Significance: Simulations of atrial LATs and ECGs can be notably accelerated to clinically feasible time frames at high accuracy by resorting to the Eikonal and boundary element methods.

Index Terms—Atrial electrophysiology, bidomain, eikonal, electrocardiograms, finite element method, local activation times, monodomain, P waves.

I. INTRODUCTION

IN COMPUTATIONAL cardiac modeling, the bidomain model is the most biophysically detailed formulation to compute the spread of the de- and repolarization wavefront and the electrical source distribution throughout the cardiac tissue. Furthermore, the finite element method is considered the gold standard for computing the body surface potentials from a given distribution of the electrical

sources in the heart to extract electrocardiograms (ECG) at standardized electrode positions. However, both methods are computationally expensive and are thus suboptimal for generating large in silico datasets of cardiac signals for machine learning applications [1], [2], or for efficiently simulating excitation propagation in cardiac digital twin for certain clinical applications such as to guide ablation therapy[3].Hence,simplifiedmodelswithfastsolutiontimesare needed to speed up the generation of in silico datasets of cardiac signals, such as local activation times (LATs), electrograms or ECGsbyseveralordersofmagnitude[4]–[6].Yet,thesignalsobtained with these simplified methods need to be physiologically accurate and resemble the results obtained with the bidomain and f inite element method.In this work,we therefore aim to quantify the inaccuracies arising in simulated atrial signals when resorting to simplified computational methods. While comparisons of this type have already been performed for the ventricles [5], [7] and partly also for four chamber heart models [8], a study focusing on atrial electrophysiology is lacking to the best of our knowledge. However, this is substantial since the atria stand out by a highly complex myocardial fiber structure, locally heterogeneous properties regarding ion channel and tissue conductivities and higher anisotropy ratios as compared to the ventricles.

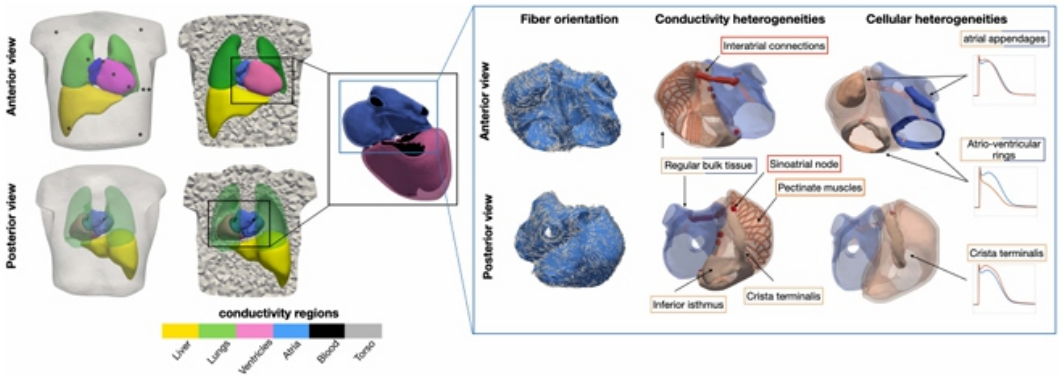

Fig. 1. Torso model with the segmented organs and electrode positions (transparent and clipped views) from the anterior and posterior view in the top and bottom row, respectively. The right panel shows the anatomically detailed atrial model that was augmented with fiber orientation and labels for anatomical structures. Heterogeneous conductivity and ionic properties were assigned to spatially distinct regions in the mesh. Resulting APs featuring ionic heterogeneity are depicted on the right side in red together with the baseline Courtemanche et al. cellular model in blue.

The mono domain, reaction-Eikonal (RE), and the Eikonal model solved by the fast iterative method constitute the simplified propagation models investigated in this work. Forward calculation techniques applied in this study comprise the boundary element and the infinite volume conduct or methods. Simulations were carried out in sinus rhythm with and without the inclusion of fibrotic tissue modeled as passive conduction barriers [9], slow conducting tissue patches and rescaled ion channel conductivities representing cytokine effects [10], [11]. We assess the errors between simplified propagation models and forward calculation methods to the gold standard bidomain and finite element formulations with metric sextracted from the simulation results on cellular, tissue and organ scale comprising APDs, LATs, and ECGs, respectively.

II. METHODS

A. Model Generation

An anatomically detailed model of the torso was obtained by multi-label magnetic resonance image segmentation as described in [12]. The contours of atria, ventricles, lungs, liver and torso were exported as triangular surface meshes. These were smoothed and resampled with an average edge length of 0.5 mm, 5 mm, 5 mm, 7 mm and 15 mm, respectively, using Meshmixer (Autodesk, San Rafael, CA, USA) and Instant Meshes [13] whereby details were corrected manually in Blender (Blender Foundation, Amsterdam, The Netherlands) to avoid intersecting segments and ensure a sufficient mesh quality and topology. The segmented atrial endocardial surfaces were fed into the pipeline described in [10], [14], [15] to obtain a volumetric tetrahedral bi-atrial geometry with a homogeneous wall thickness of 3 mm and an average edge length of 523 μm augmented with inter-atrial connections, labels for anatomical structures and myocardial fiber orientation. In contrast to fully personalized approaches where fiber orientation can be defined based on information extracted from diffusion tensor imaging data, we defined myocardial fiber architecture in a rule-based way as described in [14] building on the solution of Laplace's [16], [17]. Meshtool [18] was used to generate a tetrahedral model of the full torso while preserving the surfaces of the considered organs.Tags for the atrial and ventricular blood pools were allocated to all elements in the volumetric torso model located inside the surfaces bounded by the atrial and ventricular endocardial walls with closed valve and vein orifices. A detailed view of the torso and atrial model is depicted in Fig. 1.

Isotropic extracellular conductivityof0.0389S/m,0.028S/m, 0.06 S/m, 0.7 S/m and 0.22 S/m was assigned to lungs, liver, ventricles, atrial and ventricular blood pools and the remaining torsotissue,respectively,asreportedinpreviouswork[19]–[21].

In order to conduct comparable experiments with the mono or bidomain model that require conductivities, and the Eikonal based models that resort instead to conduction velocities (Cvs), it is crucial to consistently associate conductivities and Cvs for all heterogeneous tissue regions in the atria. Therefore, anisotropic and locally heterogeneous conductivities were assigned to five different regions in the atria comprising regular bulktissue, cristaterminalis,pectinatemuscles,inferioristhmus, and inter-atrial connections. Cvs corresponding to the mono domain conductivities reported in [22] for 0.33 mm resolution voxel models were therefore first calculated as described in [23]. Using tune CV [24], [25], intra- (σi) and extracellular (σe) conductivities as well as the mono domain conductivities (σm) were iteratively optimized for the tetrahedral mesh setup described above while keeping the $\sigma i/\sigma e$ ratio fixed. For this purpose, five strand geometries with a length of 10 cm generated each characterized by a resolution corresponding to the average edge length of one of the hetero geneous conductivity regions in the atria. Intra- and extracellular conductivities in longitudinal and transversal fiber direction as

reported by Clerc et al. [26] as well as by Roberts et al. [27] were initially assigned to the elements in the slab meshes. In an iterative optimization procedure, the conductivities were adjusted until the CV converged to the target value derived from [22]. In this way, the originally reported intra- and extracellular conductivity values were scaled while the ratios between them were kept constant along the eigenaxes [25]. In the following, we refer to the tuned conductivities obtained byinitially assigning the values reported by Clerc [26] and Roberts et al. [27] to the slab meshes as Clerc and Roberts conductivities, respectively. The resulting heterogeneous and anisotropic conductivity setup for each atrial region is summarized in Table SI in the supplementary material. For the monodomain simulations, we considered two different cases which we refer to as "monodomain with and without explicit conductivity tuning". For the first one, we repeated the tuneCV optimization using the monodomain propagation model and obtained the monodomain conductivities listed in Table SI in the supplementary material. In the second case, we directly computed the monodomain conductivities from the tuned intra- and extracellular bidomain conductivities as half their harmonic mean.

The Courtemanche et al. cell model [28] was used in the simulations described in Section II-B. To reflect regionally heterogeneous electrophysiology, maximum ion channel conductances were rescaled compared to the baseline model as reported in previous work [22], [29] and are summarized in Table SII in the supplementary material. The final CV values in longitudinal and transversal fiber direction as used for the Eikonal and RE simulations described in Section II-B were subsequently calculated with tuneCV [24] based on the tissue and ion channel conductivity settings in each atrial region.

B. Propagation Models

1) Bidomain Model: The bidomain model represents the propagation of the electrical de- and repolarization wavefront through the cardiac tissue [30]–[32]. Here, the intracellular and extracelullar domains are coupled and intertwined in a system of partial differential equations. Solving this system provides at each point in the cardiac tissue the intracellular Φi and extracellular Φe electrical potentials:

$$-\nabla \cdot ((\sigma_i + \sigma_e)\nabla \Phi_e) = \nabla \cdot (\sigma_i \nabla V_m) \quad (1)$$

$$\nabla \cdot (\sigma_i \nabla V_m) + \nabla \cdot (\sigma_i \nabla \Phi_e) = \beta \left(C_m \frac{\partial V_m}{\partial t} + I_{ion} - I_s \right) \quad (2)$$

where Vm = φi −φe is the transmembrane potential σi and σe are the intracellular and extracellular conductivity tensors, respectively, β is the surface to volume ratio of the membrane, and Cm is the membrane capacitance per unit surface. Additionally, Is and Iion are the transmembrane stimulus and ionic currents, respectively. The ionic current Iion depends on the state variables η that are calculated

with a non-linear system of ordinary differential equations. To solve the bidomain equation, wedefined areference electrode on the anterior, lower left hand side of the torso. Homogeneous Neumann boundary conditions were imposed at the boundaries of the myocardial tissue (intraand extracellular domains) and the torso (extracellular domain). At the myocardial tissue to torso interface, φe is constrained be continuous and no-flux is enforced in the normal direction n for φi:

$$\vec{n} \cdot \sigma_i \nabla \phi_i = 0 \qquad (3)$$

Also at the boundary of the torso that is not in contact with the myocardial tissue, a no-flux boundary condition for φe is imposed:

$$\vec{n} \cdot \sigma_b \nabla \phi_e = 0 \qquad (4)$$

where σ b is the conductivity of the bath (torso).Additionally, the continuity of the normal component of the extracellular current (5) and φe at the tissue-bath interface (6) is enforced:

$$\sigma_e \nabla \phi_e \cdot \vec{n} = \sigma_b \nabla \phi_e \cdot \vec{n} \qquad (5)$$

$$\phi_e|_e = \phi_e|_b \qquad (6)$$

Initial conditions of the model were defined by the state variables of the cell modelspacedtoalimitcycleat1Hz.Numerical methods used to solve the bidomain model equations rely on high resolution meshes which is the main cause of the model's high computational cost [33]. Nonetheless, the bidomain model is considered the most accurate of the available cardiac models for tissue level electrophysiology.

2) Monodomain Model: Assuming that the intra- and extracellular conductivity tensors are proportional, i.e. their anisotropic ratios are equal, the bidomain model can be significantly reduced to the monodomain model [31]–[33]:

$$\beta C_m \frac{\partial V_m}{\partial t} = \nabla \cdot (\sigma_m \nabla V_m) - \beta (I_{ion}(V_m, \eta) - I_s) \qquad (7)$$

where σm is the monodomain conductivity tensor. This tensor can be expressed in terms of half the harmonic mean of intraand extracellular conductivity tensors:

$$\sigma_m = \frac{\sigma_i \sigma_e}{\sigma_i + \sigma_e} \qquad (8)$$

The assumption of equal anisotropy does not fully hold in reality. However, this model still offers a close approximation of the wave propagation. [8]. For a planar wave moving along the f iber directions monodomain and bidomain models are exactly equivalent. The extracellular potential field Φe can be approximated from the monodomain transmembrane potentials as a source model by solving the

elliptic bidomain (1) at a temporally coarser scale. However, the volume conductor cannot influence the transmembr anevoltaged is tribution in this approach and bath loading effects are ignored.This concept is referred to a spseudo bidomain approach [7] and is computationally only marginally more expensive than a standard monodomain simulation. The monodomain and bidomain models can be discretized in space using different approaches [34]. For this study, we used the finite element method [24].

3) Eikonal Model: The Eikonal model is based on the macroscopic kinetics of the wavefront propagation [5], [31], [32], [35]. Solving the Eikonal equation seeks to find the activation times T for each node x based on a local speed function:

$$\sqrt{\nabla T(x)^\top M \nabla T(x)} = 1, \tag{9}$$

$$T(x) = T_0 \text{ for } x \in \Gamma, \tag{10}$$

Where M is the squared CV tensor and T0 are the initial conditions for the activation sites Γ. Although Vm is not directly calculated in this model, it can be inferred from the activation times:

$$V_m(x,t) = U(x, t - T(x)) \tag{11}$$

where U is an AP timecourse. It was obtained based on a simulation of a planar wavefront propagating in a tissue block from which the transmembrane potential Vm was extracted at a node in the center of the mesh. Specific AP timecourse were used in different anatomical regions. Numerical simulations are significantly faster because of the simplicity of the equation and lower resolution meshes that are required. Unfortunately, the Eikonal model fails to accurately represent the influence of bath loading effects, high wavefront curvatures, reentry, and wave-collisions on CV. [5], [36]. In the case of complex patterns of activation that occur for example during atrial fibrillation, these limitations become more significant. Nonetheless, these simulations still provide a decent approximation of wave propagation under healthy conditions. In these case, the shortcomings of the Eikonal model are still present but their effects are less pronounced.

4) Reaction-Eikonal Model: When applied to coarse meshes,the mono-and bidomain models both exhibits lowed CV for a given tissue conductivity [5], [34]. The general RE model uses the activation times obtained by the Eikonal model to enable biophysical models to calculate the trans membrane potential in coarsemeshes[5].Theresolutionrequirementisrelaxedbecause the thin wave front does not need to be explicitly represented.The RE model calculates an Ifoot current to replicate the activating effect of the diffusion term on neigh boring cells and applies it to the reaction model at the time given by the Eikonal solution. In this work, only the RE+ version of the model is considered (12), in which the Ifoot current is added to the diffusion term instead of replacing it.

$$\beta C_m \frac{\partial V_m}{\partial t} = \nabla \cdot (\sigma_m \nabla V_m) + I_{foot} - \beta(I_{ion}(V_m, \eta)) \quad (12)$$

Thus, the activation of the nodes can be achieved by either the diffusion term or the I foot current and neighboring nodes also interact during repolarization. The RE+ variant is more accurate when comparing to the mono domain model in coarse meshes and the repolarization gradients are significantly smoother. However, RE models are unable to activate the same node several times (as for example required for simulations of reentry) and share the limitations of the standard Eikonal model regarding the influences of wavefront curvature, source sink mismatch and bath loading on CV.

C. Forward Calculation Methods

When modeling the torso as a passive volume conductor, the bidomain formulation can be reduced to its parabolic part to solve the forward problem of electrocardiography for a given distribution of Vm. The Poisson equation in (1) can be solved numerically by discretizing the full torso domain with finite elements (finite element method). To comply with the terminology in related work [37], we use the term finite element method (FEM) in the following when referring to solving Poisson's (1) numerically using a finite element discretization scheme even though this discretization scheme was also used to solve for example the bidomain equations. Standard extracellular conductivities were hereby assigned to different organs as described in Section II-A. By assuming isotropic myocardial properties in the extracellular space, a reduced set of dipole sources can be mapped onto the surfaces bounding the organs with different conductivity properties. Then, the boundary element method can be used for computing the body surface potentials and the ECG. In the latter case, applying Green formulas and boundary conditions as well as assuming equal anisotropy ratios in the intra- and extracellular domain allow for reformulating (1) as a surface integral to compute the extracellular potential Φ at any point r on the torso surface:

$$\Phi(\vec{r}) \approx 2 \cdot \Phi^{\infty}(\vec{r}) - \frac{1}{2\pi} \sum_{k=1}^{K} \frac{\sigma_-^k - \sigma_+^k}{\sigma_T} \int_{S^k} \Phi(\vec{r'}) \frac{(\vec{r} - \vec{r'})}{|\vec{r} - \vec{r'}|^3} d\vec{S'}, \quad (13)$$

whereby the minuend describes the potentials attributable to the sources in an unbounded medium with conductivity σT.The subtrahend in (13) accounts for secondary sources introduced by the bounded volume conductor. σk − and σk + characterize the conductivities inside and outside the respective surface Sk.The potential Φ∞ can be expressed either using the transmembrane voltage distribution on the cardiac surface [38] or the primary impressed currents Jp [39] as volumetric sources inside the bounded volume conductor Vh:

$$\Phi^{\infty}(\vec{r}) = \frac{1}{4\pi\sigma_T} \int_{V_h} \frac{\vec{J_p} \cdot (\vec{r} - \vec{r'})}{|\vec{r} - \vec{r'}|^3} dV_h \quad (14)$$

When computing the ECG using the infinite volume conductor method (IVC), the heart is assumed to be immersed in a medium of infinite spatial extent with a homogeneous conductivity σT. This reflects in the sum over the surface integrals in (13) being neglected for calculating extracellular potentials on the torso surface:

$$\Phi(\vec{r}) \approx \Phi^{\infty}(\vec{r}) \qquad (15)$$

D. Simulation Scenarios

Simulations were carried out on the bi-atrial volumetric model described in Section II-A in sinus rhythm with and without the inclusion of fibrotic tissue patches. For the former case, several elliptically shaped patches with their principal axis aligned to the macroscopic atrial fiber orientation were manually defined predominantly on the posterior wall of the left atrium and the left pulmonary vein antrum as reported by Highuchi et al. [40]. These regions extended transmurally and are shown in Fig. 2. To not only account for the patchiness of atrial fibrosis but also for its diffuse deposition, 80% of the cells within the elliptical patches were definedasfibrotic. In this way, the volume fraction of left atrial fibrosis quantified to 22 % of the total left atrial tissue volume. Remodeled conduction properties were assigned the fibrotic regions in three different ways: In the first case, f ibrotic elements were removed fromtheatrial mesh and instead assigned to the extracellular domain following the concept of percolation [9]. In this way, we introduced passive conduction barriers that do not have a trans membrane voltage and thus do not

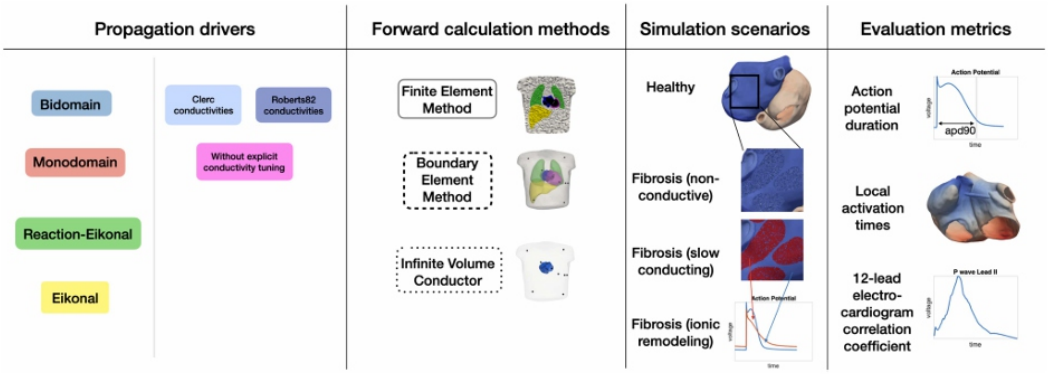

Fig. 2. Overview of the different propagation models, forward calculation methods, simulation scenarios and evaluation metrics used in this work.

contribute to the electrical source distribution on the myocardial tissue surface. In the second case, fibrotic regions were characterized as slow conducting patches with CVsreducedby80%in transversal and 50 % in longitudinal fiber direction compared to the healthy baseline case. Conductivities in these regions were obtained as described in Section I. In this way, anisotropy ratios were increased by a factor of 2.5 in fibrotic areas promoting wave propagation along myocardial fiber orientation and thus forming the basis for functional reentry circuits. In the third case, ionic properties of the fibrotic cells were remodeled by rescaling the conductances of the sodium (gNa), the calcium (gCaL)and the inward

rectifier potassium current (gK1) by a factor of 0.6, 0.5 and 0.5, respectively, compared to the baseline conductances of the Courtemanche et al. cell model to account for cytokine remodeling effects [11].

Sinus rhythm simulations were initiated at a sinus node exit site located at the junction of crista terminalis and the superior venacava.We obtain the transmembrane voltage distribution for the LATs computed with the Eikonal model as describedin(11), whereby the respective ionic model parameters in each region as listed in Table SII in the supplementary material were taken into account for calculating the AP templates.

The Cardiac Arrhythmia Research Package (CARP) [41] and openCARP [24] were used for computing the spread of the depolarization wave with different propagation model saswellas ECGswith the finite element and the infinite volume conductor method. The algorithms described by Stenroos et al. [39] were used for calculating ECGs with the boundary element method. As recommended by Schuler et al. [42], we downsampled the surface mesh bounding the atria to a resolution of 2.5 mm for computing the transfer matrix. Furthermore, we applied Laplacian smoothing to the transmembrane voltage sources to ensure a continuous wave propagation on the coarse mesh.

E. Evaluation Metrics

Fromthe source distribution obtained from simulations using different propagation models, we calculated APDs at 90 % repolarization (APD90) for each node in the mesh. Also at each vertex in the geometry, we extracted LATs defined as the timestep with the steepest AP upstroke. For both, APDs and LATs, the accuracy of each propagation model simulation was quantified as the absolute difference to the respective value for each metric obtained from the bidomain simulation with the Clerc conductivities.

To assess fidelity of simplified forward calculation methods along with different propagation models, we evaluated the Pearsoncorrelation coefficient of the respective ECGresultswiththe ECGs obtained by solving the forward problem with the finite element method based on the bidomain source model with the Clerc conductivities.

III. RESULTS

A. Propagation Models

The effect of different propagation models on the activation sequence(LATs)isvisualized inFig. 3.Thetotalactivation time in the healthy references cenario solved with the bidomain model was 102 ms. In the top panel, the distributions of the signed differences between the examined propagation models' LATs and the bidomain results obtained with Clerc conductivity ratios evaluated at all mesh nodes are visualized as violin plots. In the bottom panel, the difference to the bidomain results are

mapped onto the atrial geometry. The mismatch in LATs was most pronounced for the bidomain scenario with Roberts conductivities and much smaller for the simplified propagation models. For the Roberts conductivity ratios, the LATs were systematically smaller than the ones resulting from the reference bidomain simulation with the Clerc conductivity settings. Furthermore, the error increased with the spread of the depolarization wave front leading to small deviations close to the sinus node exit site, but errors of up to −14 ms at the latest activated areas at the posterior wall of the left atrium and the coronary sinus in the right atrium. The mean and standard deviation of the absolute errors between the bidomain and monodomain LATs with and without explicit conductivitiy tuning were 0.93 ± 0.61 ms and 1.02 ± 0.64 ms. With the temporal resolution of the sampled simulated myocyte APs being 1 ms and the LATs being calculated as the point in time marking the steepest Apupstroke, in particular the LAT results for the monodomain simulation

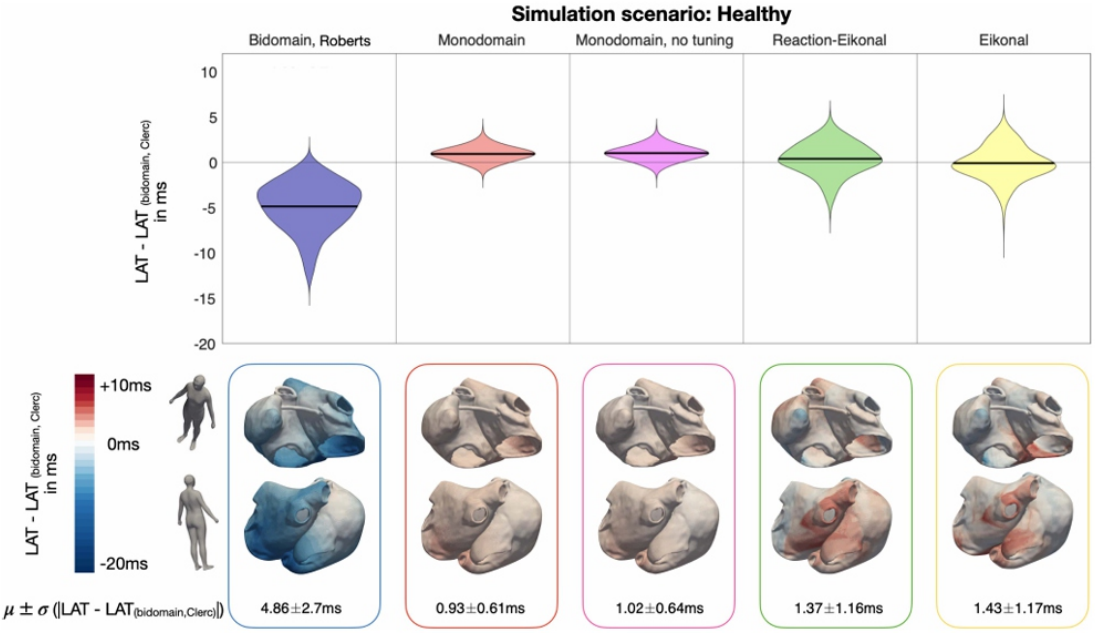

Fig. 3. Local activation time (LAT) results in sinus rhythm for healthy (non-fibrotic) tissue for different propagation models. The top panel shows the distribution of the signed LAT differences taking the bidomain simulations executed with the Clerc conductivity ratios as a reference. From left to right, the violin plots show the results for the bidomain (Roberts conductivities), the monodomain (with and without explicit conductivity tuning), the RE^{+} and the Eikonal simulations. The bottom panel shows the signed LAT differences mapped on the atrial geometry for each propagation model in the above order. Mean and standard deviation of the absolute LAT differences are shown in the bottom row for each case.

with additional conductivity tuning were below the accuracy with which the LATs were determined. RE+ and Eikonal LAT differences quantified to 1.37 ± 1.16 ms and 1.43 ± 1.17 ms, respectively. The signed LAT error to the bidomain results was distributed similarly across the atrial tissue among these two propagation models (see Fig. 3 bottom panel). The LAT results in the simulation scenarios involving fibrosis remodeling were only slightly different compared to the sinus rhythm results depicted in Fig. 3. The largest differences occurred for the Eikonal propagation model in the simulations cenario where fibrosis was modeled as slow conducting tissue. There, the absolute error to the bidomain results quantified to 1.71 ± 1.46 ms compared to 1.43 ± 1.17 ms in sinus rhythm without the inclusion of fibrosis.

APD90 results are visualized for the simulation scenario with f ibrosis modeled as ionic conductance rescaling in Fig. 4.For the monodomain simulations, the mean and standard deviation of the absolute APD90 discrepancies to the bidomain results obtained with Clerc conductivity ratios were below the temporal resolution of the AP time course of 1 ms. Absolute errors to the bidomain simulation with Roberts conductivity ratios and the RE+ results quantified to 2.92 ± 3.07 ms and 1.13 ± 1.69 ms, respectively. In both cases, the highest errors occurred in regions around the fibrotic tissue patches. APD90 results for the Eikonal simulation were characterized by an absolute error to the bidomainsimulationresultsof25.1±20.72ms.Furthermore,theAP signal trace obtained from a tissue strand simulation and used as a template to infer the transmembrane voltage distribution for the Eikonal LATs is visually clearly distinguishable from the bidomain AP especially in fibrotic regions (see Fig. 4 bottom panel).

ECGs obtained from the transmembrane voltaged is tributions from the simulation scenario with fibrosis modeled as ionic rescaling as depicted in Fig. 4 and using the boundary element forward calculation method are visualized in Fig. 5. The 12-lead ECG is displayed for a duration of 650 ms whereby the signal sections in the interval [0 ms, 150 ms] and [150 ms, 650 ms] represent the P wave and the atrial repolarization, respectively. The latter is typically not visible in the ECG of a full heartbeat since the repolarization phase of the atria temporally coincides with the ventricular activation and the respective signal parts are thus buried within the QRS complex.

The observed discrepancies in the AP signal course between the bidomain and Eikonal simulation also reflects in the ECG. As can be seen in Fig. 5, the repolarization signal obtained with the Eikonal and bidomain propagation modeldiffer. In lead aVL, the polarity of the repolarization wave was even inverted. Apart from the atrial repolarization ECG signal obtained with the Eikonal model and precomputed AP templates, the choice of the propagation model did not markedly influence the ECG as the remaining signals in Fig. 5 show only minor differences. Furthermore, the correlation coefficients between the bidomain ECG obtained with the Clerc conductivity ratios and the other examined propagation models are summarized in Table I for the

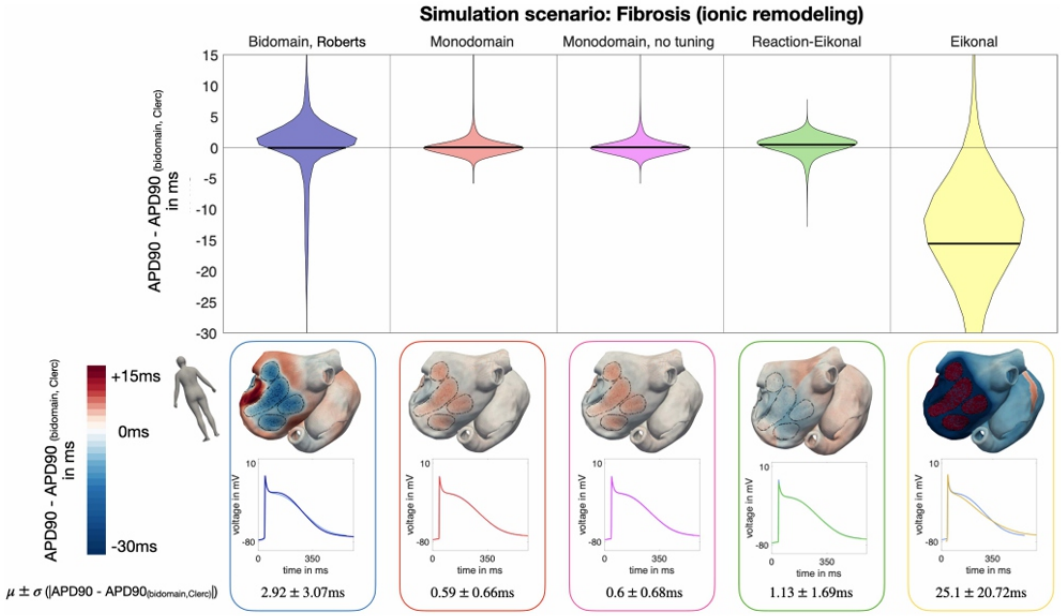

Fig. 4. APD_{90} results in sinus rhythm with fibrotic substrate replacing 22% of the left atrial myocardial tissue modeled as rescaled ionic conductances. The violin plots in the top panel represent the distribution of APD_{90} discrepancies to the bidomain results for all investigated propagation models. In the bottom panel, the signed APD_{90} differences are mapped onto the atrial geometry. Fibrotic regions are encircled with black dashed lines. The APs are shown for one node within the fibrotic area on the posterior left atrial wall. Bidomain APs are visualized in light blue, the other signal trace was obtained with the respective propagation model. The numbers in the bottom line show the mean and standard deviation of absolute APD_{90} differences with respect to the bidomain simulation results.

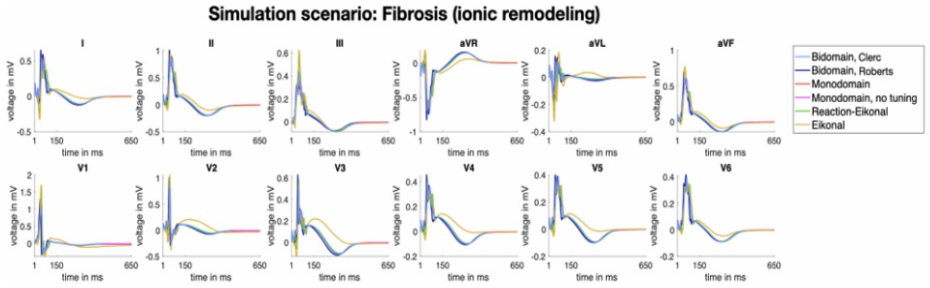

Fig. 5. ECGs calculated with the same forward calculation method (BEM) but different propagation models (color coded) with the transmembrane voltages resulting from the simulation scenario with fibrosis modeled as ionic conductivity rescaling.

TABLE I

CORRELATION COEFFICIENTS BETWEEN THE ECGS OBTAINED WITH THE BIDOMAIN AND SIMPLIFIED PROPAGATION MODELS WHEN SOLVING THE FORWARD PROBLEM WITH BEM. COLUMNS REPRESENT DEPOLARIZATION (P WAVE), REPOLARIZATION AND THE ENTIRE SIGNAL

	[0 ms, 150 ms]	[150 ms, 650 ms]	[0 ms, 650 ms]
Bidomain, Clerc	1	1	1
Bidomain, Roberts	0.8590	0.9904	0.9028
Monodomain	0.9942	0.9998	0.9961
Monodomain, no tuning	0.9931	0.9998	0.9954
Reaction-Eikonal	0.9211	0.9953	0.9428
Eikonal	0.9203	0.6233	0.8791

intervals [0 ms, 150 ms] (Pwave),[150ms,650ms](repolariza tion) and [0 ms, 650 ms]. The lowest correlation coefficient for the P wave occurred for the bidomain simulation with Roberts conductivity ratios. For all simplified propagation models, the P wave correlation coefficients were above 0.92. Except for the Eikonal model, the correlation coefficient of the ECG signal sections representing the repolarization phase wave was above 0.99. ECG and APD90 results only marginally differed for the remaining fibrosis remodeling scenarios as detailed and visualized in the figures S6-S10 in the

supplementary material.

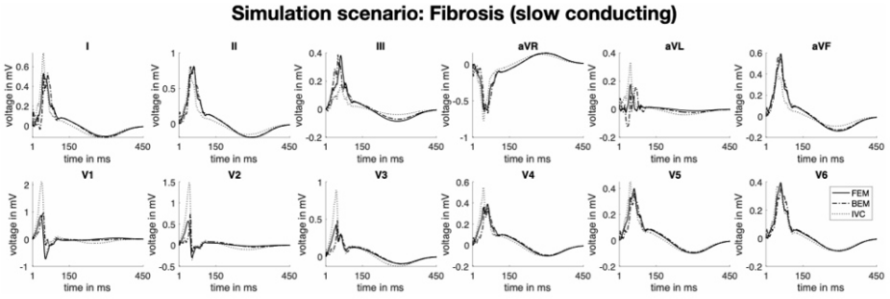

Fig. 6. ECGs calculated the same source distribution resulting from a bidomain simulation with Clerc conductivity ratios and with different forward calculation methods in the simulation scenario with fibrosis modeled as slow conducting tissue. ECGs calculated with the finite element method (FEM), the boundary element method (BEM) and the infinite volume conductor method (IVC) are visualized with the solid, dash-dotted and dotted lines, respectively.

B. Forward Calculation Methods

ECGs calculated with different forward calculation methods based on the same source distribution stemming from the bidomain simulation with Clerc conductivity ratios are depicted in Fig. 6 for the simulation scenario with fibrosis modeled as slow conducting tissue.The correlation coefficients covering the ECG signal parts of the P wave between the gold standard FEM approach and each of the BEM and IVC method quantified to 0.94 and 0.83 for fibrosis modeled as slow conducting tissue. Especially the IVC method yielded too high ECGs in the precordial leads and inaccurately captured atrial repolarization in the inferior leads II, III and aVF.

IV. DISCUSSION

A. Main Findings

In this work, we compared atrial APD90, LATs and ECGs computed with the bidomain, monodomain, RE+ and the Eikonal propagation models as well as with the finite element, the boundary element and the infinite volume conductor forward calculation methods. The largest deviations in LATs were observed between the bidomain simulations with Clerc and Roberts conductivity ratios. As the absolute LAT errors increase with the propagating wavefront, discrepancies in LATs can be traced back to more pronounced bath loading effects occurring in the Roberts conductivity settings. With a higher ratio between extracellular bulk and isotropic bath conductivities, the depolarization wave propagates faster in close vicinity to the interface between blood pool and endocardial wall leading to earlier LATs throughout the cardiac tissue. Due to the thin atrial wall, the bathloading effect is visible transmurally and thus leads to globally faster conduction velocities in the bidomain simulation with the Roberts conductivity setup. However, in this work, conductivities were tuned as described in Section II-A without a bath attached to one face of the strand meshes. Incorporating the bath already in the tuning process would have led to more similar results between the bidomain simulation results obtained with tuned Clerc and Roberts conductivities. This systematic underestimation of LATs also reflects in the

ECG. The bidomain simulation with the Roberts conductivity settings yielded the smallest P wave correlation to the bidomain ECGs with the Clerc conductivity ratios and markedly shorter P wave duration. Also Sebastian et al. [43] found that the choice of conductivity ratios in the intra- and extracellular domain as well as in longitudinal and transversal fiber direction had a marked effect on CV and LATs. Intra- and extracellular conductivity values were derived by Clerc and Roberts et al. in animal experiment son specimen from excised trabe cularcardiac bundles. Measuring intra- and extracellular current flow using micro electrodes allowed for a computation of the resistance and in turn the conductivity in longitudinal and transversal fiber direction in both, the extra- and intracellular space. Considering the complex and cumbersome in and ex vivo experiments to derivetheseparameters,fixedratiosbetweenσi andσe alongand perpendicular to the myocardial fiber orientation need to be assumed when personalizing computer models.As a consequence, the high uncertainty of the ratio between σi and σe whichcannot be measured patient-specifically with reasonable efforts further justifies the application of simplified models that do not involve uncertainties in non-measurable entities and only cause minor differences in LATs, ECGs and APD90. Among all investigated simplified model solutions, the mono domain model yielded the most accurate results regarding activation times, repolarization behavior and ECGs. However, explicit conductivity tuning for the mono domain model neither had a notable effect on LATs, nor APD90, nor on the 12-lead ECG. With mean and standard deviation of the absolute LAT differences to the bidomain results quantifying to 1.37 ± 1.16 ms and 1.43 ± 1.17 ms for the RE+ and the Eikonal model, respectively ,which differed onlys lightly due to numerical jitter. The distribution of LAT discrepancies to the bidomain results mapped on the atrial geometry was similar for the Eikonal and the RE+ model. The LATs of the simplified propagation models were especially higher compared to the bidomain results in regions on the posterior left atrial wall. In these areas, different wavefronts collided causing an acceleration of the wave in the bidomain model, which is not captured in the (reaction-)Eikonal model.Source-sinkmismatch effects caused by convex wavefronts entailing conduction slowing in the bidomain model cause smaller LATs in the Eikonal simulation results. This effect is especially visible in the area where Bachmann's bundle connects to the anterior wall of the left atrium, i.e. where a small source(Bachmann'sbundle)meets a large sink (the left atrium). At the apex of the right atrial appendage,two convex wave front straver sing the tissue from the lateral and the septal right atrial wall collide and cause Eikonal LATs to be smaller than the ones resulting from the bidomain simulation. The P waves computed with the reaction-Eikonal and the Eikonal source distribution showed similar correlation coefficients of 0.921 and 0.920 to the bidomain results. However, when evaluating repolarization dynamics, the RE+ model clearly led tomorepreciseresults.Thisreflectsontheonesidein smallerAPD90 discrepancies to the bidomain simulation results. The small APD90 discrepancies between the monodomain and RE+ simulation results might have occurred due to differences in the

activation pattern or a mismatch between the diffusion term and the Ifoot current in the case of curved wavefronts or wave collisions causing different AP upstrokes and amplitudes which subsequently lead to subtle APD changes. On the other hand, the RE+ model is capable of faithfully replicating both the P wave as well as the atrial repolarization phase in the ECG, whereas with the Eikonal model, only the P wave highly resembles the bidomain results. Using precomputed AP templates to obtain the transmembrane voltage source distribution for the Eikonal LATresults, APD90 results were systematically smaller compared to the bidomain results in regular bulk tissue regions and systematically higher in fibrotic regions. The more precise representation of repolarization behavior in simulation results using the RE+ model is due to local APD balancing caused by the diffusion term. Consequently, also the repolarization signal in the ECG obtained with the source distribution derived from the Eikonal results only showed a correlation coefficient of 0.62 to the bidomain ECG.

ECGs calculated with the BEM highly resembled the ECGs obtained with the FEM. P wave correlation coefficients to the FEM approach quantified to 0.94 and 0.93 for the simulation scenario with fibrosis modeled as slow conducting and non-conductive patches, respectively. In the former scenario, transmembrane voltages can be used as a source model for the forward calculation, whereas in the latter, volumetric sources such as primary impressed currents were necessary to model the effect of passive conduction barrier not contributing to the electrical source distribution in the heart. If the surface transmembrane voltages had been used as sources for the forward calculation in this case as well, an offset in the isoelectric line in the P wave would have been induced. The infinite volume conductor method instead yielded more inaccurate ECG results. Especially in the septal and anterior leads, the ECG amplitudes were overestimated by a factor of >2 compared to the FEM results. On the one side, this observation can be traced back to the method's assumption that the atria are immersed in an infinite medium of a homogeneous conductivity, which does not allow considering a heterogeneous conductivity setup in the torso. On the other hand, the high ECG errors occurred predominantly in leads measured at electrode locations on the body surface in close proximity to the cardiac sources. Thus, neglecting the attenuating effect that the bounded torso volume conductor introduces causes a more pronounced effect on the resulting ECGs in V1-V3.

Simulations were run on a 16 core CPU machine (Intel Xeon Gold 6230, 2.1 GHz). The full bidomain and the pseudobidomain simulation for a duration of 450 ms were completed in 25and1.5hours, respectively. Computation time for the RE+ setup was 1.4 hours on a 6 core machine.The computation of the transfer matrix for the BEM approach in the case of a hetero geneous torso volume conductor with seven surfaces bounding the atria, the torso and other organs took 2 hours on a 4 core CPU machine (Intel Core i5, 2.4 GHz). The speed-up in computation times when using simplified propagation models is comparable to a ventricular setup. Computational performance improved by one order of magnitude when using the mono domain model [7] and up to three orders of magnitude when using the

Eikonal or RE+model[4],[5]comparedtobidomain.However,increasing the number of cores the simulations are ran on could change the results regarding algorithmic efficiency as different models might exhibit different scalability properties when parallelized to multiple threads or processes[44].Solverswithstrongscaling capabilities have been shown to provide the basis for fast simulation runs of the biophysically detailed mono domain model without any cutbacks on anatomical and electro physiological properties [45]. In the simulations in our study, the degrees of freedom in terms of number of nodes and elements in the mesh was the same for all propagation models. High resolutions in time and space are required for numerical convergence of the bi- and mono domain solution [46]. As described by Wood worth et al. [47], a high mesh resolution is a necessary requirement for CV convergence, especially for low conductivities (see also Fig. S3 in the supplementary material). On the other side, (reaction-)Eikonal models are capable of faithfully estimating activation time sequences on coarser meshes [5], [48]. The computational complexity of the Eikonal model depends on the method used to solve it [49], but is approximately O(nlog(n)) with n being the number of nodes in the mesh. These properties could be taken advantage of to further reduce computational cost when running simulations based on these simplified models.

Computational savings using the BEM approach are on the one hand due to the decreased problem complexity when discretizing the domain with surface instead of volume elements [37]. On the other hand, coarser resolution meshes can be applied which is the key influencing factor for an improved computational efficiency over FEM [50].

B. Related Work

In our work, we studied the differences in activation and repolarization times when using different propagation models in atrial electro physiology, which, to the best of our knowledge, has not been done before in a comprehensive way. However,comparable studies have partly already been conducted for the ventricles and four-chamber heart models. Potse et al. [8] found that activation using bidomain was 2 % faster compared to the monodomain approach for a complete cardiac cycle. Also in our study, the monodomain activation times were on average 1 mshigher than those obtained from the bidomain simulation. Pashaei et al. [51], [52] as well as Wallman et al. [4] found that the differences in activation times are small for a ventricular simulation setup when comparing biophysically detailed approaches and the Eikonal model. Neic et al. [5] compared extracellular potential fields, electro grams and ECGs calculated with the RE and the bidomain model for the ventricles and concluded that the simplified model can replicate the gold standard results with high fidelity. Gassa et al. [53] investigated the suitability of an RE model to generate re-entrant activity on a bi-atrial geometry and succeeded in replicating the wave patterns resulting from a mono domain simulation. We have also recently shown that the Eikonal-based models can produce activation times and ECGs resembling full bidomain

simulation results with high fidelity in an atrial model without cellular remodeling placed inahomogeneoustorsovolumeconductor[54].Here,we extended the setup to heterogeneous scenarios covering cellular and conductivity hetero geneity in both the torso and the atria and observed similar results. This work confirms the findings from previous studies mainly conducted for ventricular simulation setups.

Previous studies have also investigated the application of simplified forward calculation methods to computed ECGs. Schuler et al. [42] suggest the calculation of ECGs based on the BEM with coarse resolution surface meshes bounding the heart and the torso whereby parameters to blur the cardiac sources are optimized beforehand to avoid discontinuous wave propagation. In this way, they obtained body surface potentials in accurate accordance with the bidomain simulation results for a ventricular setup. However, one major drawback of the BEM approach is the impossibility of accounting for anisotropic conductivity in the myocardium [37]. However, we found that P wave correlation coefficients still quantified to >0.93 showing that the isotropic assumption yields similar ECGs compared to the bidomain results. For the infinite volume conductor method instead, not only the assumption of is otropicmyo cardial conductivities but also of a homogeneous torso volume conductor has to be made. Moreover, the simplified assumption that the atria is immersed in a medium of infinite spatial extent holds. Although the general P wave morphology was preserved, the ECG still substantially differs regarding peak-to-peak amplitudes in the precordial leads and atrial repolarization in the inferior leads as it reflects in our results and was reported in previous work [55]. For the application field of computing in tracardiac electro grams, the reader is referred to the review by SÃ¡nchez et al. [6].

C. Limitations

In this work, we investigated 4 different simulation scenarios comprising a healthy baseline case and three atrial models infiltrated with fibrosis, which was modeled either as slow conductingpatches,non-conductive conduction barriers orionic conduct anceres caling.For the spatially distributed fibrotic areas (patchy and diffuse), none of the fibrosis remodeling scenarios had a marked effect on the ECG compared to the healthy baseline case. Ionic conductance rescaling, slow conducting f ibrotic patches and percolation reflect in the ECG as a slight prolongation of the repolarization phase and an offset in the isoelectric line, a marginal prolongation of the P wave and a decrease in peak-to-peak P wave amplitudes, respectively. However,all these effects on the ECGaresmallandwouldshow up in a more pronounced way if different fibrosis remodeling approaches were combined [1]. However, we intentionally decided to investigate the effect of different propagation models and forward calculation methods in each of these simulation scenarios separately to shed light on which fibrosis remodeling aspects can be accurately captured by the simplified model solutions.

In our simulation setup, we did not consider motion and contraction of the atria for the sake of reducing model complexity and computational cost. Moss et al. showed that a fully coupled electro-mechanical model does not have any influence on simulation results regarding atrial activation and that resulting P waves exhibit negligible differences to the ones computed on a non-deforming model [56]. However, the atrial repolarization results of our study might be affected to a larger extent by the lack of a coupled model aspreviousstudiesreportedasubstantial impact of mechanical feedback on electrophysiological behavior in the ventricles [57], [58], especially during the repolarization phase [56], [59].

CVs were derived from the values reported in [22]. Based on them, conductivities were computed using tune CV [25] as described in SectionII- Ausing strand meshes.However,nobath loading effects, mesh and wavefront curvature were considered when tuning the CVs,which might lead to mis matchingCVsand conductivities assigned to different regions in the more complex atrial geometry. Adding a bath in the experiments set up for the tuning process, could lead to more similar LAT and ECG results between the bidomain results with Clerc and Roberts conductivities on the bi-atrial geometry. Moreover, performing the tuning with a bath attached to the strand geometries would lead to different monodomain conductivities for the setups without explicit conductivity tuning while the conductivity values in case of explicit conductivity tuning for the mono domain simulation would remain unchanged. Conductivities in transverse and longitudinal direction needed to be scaled by a factor of 54 and 12, respectively. The tuning procedure caused the original transversal vs. longitudinal conductivity ratios reported by Clerc and Robertsetal.to change while keeping in tra-vs.extracellular conductivity ratios constant.

The average edge length of the atrial geometry was 523 μm.To quantify the numerical error arising due to the mesh resolution, we conducted experiments on a 5 cm × 2cm× 2.8 mm block mesh with a resolution of 528 μm and a refined resolution of 265 μm by linearly subdividing the elements (see Fig. S2 in the supplementary material). Using the same numerical settings as for the experiments on the bi-atrial geometry, we ran a simulation of a planar wave passing through an isthmus and then propagating with a curved wavefront. Conductivities were adjusted using tune CV [25] as described in Section I to the CV in the regular atrial bulk tissue region. Maximum LAT differences between the experiments on the coarse and the fine mesh were 1.2 ms. Considering the total activation time in the block of 43 ms, the error introduced by the coarse mesh resolution was 2%. The root mean squared errors between two APs resulting from the simulations on the coarse and the fine mesh were 0.0186 mV and 0.0491 mV for the two nodes marked in Fig. 2 in the supplementary material. When adding a fibrotic region to the block, the maximum absolute LAT error between the experiments on the fine and the coarse mesh was 1.2 ms (~2 %) as well (see Fig. 3 in the supplementary material) for planar wave propagating along fiber direction. The latter is approximately also the case in our bi-atrial simulation setup where the depolarization wavefront traverses the elliptically shaped fibrotic patches growing predominantly in

fiber direction. However,ifanotabletransversewavepropagationhadtobe represented, our chosen mesh resolution of 523 μm would have been too coarse to capture the wave propagation at a velocity of 0.15 m/s. Thus, the mesh resolution chosen for the atrial model in this study mightintroduce anerrorof2%,whichisequivalent to an absolute LAT error of ~2 ms on the bi-atrial mesh. Due to the small root mean squared error between the APs of the coarse and the fine mesh, no additional discretization error affecting APD90 is expected.

V. CONCLUSION

The results presented here show that the Eikonal model is capable of faithfully producing LATs and P waves compared to full bidomain simulations with a reduction of computation times by a factor of up to three orders of magnitude. However, propagation models neglecting diffusion terms lack the fidelity in terms of repolarization as shown by APD90 deviations. Thus, RE models are needed e.g. in cases where repolarization dynamics are of significant importance such as e.g. for re-entry mechanism studies. ECGs calculated with the BEM accurately resemble the FEM results for both P waves and the ECG in the repolarization phase. When computing ECGs with the infinite volume conductor method, the systematic overestimation of peak-to-peak P wave amplitudes especially in the precordial leads should be taken into account when evaluating P wave features.

REFERENCES

[1] C. Nagel et al., "Non-invasive and quantitative estimation of left atrial fibrosis based on P waves of the 12-lead ECG-a large-scale computational study covering anatomical variability," J. Clin. Med., vol. 10, 2021, Art. no. 1797.

[2] G. Luongo et al., "Hybrid machine learning to localize atrial flutter substrates using the surface 12-lead electrocardiogram," EP Europace, vol. 24, no. 7, pp. 1186–1194, 2022.

[3] L. Azzolin et al., "A reproducible protocol to assess arrhythmia vulnera bility: Pacing at the end of the effective refractory period," Front. Physiol., vol. 12, 2021, Art. no. 656411.

[4] M. Wallman, N. P. Smith, and B. Rodriguez, "A comparative study of graph-based, eikonal, and monodomain simulations for the estimation of cardiac activation times," IEEE Trans. Biomed. Eng., vol. 59, no. 6, pp. 1739–1748, Jun. 2012.

[5] A.Neicetal., "Efficient computation of electrograms and ECGs in human whole hearts imulations using a reaction-eikonalmodel,"J.Comput.Phys., vol. 346, pp. 191–211, 2017.

[6] J. Sánchez and A. Loewe, "A review of healthy and fibrotic myocardium microstructure modeling and corresponding intracardiac electrograms," Front. Physiol., vol. 13, 2022, Art. no. 908069.

[7] M. J. Bishop and G. Plank, "Bidomain ECG simulations using an aug mented mono domain model

fort he cardiac source,"IEEETrans.Bio-Med. Eng., vol. 58, no. 8, pp. 2297–2307, Aug. 2011.

[8] M.Potseetal., "A comparison of mono domain and bidomain propagation models for the human heart," in Proc. IEEE Annu. Int. Conf. Eng. Med. Biol. Soc., 2006, pp. 3895–3898.

[9] E. Vigmond et al., "Percolation as a mechanism to explain atrial fraction ated electrograms and reentry in a fibrosis model based on imaging data," Heart Rhythm, vol. 13, pp. 1536–1543, 2016.

[10] L. Azzolin et al., "Automated framework for the augmentation of missing anatomical structures and generation of personalized atrial models from clinical data," in Proc. Comput. Cardiol. Conf., 2021, pp. 1–4.

[11] C. H. Roney et al., "Modelling methodology of atrial fibrosis affects rotor dynamics and electrograms," EPEuropace,vol.18,pp.iv146–iv155, 2016.

[12] M.W.Kruegeret al., "Personalization of atrial anatomy and electrophysiology as a basis for clinical modeling of radio-frequency ablation of atrial f ibrillation," IEEE Trans. Med. Imag., vol. 32, no. 1, pp. 73–84, Jan. 2013.

[13] W.Jakobetal.,"Instantfield-alignedmeshes,"ACMTrans.Graph.,vol.34,pp. 1–15, 2015.

[14] L. Azzolin et al., "AugmentA: Patient-specific augmented atrial model generation tool," medRxiv, 2022, doi: 10.1101/2022.02.13.22270835.

[15] T. Zheng et al., "An automate pipeline for generating fiber orientation and region annotation in patient specific atrial models," Curr. Directions Biomed. Eng., vol. 7, pp. 136–139, 2021.

[16] R.Piersantietal., "Modeling cardiacmuscle fibers inventri cularan datrial electrophysiology simulations," Comput. Methods Appl. Mechanics Eng., vol. 373, 2021, Art. no. 113468.

[17] P. C. Africa et al., "lifex- heart module: A high-performance simulator for the cardiac function. package 1: Fiber generation," 2022, arXiv:2201. 03303.

[18] A. Neic et al., "Automating image-based mesh generation and manipulation tasks in cardiac modeling workflows using meshtool," SoftwareX, vol. 11, 2020, Art. no. 100454.

[19] K. Gillette et al., "A framework for the generation of digital twins of cardiac electrophysiology from clinical 12-leads ECGs," Med. Image Anal., vol. 71, 2021, Art. no. 102080.

[20] A. Reinke et al., "Geometrical model and corresponding conductivities for solving the inverse problem of ECG," in Biomedizinische Technik / Biomed. Eng., vol. 59, pp. 937–940, 2014.

[21] D. Keller et al., "Ranking the influence of tissue conductivities on forward-calculated ECGs," IEEE Trans. Biomed. Eng., vol. 57, no. 7, pp. 1568–1576, Jul. 2010.

[22] A.Loeweetal.,"Leftandrightatrialcontribution to the p-waveinrealistic computational models," in Proc. Int. Conf. Funct. Imag. Model. Heart, pp. 439–447, 2015.

[23] M. W. Krüger, "Personalized multi-scale modeling of the atria : Hetero geneities, fiber architecture, hemodialysis and ablation therapy," Ph.D. dissertation, KIT Scientific Publishing, Karlsruhe, Germany, 2013.

[24] G. Plank et al., "The openCARP simulation environment for cardiac electrophysiology," Comput. Methods Programs Biomed., vol. 208, 2021, Art. no. 106223.

[25] C. Costa et al., "Automatic parameterization strategy for cardiac electro physiology simulations," in Proc. Conf. Comput. Cardiol., 2013, pp. 373376.

[26] L. Clerc, "Directional differences of impulse spread in trabecular muscle from mammalian heart," J. Physiol., vol. 255, pp. 335–346, 1976.

[27] D.E.RobertsandA.M.Scher,"Effect of tissue aniso tropy on extra cellular potential fields in canine myocardium in situ," Circulation Res., vol. 50, pp. 342–351, 1982.

[28] M. Courtemanche, R. J. Ramirez, and S. Nattel, "Ionic mechanisms underlying human atrial action potential properties: Insights from a mathematical model," Amer. J. Physiol.-Heart Circulatory Physiol., vol. 275, no. 1, pp. H301–H321, 1998.

[29] M.W.Kruegeretal.,"In-silico modeling of atrial repolarization in normal and atrial fibrillation remodeled state," Med. Biol. Eng. Comput., vol. 51, pp. 1105–1119, 2013.

[30] L. Tung, A Bi-domain Model for Describing Ischemic Myocardial DC Potentials. Ph.D. Dissertation, Massachusetts Inst. Technol., Cambridge, MA, USA, 1978.

[31] P. C. Franzone, L. F. Pavarino, and S. Scacchi, Mathematical Cardiac Electrophysiology, vol. 13, Berlin, Germany: Springer, 2014.

[32] J. Keener and J. Sneyd, Mathematical Physiology 1: Cellular Physiology. Berlin, Germany: Springer, 2009.

[33] E. Vigmond et al., "Solvers for the cardiac bidomain equations," Prog. Biophys. Mol. Biol., vol. 96, no. 1–3, pp. 3–18, 2008.

[34] S. A. Niederer et al., "Verification of cardiac tissue electrophysiol ogy simulators using an n-version benchmark," Philos. Trans. Roy. Soc. A Math. Phys. Eng. Sci., vol. 369, no. 1954, pp. 4331–4351, 2011.

[35] E.Pernodetal.,"Amulti-front eikonal model of cardiac electro physiology for interactive simulation of radio-frequency ablation," Comput. Graph., vol. 35, no. 2, pp. 431–440, 2011.

[36] A. J. Pullan, K. A. Tomlinson, and P. J. Hunter, "A finite element method for an eikonal equation model of myocardial excitation wavefront propagation," SIAM J. Appl. Math., vol. 63, no. 1, pp. 324–350, 2002.

[37] M.Potse,B.Dube,andA.Vinet,"Cardiacanisotropyinboundary-element models for the electrocardiogram," Med. Biol. Eng. Comput., vol. 47, pp. 719–729, 2009.

[38] D. B. Geselowitz and T. W. Miller, "A bidomain model for anisotropic cardiac muscle," Ann. Biomed. Eng., vol. 11, pp. 191–206, 1983.

[39] M.Stenroos, V. Mäntynen, and J. Nenonen, "A Matlab library for solving quasi-static volume conduction problems using the boundary element method," Comput. Methods Programs Biomed., vol.

88, pp. 256–263, 2007.

[40] K.Higuchietal.,"The spatial distribution of late gadolinium enhancement of leftatrialmagneticresonanceimaginginpatientswithatrialfibrillation," JACC: Clin. Electrophysiol., vol. 4, pp. 49–58, 2018.

[41] E. J. Vigmond et al., "Computational tools for modeling electrical activity in cardiac tissue," J. Electrocardiol., vol. 36, pp. 69–74, 2003.

[42] S. Schuler et al., "Spatial downsampling of surface sources in the forward problem of electrocardiography," in Funct. Imaging and Modeling of the Heart, Y. Coudière et al., Eds., vol. 11504, Berlin, Germany: Springer, 2019, pp. 29–36.

[43] R.Sebastianetal.,"Assessing influence of conductivity in heart modelling with the aim of studying cardiovascular diseases," Med. Imag., vol. 6916, 2008, Art. no. 691627.

[44] T. Cojean, F. Goebel, and M. Houillon, "Porting the OpenCARP cardiac electrophysiology simulation framework to GPU architectures," in Proc. 5th ISC Workshop HPC Appl. Precis. Med., 2022, Art. no. 956.

[45] C. M. Augustin et al., "Anatomically accurate high resolution modeling of human whole heart electromechanics: A strongly scalable algebraic multigrid solver method for nonlinear deformation," J. Comput. Phys., vol. 305, pp. 622–646, 2016.

[46] P. Pathmanathan et al., "A numerical guide to the solution of the bidomain equations of cardiac electrophysiology," Prog. Biophys. Mol. Biol., vol. 102, pp. 136–155, 2010.

[47] L. A. Woodworth, B. Cansız, and M. Kaliske, "A numerical study on the effects of spatial and temporal discretization in cardiac electro physiology," Int. J. Numer. Method Biomed. Eng., vol. 37, 2021, Art. no. e3443.

[48] Z.Fu,R.M.Kirby,andR.T.Whitaker,"A fast iterative method for solving the eikonal equation on tetrahedral domains," SIAMJ. Sci. Comput., vol. 35, pp. c473–c494, 2013.

[49] A. Capozzoli et al., "A comparison of fast marching, fast sweeping and fast iterative methods for the solution of the Eikonal equation," in Proc. 21st Telecommun. Forum Telfor, 2013, pp. 685–688.

[50] S. Mukherjee and M. Morjaria, "On the efficiency and accuracy of the boundary element method and the finite element method," Int. J. Numer. Methods Eng., vol. 20, pp. 515–522, 1984.

[51] A. Pashaei et al., "Comparison of phenomenological and biophysi cal cardiac models coupled with heterogenous structures for prediction of electrical activation sequence," in Proc. Comput. Cardiol., 2010, pp. 871–874.

[52] A. Pashaei et al., "Fast multiscale modeling of cardiac electrophysiology including purkinje system," IEEE Trans. Biomed. Eng., vol. 58, no. 10, pp. 2956–2960, Oct. 2011.

[53] N.Gassaetal., "Spiral waves generation using an eikonal-reaction cardiac electrophysiology model," in Proc. Int. Conf. Functional Imag. Model. Heart, 2021, pp. 523–530.

[54] C. Nagel et al., "Comparison of source models and forward calculation methods for atrial electrophysiology regarding activation times and electrocardiograms," in Proc. iHEART Congr. Modelling Cardiac Function, 2021, p. 48.

[55] L. R. Bear et al., "Forward problem of electrocardiography: Is it solved ?," Circulation Arrhythmia Electrophysiol., vol. 8, pp. 677–684, 2015.

[56] R. Moss et al., "A fully-coupled electro-mechanical whole-heart com putational model: Influence of cardiac contraction on the ECG," Front. Physiol., vol. 12, 2021, Art. no. 778872.

[57] M.Salvadoretal., "Electromechanical modeling of humanventricles with ischemic cardiomyopathy: Numerical simulations in sinus rhythm and under arrhythmia," Comput. Biol. Med., vol. 6, 2021, Art. no. 104674.

[58] M. Salvador et al., "The role of mechano-electric feedbacks and hemo dynamic coupling in scar-related ventricular tachycardia," Comput. Biol. Med., vol. 142, 2021, Art. no. 105203.

[59] T. Gerach et al., "Electro-mechanical whole-heart digital twins: A fully coupledmulti-physicsapproach,"Mathematics,vol.9,2021,Art.no.1247

ISSN : 2582-7405

Global ECG Classification by Self-Operational Neural Networks With Feature Injection

Muhammad Uzair Zahid,Serkan Kiranyaz and Moncef Gabbouj

ABSTRACT

Objective: Global (inter-patient) ECG classif ication for arrhythmia detection over Electrocardiogram (ECG) signal is a challenging task for both humans and machines. Automating this process with utmost accuracy is, therefore, highly desirable due to the advent of wearable ECG sensors. However, even with numerous deep learning approaches proposed recently, there is still a notable gap in the performance of global and patient-specific ECG classification performance. Methods: In this study, we propose a novel approach for inter-patient ECG classification using a compact 1D Self-ONN by exploiting morphological and timing information in heart cycles. We used 1D ONNlayers to automatically learn morphological representations from ECG data, enabling us to capture the shape of the ECG waveform around the R peaks. We further inject temporal features based on RR interval for timing characterization. The classification layers can thus benefit from both temporal and learned features for the final arrhythmia classification. Results: Using the MIT-BIH arrhythmia benchmark database, the proposed method achieves the highest classification performance ever achieved, i.e., 99.21% precision, 99.10% recall, and 99.15% F1-score for normal (N) segments; 82.19% precision, 82.50% recall, and 82.34% F1-score for the supra-ventricular ectopic beat (SVEBs); and finally, 94.41% precision, 96.10% recall, and 95.2% F1-score for the ventricular-ectopic beats (VEBs). Significance: As a pioneer application, the results show that compact and shallow 1D Self-ONNs with the feature injection can surpass all state-of-the-art deep models with a significant margin and with minimal computational complexity. Conclusion: This study has demonstrated that using a compact and superior network model, a global ECG classification can still be achieved with an elegant performance level even when no patient-specific information is used.

Index Terms—Inter-patient ECG classification, operational neural networks, real-time heart monitoring, generative neurons.

I. INTRODUCTION

CARDIOVASCULAR diseases (CVDs) are responsible for 31% of deaths globally, according to the World Health Organization (WHO) [1]. It is crucial to detect CVDs as early as possible to begin effective treatment and medication.Forcardiac arrhythmia detection, a variety of methods such as

blood tests, stress tests, echocardiograms, and chest X-rays have been used. Still, ECGs are perhaps the most popular among clinicians. ECGs record the heart's electrical activity over time and can help diagnose many conditions, including premature ventricular contractions (PVCs or V rhythms) and supraventricular premature beats (SPBs or S rhythms). An experienced cardiologist can determine the presence of an arrhythmia, as an abnormality of heart rate or rhythm or a change in morphological pattern, by analyzing a recorded ECG signal. However, identifying and classifying arrhythmias can be an erroneous ,labor-intensive ,and subjective task even for cardiologists since it often requires considering each heartbeat of an ECGsignalaccumulatedoverhours or days. With the recent advances in various low-cost portable ECG devices [2], [3] such as chest straps and wristbands, the opportunities for self-monitoring and auto-diagnosis have increased. Therefore, it is highly desirable to have global (patient independent or inter-patient) and reliable ECG classification methods. However, robust and accurate classification of ECG signals still poses a challenge because among different patients or even for the same patient but under different temporal, psychological, and physical conditions, significant variations may occur in ECG signals' morphological and temporal/structural characteristics.

ECG-based arrhythmia classification is typically initiated with a peak detection/segmentation. This study does not discuss R-peak detection since highly accurate algorithms have already been proposedin the literature [4], [5]. The analysis and classification of ECGsignals have been extensively studied throughout the last decades [6]–[9]. Generally, these works can be classified as intra-patient, inter-patient (global), and patient-specific [10]. In the intra-patient paradigm, datasets are divided into and test subsets according to heartbeat labels. Therefore, beats from the same individual may appear both in training and evaluation subsets, making the evaluation process biased [11]. The classifiers usually produce over-optimistic results (in close vicinity of 100%) because the model learns the information specific to the patient during the training phase [11]–[13]. The classification performance declines due to inter-individual variability. Hence, morphological variations in ECG from different patients should be considered when building the model. Even for a healthy subject's (normal) ECG waveform, the shape of the QRS complex, P waves, and R–R intervals may differ from one beat to the next under various circumstances [14]. Chazal et al. [15] presented the inter-patient paradigm where training and testing heartbeats are collected from different patients' ECG recordings to adopt real-world scenarios. Some patients are reserved for the evaluation phase and beats from other patients are used to train the classifier so that classifier would exhibit a better generalization capability for new unseen patients. Most researchers have chosen to use another approach called the "patient-specific" paradigm, i.e., [9], [16]–[18] in which other patients and patient-specific beats of a new patient are jointly used to train the network. Although the patient-specificparadigm is superior to inter-patient paradigms in terms of performance, it requires cardiologists' labeling in advance for each (new) patient, which is cumbersome, subjective, and labor-intensive. Furthermore, a new network should always be trained

from scratch or fine-tuned carefully to achieve the required generalization. Only then one can evaluate and test its reliability, all of which limit its clinical application. Especially, the training of these personalized models requires the collection of patientspecific arrhythmic data, which requires long-term monitoring or even may not exist. As the data volume increases, it becomes difficult or even impossible to manually label small chunks of data from all stored records. In a recent work [19], an adaptive patient-specificheartbeatclassificationmodelisproposedfordiagnosing heart arrhythmias. A general classifier was first trained on the general population. Then, the weights in the lower part of the general classifier were retained using i-vectors and the weights in the upper part were randomized.

For several decades ,feature engineering-based methods dominated ECG signal recognition. Studies [20]–[23] based on traditional signal processing and machine learning methodologies have not been successful inclinical settings.This is because there can be significant variations in the morphological characteristics and temporal/structural dynamics of ECG signals for different patients or even the same patient under varying physical, psychological, and temporal conditions. Such hand-crafted feature extraction may not capture the actual characteristics of each ECG beat variation for accurate classification. Therefore, their performance level varies significantly in large ECG datasets [24]. Moreover, extreme performance variations may occur due to increased noise levels, different ECG sensor types, inter-patient variations in ECG signals, and different arrhythmia prevalence between databases.

Mariano et al. [25] extracted features using both leads of ECG, wavelet transform, and RR intervals. The floating feature selection model was used to reduce the feature set, and finally, eight features were fedin to the classifier. Canetal. [26] extracted morphological features using wavelet transform and dynamic features using RR intervals. A combination of these features is then fed into the SVM classifier. The authors reported an overall accuracy of 86.4% in the patient-specific evaluation. In another study [27], a weighted variant of the conditional random fields classifier(CRF)wasusedwithL1regularizationandachievedan accuracy of 85%. Khorrmi et al. conducted a comparative study of feature extraction and classification methods. The Discrete Wavelet Transform (DWT), Continuous Wavelet Transform CWT), and Discrete Cosine Transform (DCT) were compared to extract features. Similarly, a comparison between a multilayer perceptron (MLP) and a support vector machine (SVM) was presented as a classifier [28]. Karpagachelvi et al. combined discrete wavelet transform with high-order statistics and AR modeling to extract features, while extreme learning machines (ELMs) were used for classification [29]. For feature extraction, the authors used a vector cardiogram-based ECG representation. Features were selected using the particle swarm optimization algorithm to feed into the SVM classifier [30].

The development of deep learning models has led to the widespread use of neural networks in many applications, including face detection, image denoising, image classification, and numerous one-

dimensional signal processing. Recently, one-dimensionalconvolutionalneuralnetworks(1D-CNN)have also been extensively studied because of their speed and efficiency when managing complex tasks, as demonstrated by various applications involving signal processing [31], [32], motor fault detection [33], and advance warning system for cardiac arrhythmias [34]. In a study by Kiranyaz et al. [35], only three layers of acompact1DCNNwereusedforpatient-specificECG classification. To train each personalized classifier, the authors used only the first 5-min section of the record and 245 common beats randomly selected from the train partition of the MIT-BIH dataset, following the AAMI recommendations [36].

Several global ECG classification methods [29], [37]–[41] based on deep CNN models have recently been proposed. They naturally have high complexity and require large volumes of labeled ECG data for training. In addition, because they require parallelized hardware to function, they cannot be directly implemented on low-power or mobile devices. Finally, most methods tested on unseen patients do not perform well in the inter-patient paradigm. As opposed to beat-wise classification, alternative deep learning approaches used ECG segments instead. In their study, Acharya et al. used two and five seconds of ECG data with a 10-layer CNN model [42]. The deep network architecture proposed by Li et al. consists of densely connected CNNs (DenseNet) further connected to gated recurrent units (GRU). 10-second ECG segments were analyzed, and the F1 score was only 61.25% for SVEB detection and 89.75% for VEB detection [43]. The results have shown that even with deep network models, especially the SVEB detection performance is relatively poor in general, which hinders their clinical usage.

Recent studies [44]–[49] have pointed out that CNNs are homo geneous networks with an ancient linear neuron model that originated in the 1950s (McCulloch-Pitts). The linear neuron model is a crude representation of biological neurons with specialized electrophysiological and biochemical properties in highly heterogeneous biological networks [29]. Following this, Operational Neural Networks (ONNs) [44], [50] have been proposed to address such drawbacks. ONNs derived from Generalized Operational Perceptrons (GOPs) [44]–[49] are heterogeneous networks with a nonlinear neuron model, which permits them to learn highly complex and multimodal functions or spaces with minimal network complexity and training data. Studies [51]–[53] have proposed the latest ONN variant, SelfOrganized ONNs (Self-ONNs), for various image processing and regression tasks.

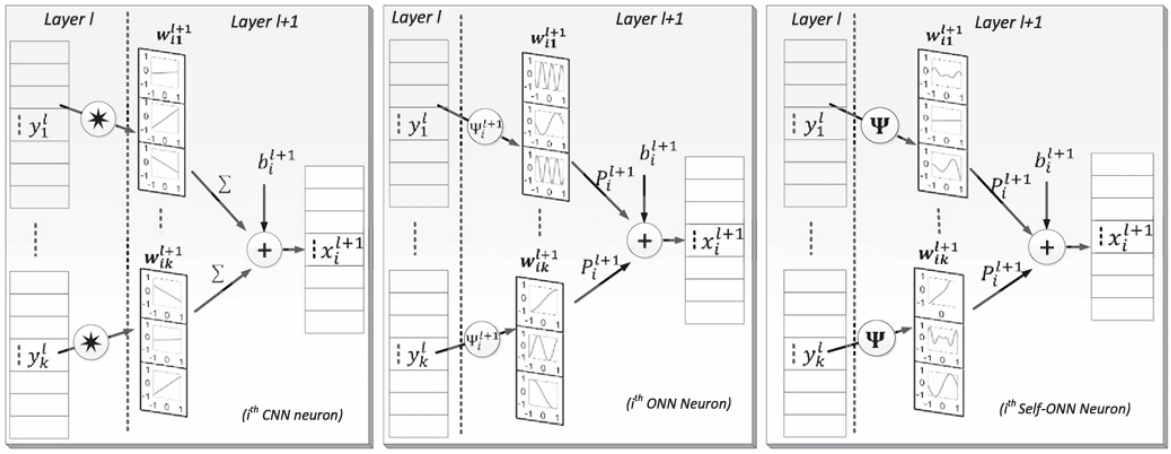

Fig. 1. An illustration of the 1D nodal operations with the 1D kernels of the k^{th} CNN (left), ONN (middle), and Self ONN (right) neurons at layer l [54].

In this study, we propose a novel inter-patient ECG classification approach to address the aforementioned issues. The proposed method is based on compact 1D Self-ONNs, with feature injection/fusion ability. In our method, normalized ECG signals are divided into 230 samples (639 ms) of fixed-duration frames using the R peak as a reference point. To accomplish a multi-scale representation, each frame is decomposed into the time-frequency domain using Discrete Wavelet Transform (DWT) at nine different scales to achieve the scale invariance. As arrhythmia affects not only the morphology of the heart cycle but also varies the timing of beat, four R-R intervalbased features are extracted and injected into the Self-ONN model to enrich the learned features. We evaluate the proposed approach on the MIT-BIH database. Overall, the novel and significant contributions of this study can be enlisted as follows:

1. Wedeveloped a compact architecture with 1D Self-ONN layers for global ECG classification that significantly outperforms all state-of-the-art methods.

2. This is the first study that proposes Self-ONNs with feature injection to perform a joint classification in the same network.

3. A multi-scale approach using DWT is proposed to transform the raw ECGsignal before feeding it to the network and thus achieve the scale invariance.

4. Finally, over the MIT-BIH benchmark dataset, we show that without changing or fine-tuning the model,the performance of our model remains the same for unseen patients despite the morphological variations.

The rest of the paper is organized as follows: Section II outlines the ECG datasets used in this study. The proposed approach is presented in Section III. In Section IV, the performance of the proposed system is evaluated over the MIT-BIH database using the standard performance metrics, and theresults are compared with the recent state-of-the-art works. Finally, Section V concludes the paper and suggests topics for future research.

II. 1D SELF-ORGANIZED OPERATIONAL NEURAL NETWORKS

Fig. 1 shows 1D nodal operations of a CNN, ONN with fixed (static) nodal operators, and Self-ONN with generative neuron which can approximate any arbitrary nodal function, ψ, (including the conventional types such as linear, exponential, Gaussian, or harmonic functions) fore achkern elelemen to feach connection. With such generation ability, obviously, Self-ONNs have the potential to achieve greater operational diversity and flexibility, allowing the optimal nodal operator function to be formed for each kernel element to maximize the learning performance. Another crucial advantage over conventional ONNs is that Self-ONNs do not use an operator set library or a search process to select the best nodal operator. The Qth order truncated approximation, formally known as the Mac Laurin polynomial ,takes the form of the following finite summation:

$$\psi\left(x\right)^{(Q)} = \sum_{n=0}^{Q} \frac{\psi^{(n)}\left(0\right)}{n!} x^{n} \qquad (1)$$

The above formulation can approximate any function ψ(x) sufficiently well near 0. When the activation function bounds the neuron's input feature maps in the vicinity of 0 (e.g., tanh) the formulation of (1) can be exploited to form a composite nodal operator where the power coefficients, $\frac{\psi^{(n)}(0)}{n!}$ learned parameters of the network during training.

It was shown in [52] that the nodal operator of the kth generative neuron in the lth layer can take the following general form:

$$\widetilde{\psi}_k^l\left(\boldsymbol{w}_{ik}^{l(Q)}\left(\boldsymbol{r}\right), y_i^{l-1}\left(m+r\right)\right) = \sum_{q=1}^{Q} w_{ik}^{l(Q)}\left(r,q\right)\left(y_i^{l-1}\left(m+r\right)\right)^q \qquad (2)$$

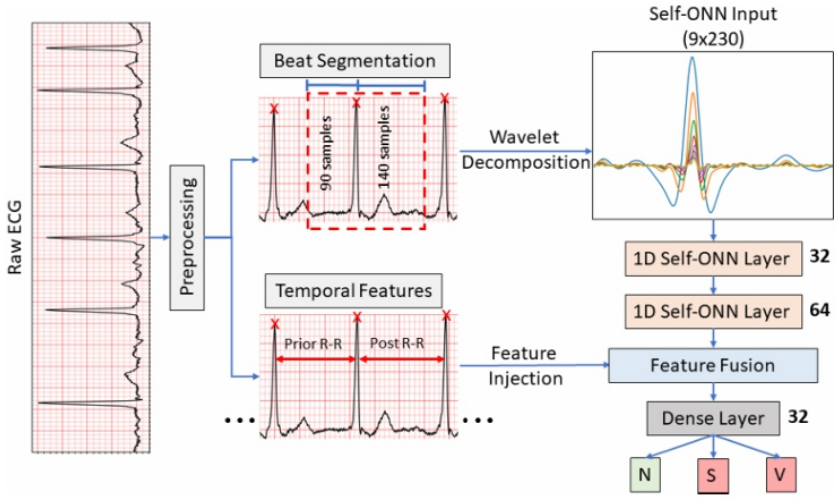

Fig. 2. Block diagram of the proposed approach and model architecture for classification of ECG signals.

$$\widetilde{x_{ik}^{l}}(m) = \sum_{r=0}^{K-1} \sum_{q=1}^{Q} w_{ik}^{l(Q)}(r,q) \left(y_i^{l-1}(m+r)\right)^q \qquad (3)$$

where K is the size of the 1D kernel of the ith neuron at layer l. One can simplify (3) as follows:

$$\widetilde{x_{ik}^{l}} = \sum_{q=1}^{Q} Conv1D\left(w_{ik}^{l(Q)}, \left(y_i^{l-1}\right)^q\right) \qquad (4)$$

Hence,the formulation can be accomplished by summation of Q1Dconvolution operations. Finally, the output of this neuron can be formulated as follows:

$$x_k^l = b_k^l + \sum_{i=0}^{N_{l-1}} \widetilde{x_{ik}^{l}} \qquad (5)$$

where bl k is the bias associated with this neuron. The 0th order term, q = 0, the DC bias, is omitted as its additive effect can be compensated by the learnable bias parameter of the neuron. With the Q = 1 setting, a generative neuron reduces back to a convolutional neuron.

The raw-vectorized formulations of the forward propagation, and detailed formulations of the Back-Propagation (BP) training in raw-vectorized form can be found in [52] and [53].

III. METHODOLOGY

The proposed global ECG classification approach is illustrated in Fig. 2. The single-channel raw ECG signal is the first unit normalized and partitioned into the segment of 230 samples. Then continuous wavelet transform is employed to convert the 1-D ECG beat into a nine-channel time-frequency beat representation (9x230) which is fed into the proposed 1D Self-ONN model. The temporal features are then injected into the Self-ONN classifier to accomplish the final classification of the ECG beat.

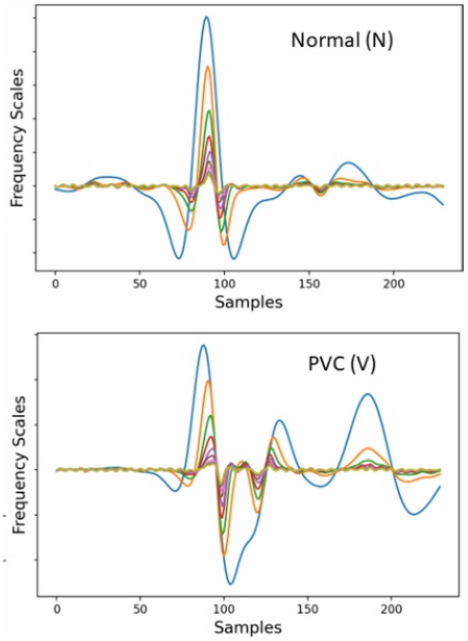

Fig. 3. Transformation patterns of a normal heartbeat (top) and an abnormal heartbeat due to premature ventricular contractions (bottom).

A. Problem Formulation

In general, abnormalities in the ECG signals can be linked to two main aspects: ECG beat morphology (morphological variations) and the time interval between ECG beats (temporal

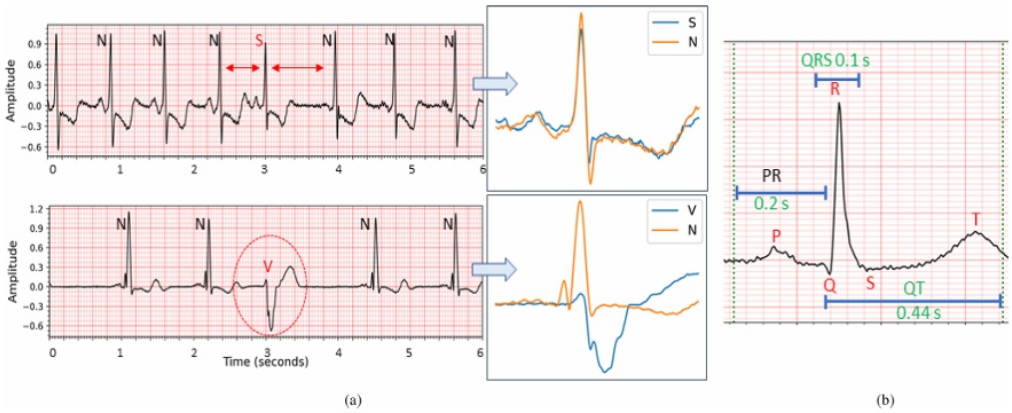

Fig. 4. (a) On top, the S beat exhibits temporal variation. In contrast, the beat morphology of successive S and N beats is almost identical. We can observe variation in the subsequent N and V beat morphology in the bottom plot. (b) ECG cardiac cycle and intervals between different waves.

variations). As illustrated in Fig. 4, the top figure shows a premature beat (temporal variance between R peaks), and the bottom figure shows ill-shaped QRS complexes (morphological variance). The morphology of each heartbeat plays a vital role in classifying arrhythmia. Moreover, the timing or location of the heartbeat is also a crucial feature. Segment-based classification can detect abnormalities without looking at timing data explicitly since the input is based on multiple beats or cardiac cycles. On the other hand, when a continuous ECG signal is divided into frames, each with a single beat, this will cause the loss of temporal information. It is relatively difficult to distinguish a beat from another by just examining its morphology. As can be seen in the figure, a regular N-beat and S-beat look similar. However, exploiting the beat location makes it easy to distinguish between them. This is the main reason for injecting the R-R-based features into the feature representation learned from Self-ONN layers to make the final classification.

B. Data Processing

Beat Segmentation: Each heart beat'smorphology is crucial to classifying arrhythmias. In some studies, the R peak is used as a center to segment the ECG signals. However, this is not a good approach in practice as the QT interval is approximately double the PR interval in duration. We do not need the morphological information before the P wave as it falls within the previous heart cycle boundary. PR intervals are generally between 0.12 and 0.20 seconds in duration and extend from the onset of the P wave to the beginning of the QRS complex. The QRS complex usually lasts between 0.06 and 0.10 seconds. The QT interval can range from 0.20 to 0.44 seconds depending upon heart rate. To avoid any information loss, the upper bound of each duration is considered. A detailed description of one ECG

cycle and its waves are presented in Fig. 4. By keeping the upper bound of these intervals and sampling frequency of 360Hz into consideration, the ECG signal from a single channel was segmented into heartbeats using the R peak as a reference point, taking 250msec before and 390msec after the peak

Temporal Features: In order to derive information about the timing of the ECG beat or, more precisely, about the temporal variation, we extracted four widely used R-R-based features, i.e., prior R-R interval, post R-R interval, a ratio of prior to post R-R interval and average R-R interval over ±10 seconds from the current beat.

Multi-scale ECG representation: Multi-scale ECG representation plays an important role in the classification of ECG signals . Any feature that can be used to discriminate abnormal beats from normal ones can be revealed in different frequency scales. Such features can represent the time-frequencycharacteristicsof the raw ECG signal. Some prior studies have investigated several methods for transforming ECG signals into different scales before feeding them to the classifier network. Among them, the DWT is considered to be the most efficient for processing ECG signals. When using DWT, ECG information can be retrieved both in the frequency and time domains, which is far superior to the DFT, which can only analyze ECG information in the frequency domain. This study applies DWT based on the Ricker (Mexican-hat) wavelet to transform ECG beats at nine different scales to generate one-dimensional DWT patterns in each scale. The overall multi-scale representation can be viewed as a 9channelrepresentationoftheoriginalsignalindifferentsubband frequencies. Fig. 3 shows examples of DWT transformation patterns from normal and arrhythmic ECG signals .Over an ECG segment x(t), its DWT with respect to a given mother wavelet ψ is defined as follows:

$$W_x\ (a,b) = \frac{1}{\sqrt{a}} \int_{-\infty}^{\infty} x\,(t)\,\psi\left(\frac{t-b}{a}\right) dt \qquad (6)$$

where a is a scale parameter and b is a translation parameter. The scale can be converted to frequency by

$$F = \frac{F_c\ .a}{f_s} \qquad (7)$$

where Fc is the center frequency of the wavelet basis, fs is the sampling frequency of the signal.In this study,we used a specific set of 9scales. The corresponding band frequencies of the scales range from 10 Hz to 90 Hz with a gap of 10 Hz.

Finally, we used the Ricker wavelet basis defined as

$$\psi\ (t) = \frac{2}{\sqrt{3}.\sqrt[4]{\pi}} e^{\frac{-t}{2}}\ \left(1-t^2\right) \qquad (8)$$

C. Data Augmentation

To achieve a more balanced distribution of classes so that under represented arrhythmias would become more prominent, we augmented the arrhythmia beats instead of excluding the majority class samples during the training of the classification model. Data augmentation is crucial to achieving the network's robustness and invariance with limited or imbalanced training samples across different

classes. We found that arrhythmia beats (S and Vbeats) are far less frequent than the normal beats in the MIT-BIH dataset. As described in [5], we generated augmented arrhythmic rhythms fromthe20-second ECG segments containing one or more arrhythmia beats by adding baseline wanderand motion artifacts from the Noise Stress Test Database [55].

D. Network Architecture

We have implemented the 1D Self-ONN model as illustrated in Fig. 2. This model, in brief, consists of two operational layers to extract learned features, fused with the injected temporal features, and two dense layers to analyze the combined features for classification. The first operational layer has 32 neurons with a filter size of 1x3, followed by a max-pooling layer of size 1x7. The second operational layer has 64 neurons with a filter size of 1x3, followed by an adaptive max-pooling of size 1x1, which applies the 1D adaptive max pooling over an input signal composed of several input planes. Both Self-ONN layers are followed by batch normalization and a hyperbolic tangent activation function (tanh). The output feature maps of operational layers are concatenated with the injected temporal features and fed into the dense layer where there are 32 neurons followed by rectified linear activation function (ReLu). The network's output layer size is 3, which computes the class score corresponding to each ECG class.

IV. EXPERIMENTAL RESULTS

In this section, we first present the benchmark dataset, MIT BIH, used for training and evaluation of the proposed approach. Then the metrics used for evaluating the proposed approach will be presented. Next, we will present a comprehensive set of experiments and comparative evaluations against the current state-of-the-art methods from the literature over the MIT-BIH dataset.

A. Dataset

As the gold-standard benchmark dataset, the MIT-BIH arrhythmia dataset [56] was used for performance evaluation in this study. Each recording on the MIT/BIH dataset is about a 30-minutedurationandincludestwo-channelECGsignals.Each record is taken from the 24-hour ECG signals of 47 subjects. Every ECG record is preprocessed using band-pass filtering at

TABLE I
MAPPING THE MIT-BIH ARRHYTHMIA DATABASE HEARTBEAT TYPES TO THE AAMI HEARTBEAT CLASSES [23]

AAMI Beat Class	MIT-BIH Normal/Arrhythmia types
Non-ectopic beats (N)	Normal (N)
	Right bundle branch block beats (RBBB)
	Atrial escape beats (e)
	Left bundle branch block (LBBB)
	Nodal (junctional) escape beats (j)
Supraventricular ectopic beats (S)	Aberrated atrial premature beats (a)
	Atrial premature contraction (A)
	Supraventricular premature beats (S)
	Nodal (junctional) premature beats (J)
Ventricular ectopic beats (V)	Premature ventricular contraction (PVC)
	Ventricular escape beats (E)
	Ventricular
	flutter wave (!)
Fusion beats (F)	Fusion of ventricular and normal beat (F)
Unknown beats (Q)	Paced beats (/)
	Fusion of paced and normal beats (f)
	Unclassifiable beats (Q)

0.1–100 Hz and then sampled at 360 Hz. Independent experts have annotated both timing and beat class information in the database. Advancement of Medical Instrumentation (AAMI) classifies heartbeats in this database into 15 classes. Further, it divides them into five categories, which are normal (N), supraventricular ectopic beats (SVEB), ventricular ectopic beats (VEB), fusion beats (F) and unknown beats (Q), as shown in Table I. While the MIT-BIH arrhythmia dataset is frequently used, few studies follow the AAMI class division scheme and a more realistic evaluation protocol (inter-patient paradigm).

A widely used data division method proposed by de Chazal et al. [11] is utilized to split the database in order to make a fair comparison with existing works. ECG recordings from 44 patients were divided into two datasets: DS1 and Ds2, each containing ECG data from 22 recordings of approximately equal

proportions of beat types. There are approximately 50000 heartbeats in both partitions, including routine and complex arrhythmia recordings. The first dataset (DS1) was used to train andvalidate the classifier, while the second dataset (DS2)served as the basis for the final performance evaluation.

In Table II, ECG record partitions and the number of heartbeats for each class are presented. According to the AAMI recommended practice, we removed the four recordings (102, 104, 107, and 217) containing paced beats from the analysis because those patients were all wearing cardiac pacemakers that could potentially interfere with the analysis. Among the 44 ECG records from the MIT/BIH arrhythmia database, there are records withpatientIDsintherangeof100to124thatreflect the common clinical ECG patterns. Other patient records with patient IDs ranging from 200 to 234 contain less common to very rare arrhythmia beats including ventricular, junctional, and supraventricular arrhythmias.

TABLE II
EACH PARTITION'S RECORDS AND THE NUMBER OF REPRESENTATIVE BEATS FOR EACH CLASS

Partition	Patients	N	S	V
DS1	101, 106, 108, 109, 112, 114, 115, 116, 118, 119, 122, 124, 201, 203, 205, 207, 208, 209, 215, 220, 223, 230	45786	941	3784
DS2	100, 103, 105, 11, 113, 117, 121, 123, 200, 202, 210, 212, 213, 214, 219, 221, 222, 228, 231, 232, 233, 234	44177	1834	3218
Total		89963	2775	7002

B. Evaluation Metrics

In this section, we present five of the most commonly used performance metrics to evaluate arrhythmia classification methods: accuracy (Acc), specificity (Spe), sensitivity (Se), positive predictive (Ppr), and F1-score. The majority class figures can significantly distort overall accuracy.As the classes for heartbeat types in the MIT-BIH database are highly imbalanced, the other four metrics are more relevant to compare the methods.

$$Acc = \frac{TP + TN}{TP + FP + TN + FN} \times 100 \quad (9)$$

$$Sen\ (Recall) = \frac{TP}{TP + FN} \times 100 \quad (10)$$

$$Spe = \frac{TN}{TN + FP} \times 100 \quad (11)$$

$$Ppr\ (Precision) = \frac{TP}{TP + FP} \times 100 \quad (12)$$

$$F1 = \frac{2 \times Sen \times Ppr}{Sen + ppr} \times 100 \quad (13)$$

where TP is true positive,TN is true negative,FP is false positive and FN is false negative. As in the competing methods, we evaluated the classification performance for N, S, and V beats individually.

In addition, receiver operating characteristics (ROCs) were used to illustrate the diagnostic ability of a binary classification system with different thresholds of discrimination (specifically SandVbeats).Due

to the wide range of thresholds, RO Ccurves can provide comprehensive information regarding performance.

C. Experimental Setup

The proposed Self-ONN model is implemented using the Fast ONN library, a fast GPU-enabled library developed in Python and PyTorch to implement and train operational neural networks. The optimized PyTorch implementation of Self-ONNs is publically shared in [57]. The Adam optimizer is used with a learning rate (LR) of 0.01 and an LR scheduler, which drops by 0.1 every 10 epochs. Kaiming initializer was used to initialize the weights of the model. The model is trained for 35 epochs with a batch size of 128. Patient-wise, 5-folds cross-validation is used to train the model and tune the hyper-parameters. We used the cross-entropy loss as the objective function for training the network [2], which is then summed over all the samples in a mini-batch. The experiments were conducted on a computer equipped with an Intel Core i7-8750H, 16GB memory, 6 GB

TABLE III
THE CONFUSION MATRIX REPRESENTS THE RESULTS OF THE BEAT CLASSIFICATION IN THE MIT-BIH ARRHYTHMIA DATABASE FOR 24 RECORDS IN DS2 (TOP) AND 24 RECORDS IN DS1 (BOTTOM)

Ground Truth	Prediction		
	N	S	V
N	43868	266	43
S	269	1529	36
V	241	36	2941

Ground Truth	Prediction		
	N	S	V
N	45355	170	299
S	122	749	72
V	91	6	3691

NVIDIA GeForce GTX 1060 graphics card, and a 2.21 Ghz processor.

Additionally, the only parameter of the 1D Self-ONN (aside from the network configuration and the common hyperparameters) is the setting of Q (the order of the Taylor polynomial), which represents the degree of non-linearity for each neuron. When this value is set high, higher-order polynomials can be generated, resulting in a higher degree of nonlinearity, but at the expense of increasing the number of network parameters and complexity. In contrast, setting it too low will result in the opposite outcome. Setting it to Q = 1 will result in Self-ONN being identical to a CNN, resulting in reduced learning and generalization performance. In order to achieve a balanced network, we choose Q = 3for all layers/neurons.

D. Performance Evaluation

Two experiments were conducted so that we could compare the model's performance in real-world scenarios and demonstrate the robustness of the model. To begin with, we treated the ECG records in DS2 as unseen patient records and used those records as the test set, whereas Ds1wasusedformodeltraining. Next, we will swap the training/evaluation sets, i.e., training on DS2andevaluationonDS1.Thethreemajorclasses(N,SandV) were considered in the experiments, while the other two classes, F and Q are ignored as in several studies [30]. In Table III, the confusion matrix is shown for all the records in both partitions of data (DS1 and DS2) of the MIT-BIH arrhythmia database using Q = 3 in all Self-ONN layers. A more extensive and accurate comparison of performance evaluation is conducted

TABLE IV
CLASSIFICATION PERFORMANCE OF THE PROPOSED 1D SELF-ONN WITH Q = 3 AND FIVE COMPETING ALGORITHMS. THE BEST RESULTS ARE IN BOLD. THE PERFORMANCE LEVELS BELOW 80% ARE SHOWN IN RED

Methods	Acc	Class (N)			Class (S)			Class (V)		
		Sen	Ppr	Spe	Sen	Ppr	Spe	Sen	Ppr	Spe
Proposed[1]	98.19	**99.30**	98.85	**99.83**	**83.37**	**83.51**	99.36	91.39	**97.38**	89.76
Proposed[2]	**98.50**	98.98	**99.53**	95.54	79.43	80.97	**99.64**	**97.44**	90.87	**99.20**
Garcia *et* al [30][1]	92.4	94	98	82.55	61.96	52.96	97.89	87.34	59.44	95.91
Sellami *et* al [58][1]	88.34	88.52	98.80	91.3	82.04	30.44	92.8	92.05	72.13	97.54
Li *et* al [59][1]	88.99	94.54	93.33	80.8	35.22	65.88	98.83	88.35	79.86	94.92
Wang *et* al [60][1]	97.68	99.04	98.64	87.95	70.75	77.0	99.51	**94.35**	95.32	99.45
Takalo *et* al [61][1]	89.91	91.89	97	76.93	62.49	55.86	98.11	89.23	50.85	94.02
Junaid *et* al [53][3]	95.99	98.48	97.39	76.82	44.01	64.50	99.01	92.96	89.62	**99.22**

1Training on DS1 and evaluation on DS2.
2Training on DS2 and evaluation on DS1.
3Using the same 1D Self-ONN network as proposed in [53], we evaluated the method for interpatient settings.

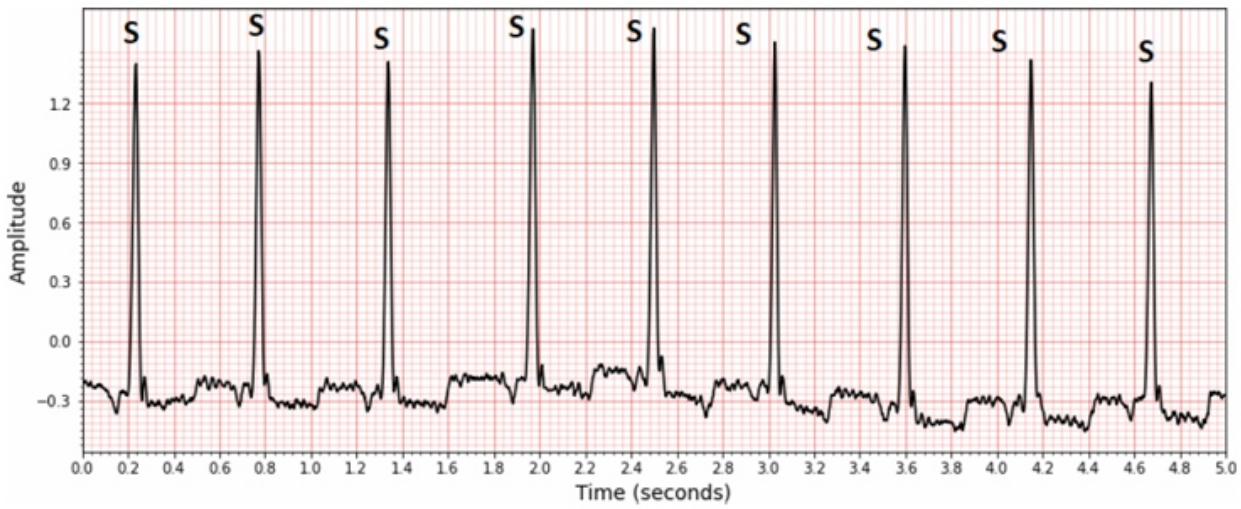

Fig. 5. Five seconds interval from patient 234's ECG record with the ground truth labels.

by comparing the performance of the proposed system with the six existing algorithms, including the self-ONN network model, presented in [53]. Table IV presents the performance metrics of all methods.

Several interesting observations can be made from the results in Table IV. First, for S-beat detection, sensitivity and positive predictivity rates are comparably lower than V-beat detection, while a high-specificity performance is achieved. The first and foremost reason for slightly worse performance in detecting S-beats as compared to V-beats is that the S class is under represented in the training data,and, hence, relatively more S beats are misclassified as normal beats. Another reason is the pattern-wise similarity of the S and N beats. Sometimes it becomes almost impossible to distinguish S-beats from the N-beats even with a trained eye. In some records (e.g., patients 202, 222, 232 and 234) several S beats are present in the sequence, yet only the first S beat displays the timing anomaly, while the others are usually perfectly symmetric but with considerably reduced time intervals. For example, Patient 234 has an episode of junctional tachycardia which last around 25 seconds. It has 50 consecutive beats of supraventricular ectopy (S-beat). The 5 seconds interval of consecutive S beats from this patient's ECG record is showning Fig. 5. This issue arises as the proposed method is limited to beat-by-beat classification. All algorithms that target beat-by-beat classification will eventually suffer in the patient's recording with consecutive S beats. But the proposed method has a superior learning capability and hence the overall performance specially for S beats is much improved compared to earlier "global" ECG classification methodologies in the literature.

The results clearly indicate that the proposed approach

achieved the topper formance in all metrics for Nand S beat classification .For V beats,the topper formance has been achieved for positive predictivity (Precision) while competitive performance levels have been achieved with the two competing methods for sensitivity and specificity. However, one can note that in [58],

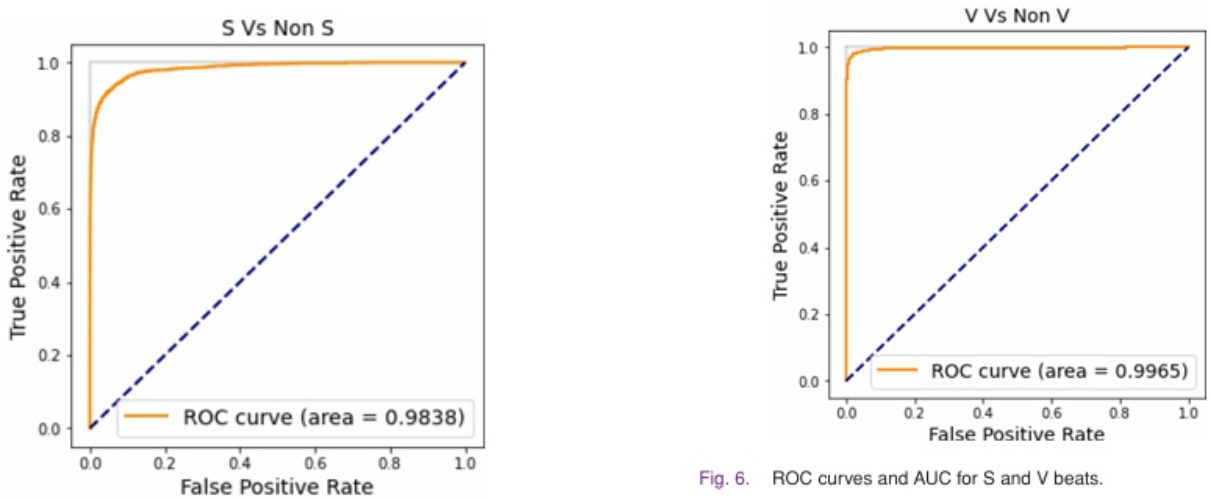

Fig. 6. ROC curves and AUC for S and V beats.

[30], and[59],slightly better specificity levels are obtained at the expense of low (<80%) positive predictivity (precision) levels as shown in red in the table. Similarly, [60] and [58] obtain slightly better sensitivity levels; however, their performance levels are quite low in other metrics, including S beat classification (e.g., [58] obtained as low as 30.44% precision level in S-beat classification). The 1D

Self-ONN model in [53] achieved the top specificity level in V beat classification; however, it failed in S beat classification too. Such poor performance levels make those competing methods useless and unreliable in clinical practice. Finally, our approach has led to significant improvements in arrhythmia beat detections, especially in S beat classification in all performance metrics over all competing methods. The performance gap sometimes reaches to 30% or even above against [30], [53], [58], [59] and [61].

In Fig. 6, the ROC curves for the proposed method are plotted to show the diagnostic ability of binary classifiers (S Vs Non-S and VVsNon-V). The ROCcurve shows the trade-off between sensitivity (or TPR) and FPR (or 1-specificity). Classifiers that give curves closer to the top-left corner indicate better performance. It is obvious from the ROC curves and area under the

TABLE V
COMPUTATIONAL COMPLEXITY OF THE NETWORKS

Methods	No. of layers	No. of Neurons	No. of trainable parameters
Proposed	4	164	23,619
Sellami *et* al [58]	9	1344	1,395,648
Li *et* al. [59]	17	876	-
Wang *et* al. [60]	5	180	26,500
Takalo *et* al. [61]	4	112	-

curve (AUC) that the proposed system is doing an excellent job in the detection of S and V beats.

E. Computational Complexity Analysis

As part of the computation complexity analysis, the total number of layers, total number of neurons, and total number of trainable parameters for each network configuration are calculated and reported in Table V.

As the numbers in the table indicate, along with the compact CNN model proposed in [61], the proposed 1D Self-ONN architecture is the most compact, shallowest network architecture with the least number of parameters. Obviously, the compact CNN model in [61] yields the worst performance level in all metrics shownin TableV .Simultaneously ,the proposed method with a similar computational complexity achieves the best performance levels with a significant margin in general.

V. CONCLUSION

We have presented a novel approach for classifying heart rhythms from ECG recordings without using anypatient-specific data. With the proposed feature injection scheme into the SelfONN network, our approach exploits both morphological and temporal information of ECG beats to maximize the classification performance. Another critical factor is that each ative neuron in an operational layer is capable of optimizing the nodal operator function of each kernel. Such neuron-level heterogeneity

further improves the network diversity and, thus, the learning performance. Finally, with the employed multiscale signal representation, a high degree of discrimination is accomplished when dealing with normal and arrhythmic ECG signals, especially the S beats. An extensive set of comparative evaluations, performed on the benchmark MIT/BIH arrhythmia database, revealed that our approach outperforms all state-ofthe-art methods usually with a significant performance gap in SVEB detection. Only the proposed approach can consistently achieve sufficiently high-performance levels required for clinical usage among all the competing methods. Finally, this pioneering study significantly narrows the performance gap between global and state-of-the-art patient-specific approaches such as [53] and [62]. Besides the performance superiority, the proposed model is also compact, and thus it can be used in real-time, especially over low-power mobile devices. Due to its highly accurate ECG classification without patient-specific labeled data, our method can serve as an additional diagnostic tool in clinical settings as well as for wearable ECG sensors such as wristbands or smart watches. In future work, we plan to further improve the performance and reduce the complexity of the model by exploring improved neuron models in Self-ONNs such as the super (generative) neuron model [63]. Additionally, we intend to expand our research on arrhythmia classification and its generalization to Holter ECGs with low-quality ECG records. In a recent study [64] we showed that the performance of R peak detection drastically decreases when algorithms that are developed for clean ECG signals are applied to noisy and low-quality Holter ECG data. For this purpose, we are planning to use the China Physiological Signal Challenge (2020) database (CPSC-DB) [65], [66], the largest Holter ECG database which contains more than one million beats.

REFERENCES

[1] "Cardiovascular diseases (CVDs)," Accessed: Feb. 4, 2022. [Online]. Available: https://www.who.int/news-room/fact-sheets/detail/cardiovas cular-diseases-(cvds)

[2] "ECG anywhere, anytime | alivecor," Accessed: Feb. 4, 2022. [Online]. Available: https://www.alivecor.co.uk/

[3] "Portable EKG monitor- Instant EKG analysis with APP– wellue," Accessed: Feb. 4, 2022. [Online]. Available: https://getwellue.com/products/ duoek-hand-held-wearable-ekg-tracker?currency=EUR

[4] M. Gabbouj et al., "Robust peak detection for holter ECGs by self organized operational neural networks," IEEE Trans. Neural Netw. Learn. Syst., 2022, doi: 10.1109/TNNLS.2022.3158867.

[5] M. U. Zahid et al., "Robust R-Peak detection in low-quality holter ECGs using 1D convolutional neural network," IEEE Trans. Biomed. Eng., vol. 69, no. 1, pp. 119–128, Jan. 2022, doi: 10.1109/TBME.2021.3088218.

[6] S. M. Mathews, C. Kambhamettu, and K. E. Barner, "A novel application of deep learning for single-lead ECG classification," Comput. Biol. Med., vol. 99, pp. 53–62, Aug. 2018, doi: 10.1016/J.COMPBIOMED.2018.05.013.

[7] P. De Chazal, M. O'Dwyer, and R. B. Reilly, "Automatic classification of heartbeats using ECG morphology and heartbeat interval features," IEEE Trans. Biomed. Eng., vol. 51, no. 7, pp. 1196–1206, Jul. 2004, doi: 10.1109/TBME.2004.827359.

[8] Y. H. Hu, S. Palreddy, and W. J. Tompkins, "A patient-adaptable ECG beat classifier using a mixture of experts approach," IEEE Trans. Biomed. Eng., vol. 44, no. 9, pp. 891–900, Sep. 1997, doi: 10.1109/10.623058.

[9] M.M.A.Rahhaletal.,"Deep learning approach for active classification of electrocar diogram signals," Undefined, vol. 345, pp. 340–354, Jun. 2016, doi: 10.1016/J.INS.2016.01.082.

[10] C. Ye, B. V. K. Vijaya Kumar, and M. T. Coimbra, "Heartbeat classification using morphological and dynamic features of ECG signals," IEEE Trans. Biomed. Eng., vol. 59, no. 10, pp. 2930–2941, Oct. 2012, doi: 10.1109/TBME.2012.2213253.

[11] P. De Chazal, M. O'Dwyer, and R. B. Reilly, "Automatic classification of heartbeats using ECG morphology and heartbeat interval features," IEEE Trans. Biomed. Eng., vol. 51, no. 7, pp. 1196–1206, Jul. 2004, doi: 10.1109/TBME.2004.827359.

[12] E. J. da S. Luz et al., "ECG-based heartbeat classification for arrhythmia detection: A survey," Comput. Methods Programs Biomed., vol. 127, pp. 144–164, Apr. 2016, doi: 10.1016/J.CMPB.2015.12.008.

[13] M. Llamedo and J. P. Martínez, "Heartbeat classification using feature selection driven by database generalization criteria," IEEE Trans. Biomed. Eng., vol. 58, no. 3, pp. 616–625, Mar. 2011, doi: 10.1109/TBME.2010.2068048.

[14] R. Hoekema, G. J. H. Uijen, and A. Van Oosterom, "Geometrical as pects of the interindividual variability of multilead ECG recordings," IEEE Trans. Biomed. Eng., vol. 48, no. 5, pp. 551–559, May 2001, doi: 10.1109/10.918594.

[15] P. de Chazal and R. B. Reilly, "A patient-adapting heartbeat classifier using ECG morphology and heartbeat interval features," IEEE Trans. Biomed. Eng., vol. 53, no. 12, pp. 2535–2543, Dec. 2006, doi: 10.1109/TBME.2006.883802

[16] J. Chung et al., "Empirical evaluation of gated recurrent neural networks on sequence modeling," Dec. 2014.

[17] B.H.TraceyandE.L.Miller,"Nonlocal means denoising of ECG signals," IEEE Trans. Biomed. Eng., vol. 59, no. 9, pp. 2383–2386, Sep. 2012, doi: 10.1109/TBME.2012.2208964.

[18] S. Kiranyaz, T. Ince, and M. Gabbouj, "Real-time patient-specific ECG classification by 1-D convolutional neural networks," IEEE Trans. Biomed. Eng., vol. 63, no. 3, pp. 664–675, Mar. 2016,

doi: 10.1109/TBME.2015.2468589.

[19] S. S. Xu, M. W. Mak, and C. C. Cheung, "I-vector-based patient adaptation of deep neural networks for automatic heartbeat classification," IEEE J. Biomed. Health Inform., vol. 24, no. 3, pp. 717–727, Mar. 2020, doi: 10.1109/JBHI.2019.2919732.

[20] K. I. Minami, H. Nakajima, and T. Toyoshima, "Real-time discrimination of ventricular tachyarrhythmia with Fourier-transform neural network," IEEE Trans. Biomed. Eng., vol. 46, no. 2, pp. 179–185, Feb. 1999, doi: 10.1109/10.740880.

[21] O.T.Inan,L.Giovangrandi,andG.T.A.Kovacs,"Robustneural-network based classification of premature ventricular contractions using wavelet transformand timing interval features,"IEEETrans.Biomed.Eng.,vol.53, no. 12, pp. 2507–2515, Dec. 2006, doi: 10.1109/TBME.2006.880879.

[22] S. Osowski, L. T. Hoai, and T. Markiewicz, "Support vector machine-based expert system for reliable heartbeat recognition," IEEE Trans. Biomed. Eng., vol. 51, no. 4, pp. 582–589, Apr. 2004, doi: 10.1109/TBME.2004.824138.

[23] O.Wieben,V.X.A fonso,andW.J.Tompkins,"Classification of premature ventricular complexes using filter bank features,induction of decision trees and a fuzzy rule-based system," Med. Biol. Eng. Comput., vol. 37, no. 5, pp. 560–565, 1999, doi: 10.1007/BF02513349.

[24] P. De Chazal and R. B. Reilly, "A patient-adapting heartbeat classifier using ECG morphology and heartbeat interval features," IEEE Trans. Biomed. Eng., vol. 53, no. 12, pp. 2535–2543, Dec. 2006, doi: 10.1109/TBME.2006.883802.

[25] M. Llamedo and J. P. Martínez, "Heartbeat classification using feature selection driven by database generalization criteria," IEEE Trans. Biomed. Eng., vol. 58, no. 3, pp. 616–625, Mar. 2011, doi: 10.1109/TBME.2010.2068048.

[26] C. Ye, B. V. K. V. Kumar, and M. T. Coimbra, "Heartbeat classif ication using morphological and dynamic features of ECG signals," IEEE Trans. Biomed. Eng., vol. 59, no. 10, pp. 2930–2941, Oct. 2012, doi: 10.1109/TBME.2012.2213253.

[27] G. De Lannoy et al., "Weighted conditional random fields for supervised interpatient heartbeat classification," IEEE Trans. Biomed. Eng., vol. 59, no. 1, pp. 241–247, Jan. 2012, doi: 10.1109/TBME.2011.2171037.

[28] H. Khorrami and M. Moavenian, "A comparative study of DWT, CWT and DCT transformations in ECG arrhythmias classification," Expert Syst. Appl., vol. 37, no. 8, pp. 5751–5757, Aug. 2010, doi: 10.1016/J.ESWA.2010.02.033.

[29] S. Karpagachelvi, M. Arthanari, and M. Sivakumar, "Classification of electrocardiogram signals with support vector machines and extreme learning machine," Neural Comput. Appl., vol. 21, no. 6, pp. 1331–1339, Sep. 2012, doi: 10.1007/S00521-011-0572-Z.

[30] G. Garcia et al., "Inter-patient ECG heartbeat classification with temporal VCG optimized by PSO," Sci. Rep., vol. 7, no. 1, pp. 1–11, Sep. 2017, doi: 10.1038/s41598-017-09837-3.

[31] S. Kiranyaz et al., "1-D convolutional neural networks for signal process ingapplications," inProc.IEEEInt.Conf.Acoust.,SpeechSignalProcess., 2019, pp. 8360–8364. doi: 10.1109/ICASSP.2019.8682194.

[32] S. Kiranyaz et al., "1D convolutional neural networks and applications: A survey," Mech. Syst. Signal Process., vol. 151, Apr. 2021, Art. no. 107398, doi: 10.1016/j.ymssp.2020.107398.

[33] T.Inceetal., "Real-time motorfaultdetection by1-Dconvolutionalneural networks," IEEE Trans. Ind. Electron., vol. 63, no. 11, pp. 7067–7075, Nov. 2016, doi: 10.1109/TIE.2016.2582729.

[34] S. Kiranyaz, T. Ince, and M. Gabbouj, "Personalized monitoring and advance warning system for cardiac arrhythmias," Sci. Rep., vol. 7, no. 1, pp. 1–8, Dec. 2017, doi: 10.1038/s41598-017-09544-z.

[35] S. Kiranyaz, T. Ince, and M. Gabbouj, "Real-time patient-specific ECG classification by 1-D convolutional neural networks," IEEE Trans. Biomed. Eng., vol. 63, no. 3, pp. 664–675, Mar. 2016, doi: 10.1109/TBME.2015.2468589.

[36] "AAMI- ECAR- testing and reporting performance results of ventricular arrhythmia detection algorithms | engineering360," Accessed: Mar. 23, 2022. [Online]. Available: https://standards.globalspec.com/std/ 733772/ECAR

[37] D. Zhang et al., "An ECG heartbeat classification method based on deep convolutional neural network," J. Healthcare Eng., vol. 2021, pp. 1–9, 2021, doi: 10.1155/2021/7167891.

[38] L. Guo, G. Sim, and B. Matuszewski, "Inter-patient ECG classification with convolutional and recurrent neural networks," Biocybern. Biomed. Eng., vol. 39, no. 3, pp. 868–879, Jul. 2019, doi: 10.1016/J.BBE. 2019.06.001.

[39] S. S. Xu, M. W. Mak, and C. C. Cheung, "Towards end-to-end ECG classification with raw signal extraction and deep neural networks," Undefined, vol. 23, no. 4, pp. 1574–1584, Jul. 2019, doi: 10.1109/ JBHI.2018.2871510.

[40] U. R. Acharya et al., "A deep convolutional neural network model to classify heartbeats," Comput. Biol. Med., vol. 89, pp. 389–396, Oct. 2017, doi: 10.1016/J.COMPBIOMED.2017.08.022.

[41] U. R. Acharya et al., "Automated detection of arrhythmias us ing different intervals of tachycardia ECG segments with convolutional neural network," Inf. Sci., vol. 405, pp. 81–90, Sep. 2017, doi: 10.1016/J.INS.2017.04.012.

[42] U. R. Acharya et al., "Automated detection of arrhythmias us ing different intervals of tachycardia ECG segments with convolutional neural network," Inf. Sci., vol. 405, pp. 81–90, Sep. 2017, doi: 10.1016/J.INS.2017.04.012.

[43] L. Guo, G. Sim, and B. Matuszewski, "Inter-patient ECG classif ication with convolutional and

recurrent neural networks," Biocybern. Biomed. Eng., vol. 39, no. 3, pp. 868–879, Jul. 2019, doi: 10.1016/J.BBE.2019.06.001.

[44] S. Kiranyaz et al., "Operational neural networks," Neural Comput. Appl., vol. 32, no. 11, pp. 6645–6668, Jun. 2020, doi: 10.1007/S00521020-04780-3.

[45] D. T. Tran et al., "Knowledge transfer for face verification using heterogeneous generalized operational perceptrons," in Proc. Int. Conf. Image Process., Sep. 2019, pp. 1168–1172, doi: 10.1109/ICIP.2019.8804296.

[46] D. T. Tran et al., "Heterogeneous multilayer generalized operational perceptron," IEEE Trans NeuralNetwLearnSyst,vol.31,no.3,pp. 710–724, Mar. 2020, doi: 10.1109/TNNLS.2019.2914082.

[47] S. Kiranyaz et al., "Exploiting heterogeneity in operational neural networks by synaptic plasticity," Neural Comput. Appl., vol. 33, no. 13, pp. 7997–8015, Jul. 2021, doi: 10.1007/S00521-020-05543-W/FIGURES/18.

[48] S. Kiranyaz et al., "Progressive operational perceptrons," Neurocomputing, vol. 224, pp. 142–154, Feb. 2017, doi: 10.1016/J.NEUCOM. 2016.10.044.

[49] S. Kiranyaz et al., "Generalized model of biological neural networks: Progressive operational perceptrons," in Proc. Int. Joint Conf. Neural Netw., 2017, pp. 2477–2485, doi: 10.1109/IJCNN.2017.7966157.

[50] S. Kiranyaz et al., "Exploiting heterogeneity in operational neural networks by synaptic plasticity," Neural Comput. Appl., vol. 33, no. 13, pp.7997–8015, Jul. 2021, doi: 10.1007/S00521-02005543-W/FIGURES/18

[51] S. Kiranyaz et al., "Self-organized operational neural networks with generative neurons," Neural Netw., vol. 140, pp. 294–308, Apr. 2020, doi: 10.1016/j.neunet.2021.02.028.

[52] J.Malik,S.Kiranyaz,andM.Gabbouj,"Self-organize doperational neural networks for severe image restoration problems," Neural Netw., vol. 135, pp. 201–211, Aug. 2020, doi: 10.1016/j.neunet.2020.12.014.

[53] J. Malik et al., "Real-time patient-specific ECG classification by 1D self operational neural networks," IEEE Trans. Biomed. Eng., vol. 69, no. 5, pp. 1788–1801, May 2022, doi: 10.1109/TBME.2021.3135622.

[54] M. Gabbouj et al., "Robust peak detection for holter ECGs by self organized operational neural networks," IEEE Trans. Neural Netw. Learn. Syst., to be published, doi: 10.1109/TNNLS.2022.3158867.

[55] "MIT-BIH noise stress test database v1.0.0," Accessed: Dec. 23, 2020. [Online]. Available: https://www.physionet.org/content/nstdb/1.0.0/

[56] "MIT-BIH arrhythmia database v1.0.0,".

[57] "junaidmalik09/fastonn: FastONN- Python based open-source GPU implementation for

operational neural networks," Accessed: May 15, 2022. [Online]. Available: https://github.com/junaidmalik09/fastonn

[58] A. Sellami and H. Hwang, "A robust deep convolutional neural network with batch-weighted loss for heartbeat classification," Expert Syst. Appl., vol. 122, pp. 75–84, May 2019, doi: 10.1016/J.ESWA.2018.12.037.

[59] Y. Li, R. Qian, and K. Li, "Inter-patient arrhythmia classification with improved deep residual convolutional neural network," Comput. Methods Programs Biomed., vol. 214, Feb. 2022, Art. no. 106582, doi: 10.1016/J.CMPB.2021.106582.

[60] T. Wang et al., "Automatic ECG classification using continuous wavelet transform and convolutional neural network," Entropy, vol. 23, no. 1, Jan. 2021, Art. no. 119, doi: 10.3390/E23010119.

[61] J. Takalo-Mattila, J. Kiljander, and J. P. Soininen, "Inter-patient ECG classification using deep convolutional neural networks," in Proc. 21st Euromicro Conf. Digit. System Des., 2018, pp. 421–425, doi: 10.1109/DSD.2018.00077.

[62] S. Kiranyaz, T. Ince, and M. Gabbouj, "Real-time patient-specific ECG classification by 1-D convolutional neural networks," IEEE Trans. Biomed. Eng., vol. 63, no. 3, pp. 664–675, Mar. 2016, doi: 10.1109/TBME.2015.2468589.

[63] S. Kiranyaz et al., "Super neurons," Aug. 2021.

[64] M. U. Zahid et al., "Robust R-Peak detection in low-quality holter ECGs using 1D convolutional neural network," IEEE Trans. Biomed. Eng., vol. 69, no. 1, pp. 119–128, Jan. 2022, doi: 10.1109/TBME.2021.3088218.

[65] Z. Cai et al., "An open-access long-term wearable ECG database for premature ventricular contractions and supraventricular premature beat detection," J. Med. Imag. Health Inform., vol. 10, no. 11, pp. 2663–2667, Nov. 2020, doi: 10.1166/JMIHI.2020.3289.

[66] "CSPC2020 page- icbeb2020," Accessed Jun. 20, 2022. [Online]. Available: http://2020.icbeb.org/CSPC2020

ISSN : 2582-7405

In Silico Study of Local Electrical Impedance Measurements in the Atria Towards Understanding and Quantifying Dependencies in Human

Laura Anna Unger , Carmen Martínez Antón Michael Kircher, Olaf Dössel , Michael Stritt, Reza Wakili, Annika Haas, , Fellow, IEEE, and Armin Luik

ABSTRACT

Background: Electrical impedance measure ments have become an accepted tool for monitoring intracardiac radio frequency ablation. Recently, the longestablished generator impedance was joined by novel local impedance measurement capabilities with all electrical circuit terminals being accommodated with in the catheter. Objective: This work aims at in silico quantification of distinct influencing factors that have remained challenges due to the lack of ground truth knowledge and the superposition of effects in clinical settings. Methods: We introduced a highly detailed in silico model of two local impedance enabled catheters, namely IntellaNav MiFi OI and IntellaNav Stablepoint, embedded in a series of clinically relevant environments. Assigning material and frequency specific conductivities and subsequently calculating the spread of the electrical field with the finite element method yielded in silico local impedances. The in silico model was validated by comparison to in vitro measurements of standardized sodium chloride solutions. We then investigated the effect of the withdrawal of the catheter into the transseptal sheath, catheter-tissue interaction, insertion of the catheter into pulmonary veins, and catheter irrigation. Results: All simulated setups were in line with in vitro experiments and in human measurements and gave detailed insight into determinants of local impedance changes as well as the relation between values measured with two different devices. Conclusion: The in silico environment provedtobe capable of resembling clinical scenarios and quantifying local impedance changes. Significance: The tool can assists the interpretation of measurements in humans and has the potential to support future catheter development.

Index Terms—Ablation, atrial substrate, bioimpedance, cardiac electrophysiology, local impedance, radio frequency ablation.

I. INTRODUCTION

ELECTRICAL impedance measurements have a long his tory in the medical and biomedical field. Historical studies have shown that different kinds of biological tissues are characterized by different conductivity spectra [1] attributed to the microscopic composition of the materials [2]. Besides the composition of the material and the measurement frequency, electrode arrangement and temperature are major determinants of the measured impedance.

During invasive cardiac electro physiological studies, genera tor impedance measurements have been an established method to monitor the delivery of radio frequency energy during ablation since decades [3], [4]. The transthoracic impedance of the radio frequency energy delivery pathway between an intracardiac and a cutaneous dispersive electrode assists differentiation of tissue contact during ablation. However, the bulk impedance of the torso blurs measurements [5], [6] and impedes detailed assessment of tissue characteristics in the region of interest next to the catheter. Recently, two novel catheters have been introduced to the market that aim at a more locally focused impedance assessment in the vicinity of the catheter with all injecting and measuring electrodes being built into the intracardiac catheter itself [4]. The radio frequency ablation catheters IntellaNav MiFi OI [7] and Intella Nav Stablepoint [8] (Boston Scientific, Malborough, MA, USA) come with a four-electrode and a three-electrode impedance measurement circuit implemented within the catheter, respectively. During ablation, the so-calledDirectSensetechnologymeasuresthemagnitudeofthe local impedance (LI). An LI drop resulting from a combination of resistivet issue heating and subsequent my ocardial destruction and lesion formation is used as a surrogate for lesion quality and durability [7], [9]. Compared to the trans thoracic generator impedance, the LI emphasizes local changesin impedance while beinglesssusceptibletofarfieldartifacts[9]–[12].Despiteanincreased influence of the local surroundings on the measurement compared to the generator impedance, the LI is still sensitive to the three-dimensional arrangement of materials and their properties surrounding the catheter [13]. LI may therefore not be mistaken for lumped impedance measurements ,which condense all influencing properties to an infinitesimal element. Besides the monitoring of ablation lesion formation, LI has also shown potential to characterize cardiac tissue and differentiate between healthy myocardium and fibrotic or scar tissue [10]–[12]. Atrial ibrillation as the most common sustained cardiac arrhythmia poses a major burden for both patients and global health care systems. Since current treatment approaches result in unsatisfactory success rates, novel methods of tissue characterization such as the LI need.

A major challenge in the expansion of the diagnostic value of intracardiac LI measurements are confounding factors. Not only different tissue compositions but also the distance and angle between the catheter and the tissue, the surrounding tissue geometry, an overlap of catheter and transseptal sheath, and sodium chloride (NaCl) solution irrigation influence the measurement, amongst others. Many of these effects can be observed in in human studies but lack quantification due to the superposition of multiple effects and an unknown ground truth. Therefore, the differentiation between the target measure and confounding factors has remained uncertain. In vitro and ex vivo experiments can help to shed light on different scenarios but are costly and depending on the experimental setup, the underlying ground truth still remains under-determined.

In this work, we present for the first time a highly detailed in silico framework that models the Intella Nav MiFi OI catheter and the IntellaNav Stablepoint catheter in combination with different clinically relevant surroundings. After validation of the framework by in vitro measurements in standardized setups, clinically relevant scenarios such as the effect of the distance and angle between catheter and tissue, scar tissue, the insertion of the catheter into a pulmonary vein or a transseptal sheath, and NaCl solution irrigation were investigated and compared to in vitro and in human measurements. With a highly detailed comparison between different catheter geometries and the investigation of isolated scenarios to quantify various clinically relevant effects, this work paves the way for an inexpensive enhancement of the understanding of intracardiac LI measurements and future catheter development.

II. METHODS

A. In Silico — Geometrical Setup

Both clinically available LI enabled radio frequency ab lation catheters were modeled in high detail as depicted in Fig. 1(a) to (d). Measures were taken from product specification sheets [14], [15] as well as calibrated photographs yielding a resolution below 100 µm.

The IntellaNav MiFi OI comes with a 4.5 mm tip electrode, three ring electrodes of 1.3 mm width and 2.5 mm spacing,

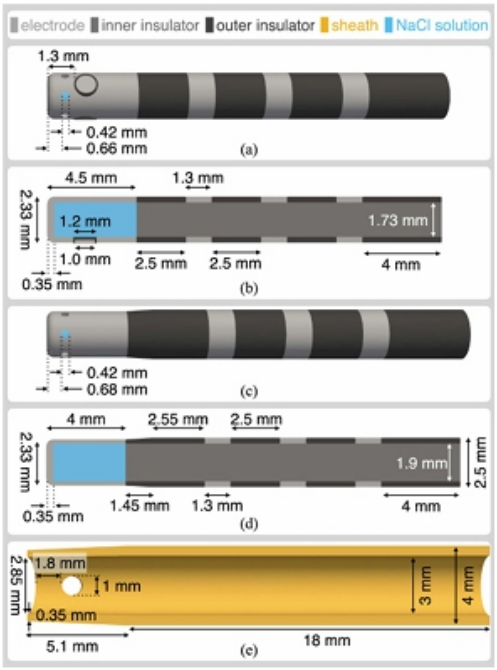

Fig. 1. Geometrical models of LI enabled radio frequency ablation catheters and a transseptal sheath. (a) 3D model of the IntellaNav MiFi OI. (b) Cross-section of the IntellaNav MiFi OI. (c) 3D model of the IntellaNav Stablepoint. (d) Cross-section of the IntellaNav Stablepoint. (e) Cross-section of a transseptal sheath including one out of two irrigation holes.

three evenly distributed mini electrodes of 0.8 mm diameter embedded in the tip electrode, six irrigation holes, and a cooling chamber filled with NaCl solution. The interior of the catheter is electrically isolated from the electrodes and accommodates thin electrical and mechanical steering wires. While neglecting the latter, the interior of the catheter shaft was filled with insulating material in the model.

The Intella Nav Stable point is similarly composed of a 4 mm tip electrode, three ring electrodes of 1.3 mm width and4.0mm| 2.5 mm | 2.5 mm spacing, six irrigation holes, and a cooling chamber filled with NaCl solution. The tip does not embed any mini electrodes. Proximal to the tip, the diameter expands conically to the shaft diameter.The existence of the force sensing spring between the tip electrode and the distal ring electrode in the interior of the catheter [8] was assumed to be negligible with respect to the spread of the electrical field outside the catheter. Therefore, the interior of the catheter shaft was filled with insulating material as well.

A transseptal sheath was implemented on the model of the 8.5 F Agilis NxT steerable introducer (Abbott, Chicago, IL, USA) as depicted in Fig. 1(e). Detailed measures of the implemented catheter and sheath geometries are shown in Fig. 1. The respective catheter was embedded in a 140 mm 140mm ×140mmboxfilledwitheitherbloodorNaClsolution

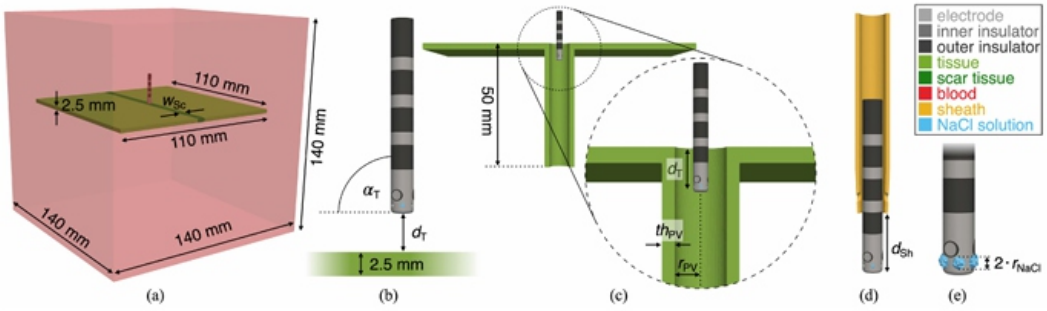

Fig. 2. Simulation setups. All setups are depicted at the example of the IntellaNav MiFi OI and were equally conducted with the IntellaNav Stablepoint. (a) Tissue patch with line of scar within the surrounding blood box. (b) Variation of distance and angle between catheter and tissue. (c) Insertion of the catheter into the PV. (d) Insertion of the catheter into the transseptal sheath. (e) Irrigation with NaCl solution.

as displayed in Fig. 2(a) for all simulation setups. Geometry definition and tetra hedral meshing was done with Gmsh (version 4.5.6) [16]. Mesh resolution was adapted to the size of local structures being the highest at the Intella Nav MiFi OI mini elec trodes and the lowest at the outer boundary of the box. The meshes were comprised of 2.5 million to 5 million tetrahedral elements.

1) Standardized NaCl Solutions: Either catheter was placed in the surrounding box filled with NaCl solution of eight different molar concentrations starting from 0.02 mol1 0.01 mol l up to 0.09 mol/1.

2) Trans septal Steerable Sheath: Within a surrounding box filled with blood, either catheter was withdrawn into the transseptal sheath model with the distance dSh describing the distance between the catheter tip and the distal edge of the sheath (compare Fig. 2(d)). Negative distances describe the withdrawal of the catheter into the sheath. dSh was varied from −2mmin steps of 0.5 mm up to 19.5 mm.

3) Tissue: Either catheter was placed in the surrounding box f illed with blood. A square patch of tissue

measuring 110 mm × 110 mm×2.5mmwasplaced below the catheter resembling a piece of atrial myocardial tissue of typical wall thickness [17] (compare Fig. 2(a)). The distance dT between the catheter and the tissue was varied from −2mmto10mminstepsof0.5mm (compare Fig. 2(b)). Negative distances represented an immersion of the catheter into the tissue. Mechanical interaction was not modeled. Instead, the catheter simply displaced the tissue. In a second step, the angle αT between the catheter and the tissue was varied from 0◦ to 180◦ in steps of 15◦. For $90^\circ < \alpha T \leq 180^\circ$, one of the mini electrodes pointed directly towards the tissue. For $0^\circ \leq \alpha T < 90^\circ$, the two remaining electrodes were pointed towards — but not directly towards — the tissue (compare Fig. 2(b)). The pivot was located at the intersection of the catheter's distal plane and the outer wall of the catheter shaft at the left and the right, respectively. The experiment was conducted for five different distances between catheter and tissue $dT \in \{0.0mm, 0.5mm, 1.0mm, 2.0mm, 4.0mm\}$.

4) Transmural Lesion: The general tissue setup as described above was complemented by a central line of scar tissue of width $wSc \in \{3mm, 6mm\}$ (compareFig.2(a))representing ablated tissue from a previous procedure or natively developed myocardial scar. For two different distances between catheter and tissue (dT =0mm and dT =1mm), either catheter was moved perpendicularly to the line of scar starting at a distance to the center of the line of scar of dSc = −10mm, crossing the line of scar for dSc =0mm up to a distance of dSc =10mm at a default step size of 1 mm and a decreased step size of 0.5 mm for $|dSc| < 2mm$.

5) Pulmonary Vein: The insertion of either catheter into a pulmonary vein (PV) was simulated by extending the general tissue setup by a perpendicular tube filled with blood (compare Fig. 2©). For a PV wall thickness thPV =2mm, four different inner PV radii $rPV \in \{2mm, 3mm, 4mm, 6mm\}$ were implemented. For rPV =6mm, additional PV wall thicknesses of $thPV \in \{1mm, 3mm, 4mm\}$ weremodeled.Eithercatheterwas inserted into the PV quantified by the distanced T to the surface of the tissue. Negative distances represent states with the respective catheter being inside the PV while positive distances represent states of catheter elevation above the tissue. dT was varied from −20mm(full immersion) to 10 mm (full extraction) in steps of 1 mm.

6) Irrigation: Catheter irrigation was modeled by placing a sphere of physiological NaCl solution at each center of the irrigation holes displacing all encircled blood elements(compare Fig. 2(e)). The radius rNaCl of the NaCl spheres was varied from 0 mmto2mminsteps of 0.05 mm.

B. In Silico — Material Properties

The tetrahedral elements of the geometrical meshes were assigned conductivity values characteristic for the respective material at 14.5 kHz as summarized in Table I.Due to the significant dependency of conductivities on the temperature, the latter had to be regarded for. The in vitro setups with NaCl solutions of different concentrations were conducted at different temperatures and compared to in

silico experiments based on conductivities published by Gabriel et al. [1], which lack an explicit statement about temperature. Comparing to the conductivity of 0.5 % NaCl solution given for 20 ◦C [18] suggests that Gabriel et al. measured at

TABLE I
CONDUCTIVITIES OF RELEVANT MATERIALS AT 14.5 KHZ

Material	Conductivity σ (S/m)	Temperature (°C)	Reference
metallic electrode	400, 000		[20]
insulator	10^{-7}		
sheath	10^{-7}		
blood	0.700	BT	[21] [22]
myocardial tissue	0.164	BT	[21] [22]
connective tissue (scar)	0.387	BT	[21] [22]
NaCl 0.020 $\frac{\text{mol}}{\text{l}}$ (0.12 %)	0.220	T_{Gab}	[1]
NaCl 0.030 $\frac{\text{mol}}{\text{l}}$ (0.18 %)	0.330	T_{Gab}	[1]
NaCl 0.040 $\frac{\text{mol}}{\text{l}}$ (0.23 %)	0.430	T_{Gab}	[1]
NaCl 0.050 $\frac{\text{mol}}{\text{l}}$ (0.29 %)	0.530	T_{Gab}	[1]
NaCl 0.060 $\frac{\text{mol}}{\text{l}}$ (0.35 %)	0.620	T_{Gab}	[1]
NaCl 0.070 $\frac{\text{mol}}{\text{l}}$ (0.41 %)	0.720	T_{Gab}	[1]
NaCl 0.080 $\frac{\text{mol}}{\text{l}}$ (0.47 %)	0.800	T_{Gab}	[1]
NaCl 0.086 $\frac{\text{mol}}{\text{l}}$ (0.50 %)	0.820	20	[18]
NaCl 0.090 $\frac{\text{mol}}{\text{l}}$ (0.53 %)	0.880	T_{Gab}	[1]
NaCl 0.154 $\frac{\text{mol}}{\text{l}}$ (0.90 %)	1.444	20	
NaCl 0.171 $\frac{\text{mol}}{\text{l}}$ (1.00 %)	1.600	20	[18]

BT: Body Temperature; T_{Gab}: Measurement Temperature in Gabriel et al. [1]

a slightly higher temperature TGab (compare Table I). With a temperature coefficient of approximately 2.1% ◦ [19] and the reference values from [18], Gabriel et al. most likely measured NaCl solutions significantly below body temperature as opposed to their measurements of biological tissue. Since the data set [1] was consistent in itself, the exact temperature was deemed insignificant for the validation setups with NaCl solutions of different concentrations.

All other in silico experiments were parameterized with conductivities given for blood, myocardial tissue, and scar tissue at body temperature (BT) as well as physiological 0.9 % NaCl solution for catheter irrigation at an approximate lab temperature of 20 ◦C as listed in Table I. Due to the lack of an explicit reference for the conductivity of physiological 0.9 % NaCl solution, the latter was linearly inter polated from the conductivities of 0.5 % and 1 % NaCl solution at 20 ◦C [18] as listed in Table I.

C. In Silico — Impedance Forward Simulation

The spread of the electrical field was simulated with the software EIDORSv3.10[23] and MATLAB R2021 a (The Math Works, Inc., Natick, MA, USA). In short, EIDORS solves the Poisson equation with a finite element model F. The injection currents are given as boundary conditions. The current density and the potential field are the solution. The voltage v between two electrodes is extracted as the potential difference and is dependent on the given conductivities σ at the elements of the model and the stimulation pattern q of the electrode model with v =F(σ,q)[23].

Stimulation and measurement circuits were defined according to the clinical system: A four-terminal

circuit with current injection between the distal tip electrode and the proximal ring electrode was combined with measurements between the mini electrodes and the distal ring electrode for the Intella Nav MiFi OI [7]. The three voltage measurements resulting from either mini electrode to the distal ring electrode were reduced to their maximum value following the clinical system. The Intella Nav Stable point was set up as a three-terminal circuit with current injection between the distal tip electrode and the proximal ring electrode and voltage measurement between the distal tip electrode and the distal ring electrode.

An alternating current of 5μA peak-to-peak amplitude at 14.5 kHz was modeled. The complete electrode model was used [24]. The resulting voltage amplitude |v| was then divided by the amplitude of the injected current to obtain LI as the magnitude of the impedance.

D. In Vitro Setup

All measurements were conducted with the Rhythmia Hdx system (Boston Scientific, Malborough, MA, USA), the IntellaNav MiFi OI, and the IntellaNav Stablepoint. To validate the simulation framework, NaCl solutions of different concentrations and known conductivity σ were prepared. The molar mass as given in [1] starting from 0.02 mol l up to 0.09 mol l in steps of 0.01 mol

l was converted to weight percentages. The respective amount of NaCl was weighed out with a scale of 10−3 g resolution and 10−3 g precision and dissolved in 250 ml of de-ionized water. For all concentrations, the NaCld is solved completely and form edanaqueous solution. Athermo meter of 0.1◦Cresolution was used to keep track of the solution's temperature. The LI was measured with both catheters in each solution at 7 to 13 different temperatures between 18.2 ◦C and 38.8 ◦C. For comparability, the LI at three different temperatures — namely 21 ◦C, 25 ◦C, and 36 ◦C — was interpolated and compared to the simulated results for the respective NaCl solutions.

Additionally, the behavior of LI with tissue contact was measured in vitro. A tissue phantom composed of 100 ml de-ionized water, 3 g agar-agar, and 0.0499 g NaCl [25] was prepared. The expected conductivity of 0.16 S m at 25 ◦C matched the conductivity of cardiac tissue at 14.5 kHz well. Since in vitro measurements were taken at 20.5 ◦C in this work, the actual conductivity might have deviated slightly due to the difference in temperature. Typical temperature coefficients reported for similar materials justified to neglect deviations caused by the described change in temperature [19], [26]. Additionally, a piece of smooth left atrial porcine tissue was used. The tissue phantom and the tissue sample were mounted at an elevated ring in order not to disturb measurements by the mount in 0.35 % NaCl solution. Either catheter was positioned at the tissue phantom and the tissue sample in orthogonal and parallel orientation.

The effect of catheter irrigation with physiological NaCl solution on LI was investigated by increasing the flow rate of the HAT500irrigation pump (Osypka AG, Rheinfelden, Germany) from 0 ml min to 2

ml min and 17 ml min in a 250 ml bath of 0.35 % NaCl solution. A flow rate of 2 ml min is clinically applied in standby mode while the flow rate is typically adjusted to 17 ml ablation. The bath model did not include circulation.

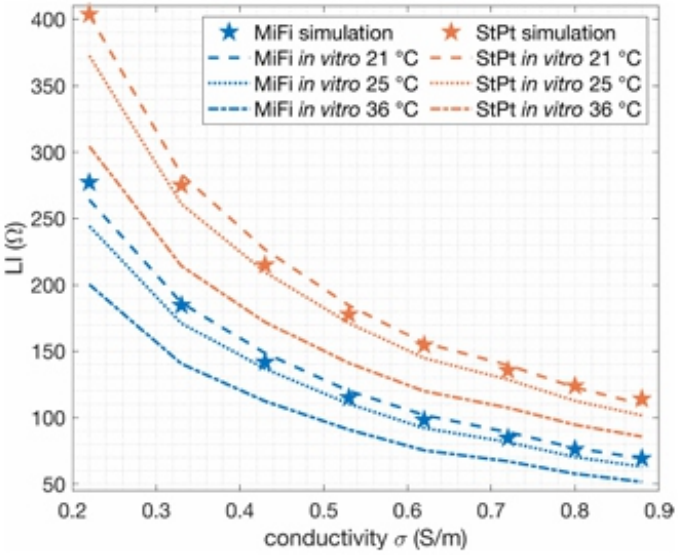

E. In Human Setup

Clinical measurements complemented the in silico analysis of catheter sheath interaction and its effect on the LI. Either catheter was located in the left atrium passing the inter-atrial septum via the transseptal sheath, namely the Agilis NxT steerable introducer. An X-ray scan verified that the proximal ring electrode was outside of the sheath. Starting from a central position in the left atrial bloodpool without endocardial contact, the catheter was gradually pulled back into the she a that constant speed while recording the LI. Clinical LI was represented by its moving average calculated with a sliding window of 1.5 s width as provided by the electroanatomical mapping system. All in human measurements were approved by the local ethics committee and were conducted in accordance with the Declaration of Helsinki. Written informed consent was obtained from all patients.

III. RESULTS

A. Aqueous NaCl Solutions

Fig. 3 presents LI values measured in vitro in aqueous NaCl solutions prepared according to Table I at 21 ◦C, 25 ◦C, and 36 ◦C along with simulated LI values for in silico setups of the corresponding molar concentrations. Higher temperatures yielded lower LI values for constant NaCl concentration. In vitro and in silico experiments followed the same hyperbolic-like trend with decreasing LI values for increasing conductivity. Simulated LI values predominantly fell between the corresponding in vitro measurements at 21 ◦C and 25 ◦C for both catheters with a median deviation of −2.7 Ω and −2.8 Ω from

the measurements at 21 ◦C for the IntellaNav MiFi OI and the IntellaNav Stablepoint, respectively. A negative deviation is in line with the assumption of 20 ◦C <Tgab 36 ◦C as stated in

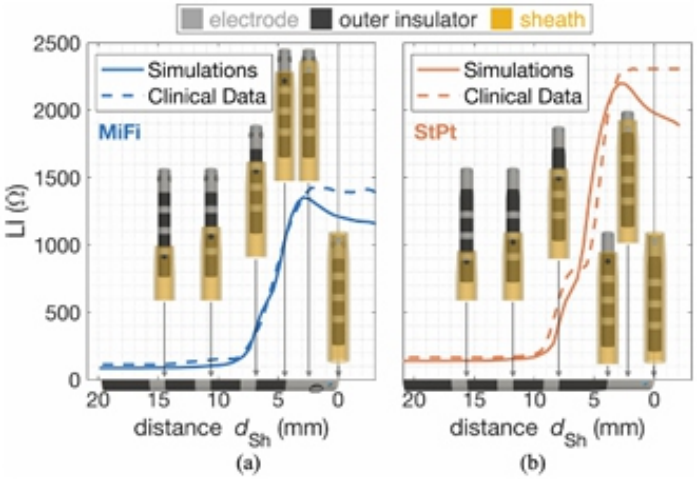

Fig. 4. Withdrawal of (a) IntellaNav MiFi OI and (b) IntellaNav Stablepoint into a transseptal sheath. *In silico* LI is represented by solid lines while clinical LI is represented by dashed lines. Sheath positions are indicated on the horizontal axes.

Section II-D. With the in silico and in vitro traces matching both in morphology and absolute values, the simulation environment was considered valid to a high degree of detail across the relevant range of conductivities for further experiments. NaCl concentrations of NaCl =0.06 mol l and NaCl =0.07 mol l equaling mass concentrations of 0.35 % and 0.41 % were found to yield an LI comparable to human blood .For a concentration of NaCl =0.06 mol l ,thein silico setups yielded an LI of 98.3 Ω and 154.5 Ω compared to in vitro measurements at 21 ◦C of 101.9 Ω and 156.2 Ω for the IntellaNav MiFi OI and IntellaNav Stablepoint, respectively, which compared well to the clinically observed ranges of bloodpool LI. The simulated bloodpool LI for a blood conductivity σ = 0.7 S m [22] as given in Table I and later on used in all other in silico setups was at the lower bound of clinically observed values with 87.1 Ω for the IntellaNav MiFi OI and 138.9 Ω for the IntellaNav Stablepoint. Linear regression of LI measurements with both catheters deduced a perfect linear relationship (R2 < 10−4) between LI values measured with the IntellaNav MiFi OI (LIMiFi) and the IntellaNav Stable point (LIStPt)forin silico and in vitro experiments. Measurements inanextendedsetof25NaClsolutionsof concentrations between0.15%and2.00%yielded the following linear relationship:

$$LI_{\mathrm{StPt}} = 1.42 \cdot LI_{\mathrm{MiFi}} + 8.7\,\Omega \qquad (1)$$

B. Transseptal Steerable Sheath

Fig. 4 presents simulated and exemplary clinical LI traces characteristic for the withdrawal of the IntellaNav MiFi OI (a) and the IntellaNav Stablepoint (b) into the transseptal sheath. Starting at a simulated bloodpool of 87 Ω and 139 Ω, the in silico LI measured with the IntellaNav MiFi OI and the IntellaNav Stablepoint first increased by more than 2 Ω for the distal edge of the sheath being located

between the proximal and the 2nd to proximal ring electrode. The steep

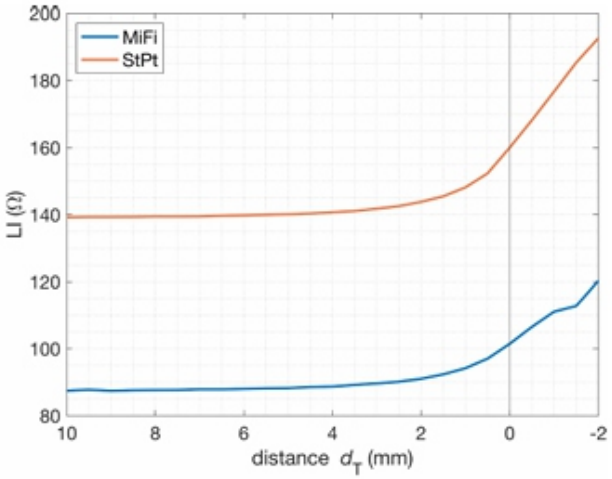

Fig. 5. Dependency of LI on the distance to myocardial tissue for IntellaNav MiFi OI in blue and IntellaNav Stablepoint in orange.

increase of LI began upon the coverage of the distal ring electrode by the sheath. For full sheath coverage, the LI increased up to 1353 Ω and 2200 Ω for the IntellaNav MiFi OI and the IntellaNav Stablepoint, respectively. For the distal edge of the sheath being located between the distal ring electrode and the tip electrode, an interim decrease in steepness formed a plateau especially pronounced for the IntellaNav Stablepoint.

Both simulated traces compared well with the clinically measured traces.

C. Catheter Tissue Interaction

1) Catheter Distance and Orientation: Again starting from a bloodpool LI of 87 Ω and 139 Ω for the IntellaNav MiFi OI and the IntellaNav Stablepoint, respectively, the LI increased with decreasing distance to the tissue surface for perpendicular catheter positions ($\alpha T = 90^\circ$) as shown in Fig. 5. At a distance dT =3.5mm and dT =2.5mm, the LI exceeded the bloodpool LI by more than 2 % for the IntellaNav MiFi OI and IntellaNav Stablepoint, respectively. At a distancedT =0mm,theLIexceededthebloodpoolLIby16.0% and 14.9 % for the IntellaNav MiFi OI and IntellaNav Stablepoint, respectively. The closer the catheter approached the tissue, the steeper the LI increased. For negative distances dT, i.e. the catheter entering the tissue, the increase in LI per distance was approximately constant. For the IntellaNav MiFi OI, a small plateau in LI formed between dT = −1.0mm and dT = −1.5mm.

Fig. 6 presents the simulated LI values for changing angles αT between the catheter and the tissue for selected distances. For both catheters and all distances, the traces were w-shaped. Starting from a perpendicular position and approaching a parallel position, LI first dropped and then increased again.TheLIfor parallel catheter orientation at a distance dT =0mm exceeded the LI for perpendicular

catheter positions by 14.0 Ω (αT =0◦) and12.9Ω(αT = 180◦)fortheIntellaNavMiFiOIandby9.4Ω

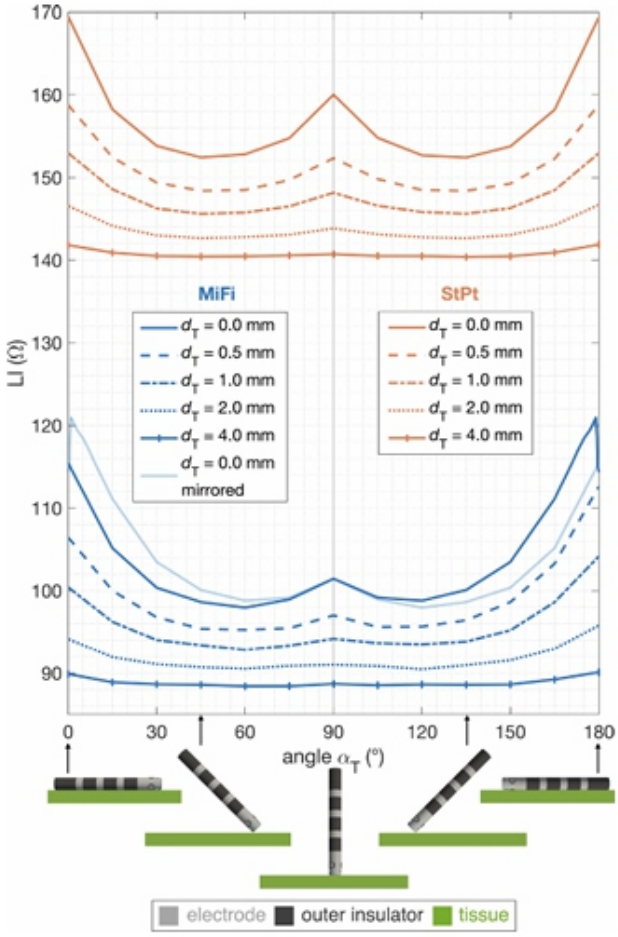

Fig. 6. Dependency of LI on the angle α_T between catheter and myocardial tissue for IntellaNav MiFi OI in blue and IntellaNav Stablepoint in orange for different distances d_T between catheter and tissue.

for the IntellaNav Stablepoint. While the traces were symmetric to αT =90◦ for the IntellaNav Stablepoint, the LI depended on the orientation of the mini electrodes for the IntellaNav MiFi OI as indicated by the mirroredtrace in Fig. 6. Catheter orientations with one of the measuring mini electrodes being directed to the tissue ((90◦ <αT ≤ 180◦)) exceeded those LI values of the same distance and angle for which none of the mini electrodes pointed directly towards the tissue (0◦ ≤ αT < 90◦).

In vitro measurements with the respective catheter touching a tissue phantom or a tissue sample perpendicularly and in parallel yielded comparable differences between the paralle land orthogonal position. The LI for the parallel position exceeded the LI of the perpendicular position by approximately 11 Ω and 10 Ω for the IntellaNav MiFi OI and IntellaNav Stablepoint, respectively.

2) Transmural Lesion: Due to the higher conductivity of connective tissue compared to healthy myocardium, the LI typically drops in the vicinity of myocardial lesions. In these setups, the dependency of the LI onthe extent of the scar and the relative position of the catheter was investigated. Fig. 7 shows LI

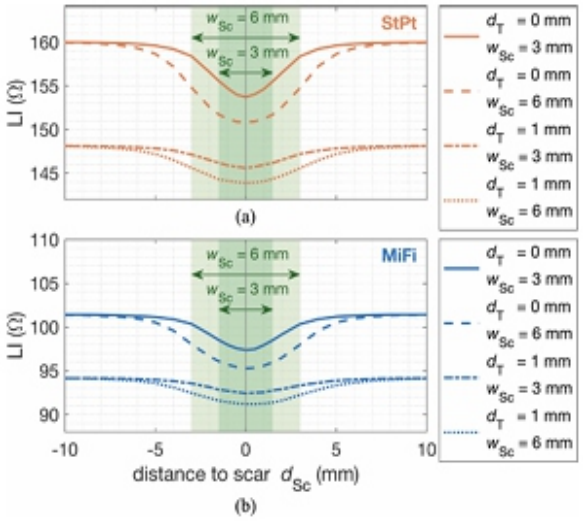

Fig. 7. Dependency of the LI on the horizontal distance d_{Sc} to a linear scar embedded in a patch of tissue for the IntellaNav MiFi OI in (a) and the IntellaNav Stablepoint in (b). Each catheter hovered the tissue at two vertical distances $d_T = 0$ mm and $d_T = 1$ mm for two different scar widths $w_{Sc} = 3$ mm and $w_{Sc} = 6$ mm.

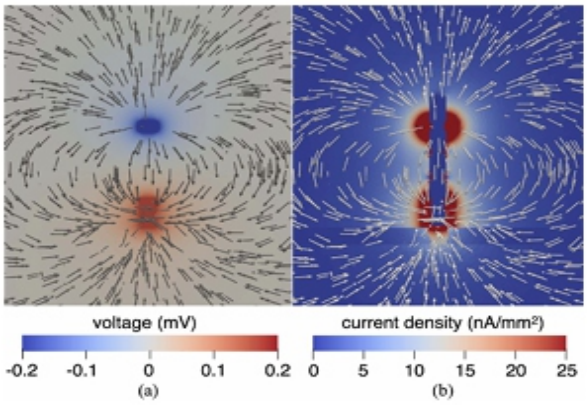

Fig. 8. Cross section of a setup with a scar of 3 mm width embedded in a patch of myocardial tissue surrounded by blood. The (a) potential field and (b) current density characterize the electrical field. Arrows mark the direction of current flow.

traces for the virtual catheter passing linear lesions of 3 mm and 6mmwidth.Fordirecttissue contact (dT = 0mm),theabsolute drop was larger for the IntellaNav Stablepoint due to the higher baseline LI for either lesion width .The percentage drop base don the LI at maximum distance to the lesion, however, was similar with3.8%and6.0% for lesion width so f3 mmand 6mm for the IntellaNav MiFi OI and a percentage drop of 3.9 % and 5.7 % for the IntellaNav Stablepoint. Increasing the vertical distance dT between the catheter and the myocardial tissue by 1 mm caused a larger drop in the baseline LI than either of the scars for both catheters.

Fig. 8 shows the potential field (a) and the current density (b) for the setup with a scar width wSc = 3mm and direct tissue contact. With a similarity to an electrical dipole field, the current spreads between the injecting electrodes. The current density in

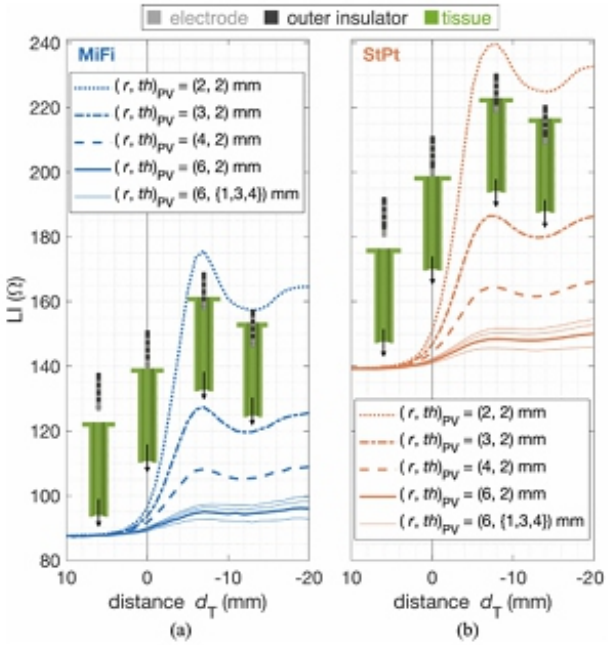

Fig. 9. LI traces upon progressive introduction of (a) IntellaNav MiFi OI in blue and (b) IntellaNav Stablepoint in orange into a PV. The horizontal axis annotates the distance between the tip of the ablation catheter and the edge of the tissue. Negative distances correspond to positions inside the PV.

Fig. 8(b) adumbrates the edges of the tissue directly underneath the distal tip electrode. Higher current densities in the central line of scar compared to the surrounding tissue were caused by the higher conductivity of scar tissue.

D. Insertion Into a Pulmonary Vein

Fig. 9 shows characteristic LI traces for progressive introduction of an ablation catheter into the PV. Fig. 9(a) displays simulated LI values for the IntellaNav MiFi OI . The LI increased from 87Ωinthe simulated blood pool up to peak values between 93Ω and 176 Ω depending on the radius rPV and the thickness thPV of the PV.According LI traces for the IntellaNav Stablepoint are presented in Fig. 9(b). Starting from a simulated bloodpool LI of 139 Ω, the LI increased up to 145 Ω to 240 Ω depending on rPV and thPV.

The radius rPV was found to be a strong determinant of the maximum LI reached upon insertion of the catheter into the PV. While the narrowest simulated PV with rPV =2mm yielded a maximum LI of 176 Ω with the IntellaNav MiFi OI and 240 Ω with the IntellaNav Stablepoint, an increase of the radius by 1 mm resulted in a maximum LI of only 127 Ω and 186 Ω, respectively.

Peak values for all parameterizations of the PV corresponded with the insertion of the tip of the ablation catheter into the PV in the in silico experiments. The slight decrease for deeper insertions was related to the passing of the surrounding tissue plate that additionally elevated the LI at its maximum. The thickness of the vein tissue took additional influence on the absolute LI value, as shown for a vein

radius rPV =6mm in Fig. 9.

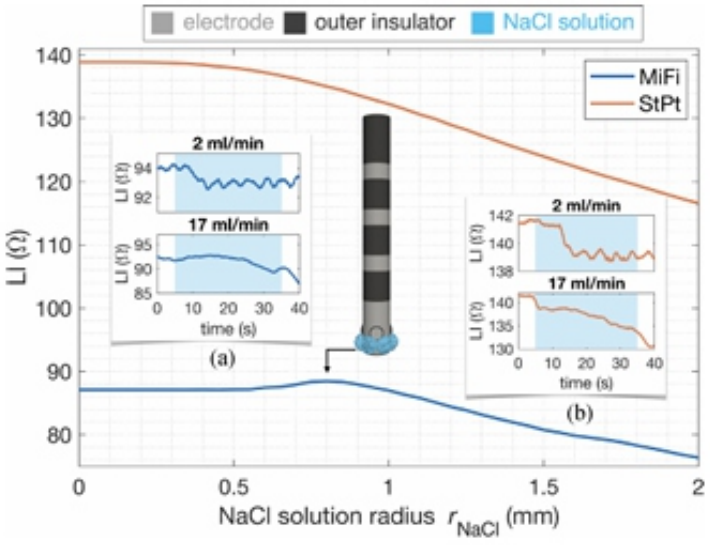

Fig. 10. *In silico* LI for different irrigation radii of NaCl solution for the IntellaNav MiFi OI in blue and the IntellaNav Stablepoint in orange. Subpanels (a) and (b) report *in vitro* measurements for the onset of irrigation flow rates of 2 $\frac{ml}{min}$ and 17 $\frac{ml}{min}$. Irrigation times are shaded in blue.

E. NaCl Solution Irrigation

Fig. 10 displays simulated LI values for flushing of the catheters with physiological NaCl solution exiting the cooling lumen at the irrigation holes. Varying the bubble radius rNaCl from 0 to 2 mm mimicked changing the irrigation flow rate. The LI remained indifferent to NaCl bubbles up to a radius rNaCl =0.7mmandrNaCl =0.55mmwithlessthan1%change compared to the in silico measurement in plain bloodpool of 87Ω and 139Ω for the IntellaNav MiFi OI and the the IntellaNav Stablepoint, respectively. For the IntellaNav MiFi OI, the LI then slightly increased reaching a maximum elevation of 1.4 Ω above the bloodpool for rNaCl =0.8 mm when the NaCl bubbles barely reached the mini electrodes' distal edges. Afterwards, LI values decreased with increasing rNaCl down to 76.4 Ω for rNaCl =2mm. The LI decreased monotonously for the IntellaNav Stablepoint down to 116.6Ω rNaCl =2mm.

Fig. 10(a) and (b) display in vitro traces of LI for onset and offset of irrigation at different flow rates. In vitro measurements at a flow rate of 2 ml min revealed an instantaneous drop of 0.6 Ω and 1 Ω and oscillations in LI of 0.6 Ω and 1 Ω peak-to-peak amplitude tracing back to the cylinders of the irrigation wheel compressing the irrigation tube for the IntellaNav MiFi OI and the IntellaNav Stablepoint, respectively. For the IntellaNav Stablepoint, LI dropped abruptly by 2.5 Ω upon the onset of irrigation at 17 ml min. The gradual decrease of LI is the result of a small bath volume mixing with the irrigation fluid of higher conductivity

IV. DISCUSSION

In summary, we presented an in silico environment that resembled in human and invitroLI measurements to a high degree of detail and allowed for quantification of distinct influences on the measurement with known ground truth.

A. Aqueous NaCl Solutions

Model validation with standardized aqueous NaCl solutions of knownconductivity was successful and proved the suitability of the simulation environment. NaCl solutions can be assumed to be of mostly resistive character at a measurement frequency of 14.5 kHz. Thus, the hyperbolic-like relationship between conductivity and LI can be explained as impedance reduces to resistance in this setup and resistance is reciprocally related to conductivity.

For in vitro experiments, aqueous NaCl solutions at 0.35 % to 0.4 % mass concentration at 21 ◦C were shown to serve well as dielectric equivalent of human blood at body temperature for a measurement frequency of 14.5 kHz.

A perfectly linear relationship between LI measurements with the IntellaNav MiFi OI and the IntellaNav Stablepoint as described by equation (1) is of great clinical value. Translation of findings and reference values between both catheters can extrapolate clinical trials to the respective other device and reduce efforts. Measurements with different instances of the catheters resulted in minor deviations of the linear coefficients and could potentially be caused by slight manufacturing differences or by the fact that all in vitro catheters had been used for radio frequency ablation before.

B. Transseptal Steerable Sheath

In silico experiments revealed that LI started to increase no tably as soon as the sheath passed the proximal ring electrode. LI measurements for both, substrate and lesion characterization in clinical practice, should therefore always assure full withdrawal of the catheter out of the sheath in order to prevent confounding influences on the measured LI.

C. Catheter Tissue Interaction

The elevation of LI in tissue contact above the bloodpool LI ranged from 14Ω for 0 mm distance to the tissue, i.e. 0 g so-called “contact force,” to 33 Ω for −2 mm distance to the tissue and compared well to clinically observed mean ranges between 16Ω and 20Ω [27] for the IntellaNav MiFi OI. The simulated upper bound for an immersion depth of 2 mm thus likely overestimates the LI for clinical mean contact force applications due to the disregard of realistic tissue deformation. Sulkin et al. had performed detailed in vitro experiments on catheter tissue interaction with the IntellaNav MiFi OI and found a nonlinear monotonic increase of LI as the catheter approximated the tissue at an angle of 90◦ [7]. The in

silico results generated in this work matched the shape of the curve very well but yielded scaled absolute values and slopes presumably due to differences in the underlying conductivity of tissue and blood. The right ventricular tissue used by Sulkin et al. was presumably thicker than the atrial tissue modeled with a thickness of only 2.5 mm in this work and could explain the higher absolute values and slopes in their study. Additionally, the natural variability of the conductivity of tissue samples causes a spread of measured LIs [7] that could account for the scaled results. The specific conductivities chosen in this work are only one sample of the natural spread of human myocardial conductivity.

Changing the angle between catheter and tissue resulted in higher LIs for more parallel compared to orthogonal catheter orientation for distances $dT > -2$mmbothintheworkbySulkin et al. and the in silico experiments in this work. Garrott et al. [8] observed a mean LI difference of 13 Ω between perpendicular and parallel catheter orientation of the IntellaNav StPt which is well in line with the in silico experiments here.

In silico experiments with the IntellaNav MiFi OI presented a small plateau for an immersion into atrial tissue by 1.0 mm to 1.5 mm as well as an abrupt decrease in LI for an angle $\alpha T = 180^{\circ}$ that were not in line with the trend of the respective adjacent distances and angles. Presumably, the between the measuring mini electrode and the tissue caused both observations.

Clinical studies report different ranges of LI values for healthy and scar tissue, e.g. 109Ω ± 15Ω and 104Ω ±12Ω [10], 111Ω ±14Ω and 92Ω±16Ω [11], and 132Ω±12Ω [12], respectively, for the IntellaNav MiFi OI. The variability in range may be explained by different operators and differences in typically applied contact force which remains uncontrolled for the IntellaNav MiFi OI. In line with previously published clinical observations, scar tissue presented lower LI compared to healthy myocardium duetotheincrease in extracellular space and the resulting increase in conductivity in the in silico model as well. Slightly lower values for both healthy and scar tissue in the in silico study as depicted in Fig. 7 in comparison with the clinical observations [10]–[12] could either be caused by the choice of conductivies in the in silico model or from a lower contact force. While the in silico model operates at an equivalent of 0 g so-called “contact force” for the experiments on scar tissue, typical clinical values range from 5 g to 20 g. The larger the lesion area within the footprint of the catheter, the lower the LI dropped. The results presented in Fig. 7 emphasize the importance of direct tissue contact and controlled contact force for quantitative applications of LI measurements. Drops in baseline LI caused by only 1 mm distance to the endocardial surface exceeded LI drops caused by transmural lesions. Since the exact values depend on the scar and tissue conductivity provided to the model and scar conductivity was approximated by the conductivity of connective tissue, a validation of the conductivity of atrial scar tissue would strengthen the finding but was out of the scope of this work.

Myocardial tissue was modeled as homogeneous, isotropic block. The effect of fiber direction and three-dimensional atrial structures remains unlit within the scope of this work. Future studies will have

to shed light on more detailed models of the myocardium.

D. Insertion Into a Pulmonary Vein

In silico experiments demonstrated the strong dependency of the LI measured inside a PV on the radius of the vein. Vein tissue was modeled indifferently from myocardial tissue for simplicity although the substrates clearly differ histologically and can be assumed to further alter the LI measured in human Pvs.

E. NaCl Solution Irrigation

Both IntellaNav MiFi OI and IntellaNav Stablepoint come with an open irrigated tip with the purpose of cooling the electrode during ablation delivery. Typically, catheters are flushed with 0.9 % so-called physiological NaCl solution at lab temperature. However, 0.9 % NaCl solution deviates by a factor of approximately 2 from human blood in terms of conductivity (compare Table I). Earlier studies have shown that the irrigation fluid during radio frequency ablation delivery takes influence on lesion formation. Highly conductive irrigation fluids such as physiological NaCl solution attract current flow and thus reduce the current flowing through the target tissue resulting in reduced energy deposition and smaller lesions compared to irrigation with less conductive fluids such as 0.45 % NaCl solution or dextrose water [28]–[31]. Similarly, awareness should be drawn to irrigation fluids for LI measurements during ablation delivery and substrate characterization. In particular, two cases have to be distinguished: the effect of constant irrigation flow rates >0 ml /min and the effect of changing flow rates .Constant flow rates mainly relate to the application of LI substrate mapping while a change of flow rate alludes to the use case of radio frequency ablation delivery. In either case, clinical LI is mostly interpreted in differential manner comparing to the bloodpool reference or the LI at the start of the ablation as opposed to absolute values. With the typical increase of the irrigation flow rate from a default flow of 2 ml min to 17 ml min or 30 ml min during radio frequency power delivery, the amount of irrigation fluid surrounding the catheter tip presumably increases and causes an LI drop by default that is not related to tissue heating as commonly attributed to LI drops during ablation.

With the results presented in Fig. 10 and the assumption that the irrigation fluid is quickly flushed by circulatory blood flow, the LI drop caused by changes of the irrigation flow rate seem to be mostly negligible seen in the context of typically required minimum LI drops of 12 Ω to 16 Ω during radio frequency power delivery with the IntellaNav MiFi OI [9]. For the use case of LI substrate mapping, LI differences of few ohms become of importance. However , a constantly low flow rate of 2 ml /min limits the potential for flawing the measurement. Interpreting LI only in differential manner, irrigation will impact the result if the distribution of NaCl close to the catheter tip changes, e.g. due to blood flow.

Additionally, the higher conductivity of NaCl solution compared to tissue and blood less current to flow through the target of interest. The in silico investigations in this work are clearly limited to the oversimplified spherical geometries of NaCl irrigation f luid at the catheter tip as well as the lack of a clear correlation betweensphericalradiusinthemodelandclinicalirrigationflow rates. Similarly, the in vitro setup lacks a model of circulatory blood flow. Including a fluid dynamics model could bring more detailed insights into the influence of irrigation and irrigation changes on the measured LI.

F. Sensitivity

Slight variations in the catheter dimensions resulted in not able changes of LI especially for the respective measuring electrodes.

For quantitative analyses, a detailed geometrical model of the catheter under investigation is therefore of high importance.

In silico experiments in this work demonstrated that selected phenomena of interest such as the presence of scar tissue result in minute changes in LI while recording conditions such as the loss of optimal wall contact cause changes in the same or even higher order of magnitude .In a clinical environment under the presence of measurement noise ,the detectable range of changes in LI will further decrease, which emphasizes the necessity of establishing ideal wall contact, amongst other recording conditions under control of the operator.

In clinical setups, the inflation and deflation of the lungs is an additional confounding factor with evident impact on the LI measurement [27] due to the close proximity of the lungs to selected parts of the cardiac chambers. While the conductivity of inflated lungs is reported to be 0.0954 S m at 14.5 kHz, the conductivityincreasesto0.247 S m indeflatedstate[21].Sincethe respiratory state of the patient is a known parameter, respiratory oscillations in LI traces could be compensated for.

An estimate of the relative contribution of sample volumes in vicinity to the catheter to the measured LI would be of high interest in order to assess the suitability of catheters and electrode arrangements for impedance measurements. The close proximity of the catheter will take significantly more influence on the measured impedance for LI measurements as compared to generator impedance measurements. Specific examples such as varying the distance between catheter and tissue, scar, and sheath as well as varying the volume of NaCl irrigation fluid were presented in this work. However, a systematic analysis does not only require the variation of the sample volume position but also of its size and conductivity. Future studies should systematically shed light on this aspect in order to further optimize catheter electrode arrangement for LI measurements.

V. CONCLUSION

With this work,we introduced and validated an in silico model including highly detailed catheter and sheath geometries in combination with a simplified myocardial geometry to study local electrical impedance measurements with intra-atrial catheters. Clinically relevant scenarios such as catheter-tissue interaction in terms of angle, distance, and substrate, the insertion of the catheter into a PV, the withdrawal into the trans septal sheath, and catheter irrigation were reflected in the model. Forward simulations of the electrical field gave in sights in the quantitative effects of isolated and combined changes in parameters on the LI. The presented environment proved to be a highly valuable tool that provides deeper in sight in to the clinical inter pretation of LI and has the potential to support future catheter development.

ACKNOWLEDGMENT

The authors would like to thank Tobias Oesterlein (Boston Scientific, Ratingen, Germany),CarinaJäger(BostonScientific, Ratingen, Germany) and the always receptive EP nursing team at Städtisches Klinikum Karlsruhe for their support.

REFERENCES

[1] S. Gabriel, R. W. Lau, and C. Gabriel, "The dielectric properties of biological tissues: II. Measurements in the frequency range 10 Hz to 20 Ghz," Phys. Med. Biol., vol. 41,, Apr. 1996, Art. no. 2251.

[2] S.Grimnes and O.G. Martinsen, Bioimpe dance and Bioelectricity Basics, San London Diego: Academic Press, 2000.

[3] C.Reithmannetal.,"Different patterns of the fall of impedance as the result of heating during ostial pulmonary vein ablation: Implications for power titration," Pacing Clin. Electro physiol., vol. 28, pp. 1282–1291, Jan. 2005.

[4] G. S. Chuet al., "Local impedance for the optimization of radiofrequency lesion delivery: A review of bench and clinical data," J. Cardiovasc. Electrophysiol., vol. 33, pp. 389–400, Dec. 2021.

[5] P. C. Qian et al., "Optimizing impedance change measurement during radiofrequency ablation enables more accurate characterization of lesion formation," JACC: Clin. Electrophysiol., vol. 7, pp. 471–481, Apr. 2021.

[6] R. van Es et al., "Novel method for electrode-tissue contact measure ment with multi-electrode catheters," EP Europace, vol. 20, pp. 149–156, Jan. 2017.

[7] M. S. Sulkin et al., "Novel measure of local impedance predicts catheter tissue contact and lesion formation,"Circulation.ArrhythmiaElectrophys iol., vol. 11, Apr. 2018, Art. no. e005831.

[8] K. Garrott et al., "Combined local impedance and contact force for radio frequency ablation

assessment,"HeartRhythm,vol.17,pp. 1371–1380, Aug. 2020.

[9] M. Das et al., "Local catheter impedance drop during pulmonary vein isolation predicts acute conduction block in patients with paroxys malatrial f ibrillation: Initial results of the LOCALIZE clinical trial," EP Europace, vol. 23, pp. 1042–1051, Feb. 2021.

[10] L. Segreti et al., "A novel local impedance algorithm to guide effective pulmonary vein isolation in atrial fibrillation patients: Preliminary experience across different ablation sites from the CHARISMA pilot study," J. Cardiovasc. Electrophysiol., vol. 31, pp. 2319–2327, Jul. 2020.

[11] M. Gunawardene et al., "A novel assessment of local impedance during catheter ablation: Initial experience in humans comparing local and generator measurements," EP Europace, vol. 21, pp. i34–i42, Jan. 2019.

[12] C. A. Martin et al., "First clinical use of novel ablation catheter incorporating local impedance data," J. Cardiovasc. Electrophysiol., vol. 29, pp. 1197–1206, Sep. 2018.

[13] P. Kauppinen, J. Hyttinen, and J. Malmivuo, "Sensitivity distribution visualizations of impedance tomography measurement strategies," Int. J. Bio electro magnetism, vol. 8, pp. 63–71, Jan. 2006.

[14] INTELLANAV MIFI OPEN-IRRIGATED ABLATION CATHETER, Boston Scientific Corporation. 2018. Accessed: May 01, 2022. [Online]. Available: https://www.bostonscientific.com/content/dam/bostonscientific/Rhythm%20Management/general/EP-479201-AB_IntellaNav%20MiFi%20OI%20Spec%20Sheet%20FINAL.pdf

[15] INTELLANAV STABLEPOINT ABLATION CATHETER, Boston Scientific Corporation. 2020. Accessed: May 01, 2022. [Online]. Available: https://www.bostonscientific.com/content/dam/bostonscientific/ep/Electrophysiology%20Portfolio/Rhythmia/intellanav-stablepoint/EP 815001-AB_STABLEPOINT_SPECSHEET.pdf

[16] C. Geuzaine and J.-F. Remacle, "GMSH: A three-dimensional finite element meshgenerator with built-in pre- and post-processing facilities," Int. J. Numer. Methods Eng., vol. 79, no. 11, pp. 1309–1331, 2009.

[17] P. G. Platonov et al., "Left atrial posterior wall thickness in patients with and without atrial fibrillation: Data from 298 consecutive autopsies," J. Cardiovasc. Electrophysiol., vol. 19, pp. 689–692, Feb. 2008.

[18] D. R. Lide and T. J. Bruno, CRC Handbook of Chemistry and Physics, vol. 99. Boca Raton, FL, USA: CRC Press, 2018.

[19] The effect of temperature on conductivity measurement; CONDUCTIVITY METER 4520 application note: A002-001 A. Accessed: Dec. 01, 2022. [Online]. Available: http://www.jenway.com/adminimages/A02_001A_Effect_of_temperature_on_conductivity.pdf

[20] H. Cao, M. A. Speidel, Jang-Zern Tsai, M. S. Van Lysel, V. R. Vorperian, and J. G. Webster, "FEM

analysis of predicting electrode-myocardium contact from RF cardiac catheter ablation system impedance,"IEEETrans. Biomed. Eng., vol. 49, no. 6, pp. 520–526, Jun. 2002.

[21] IT'IS Foundation, "Tissue properties database v4.0," May 2018.

[22] C. Gabriel, Compilation of the Dielectric Properties of Body Tissues at RF and Microwave Frequencies. Texas, USA: Occupational and Environmental Health Directorate, Radiofrequency Radiation Division, Brooks Air Force Base, Jan. 1996. Report N.AL/OE-TR-1996-0037.

[23] A. Adler and W. R. B. Lionheart, "Uses and abuses of EIDORS: An extensible software base for EIT," Physiol. Meas., vol. 27, pp. S25–42, May 2006.

[24] K.-S.Chengetal.,"Electrode models for electric current computed tomography," IEEE Trans. Biomed. Eng., vol. 36, no. 9, pp. 918–924, Sep. 1989.

[25] D. Bennett, "NaCl doping and the conductivity of agar phantoms," Mater. Sci. Eng.: C, vol. 31, pp. 494–498, Aug. 2011.

[26] M.A. Kandadai, J.L. Raymond, and G.J.Shaw,"Comparison of electrical conductivities of various brain phantom gels: Developing a 'brain gel model'," Mater. Sci. Engineering: C, vol. 32, pp. 2664–2667, Dec. 2012.

[27] L. A. Ungeret al., "Local electrical impedance mapping of the atria: Conclusions on substrate properties and confounding factors," Front. Physiol., vol. 12, Jan. 2022, Art. no. 788885.

[28] C. Gianni et al., "Half-normal saline versus normal saline for irrigation of open-irrigated radiofrequency catheters in atrial fibrillation ablation," J. Cardiovasc. Electrophysiol., vol. 32, pp. 973–981, Jan. 2021.

[29] D. T. Nguyen et al., "Effect of irrigant characteristics on lesion formation after radiofrequency energy delivery using ablation catheters with actively cooled tips," J. Cardiovasc. Electrophysiol., vol. 26, pp. 792–798, Jul. 2015.

[30] D. T. Nguyen et al., "Effect of environmental impedance surrounding a radiofrequency ablation catheter electrode on lesion characteristics," J. Cardiovasc. Electrophysiol., vol. 28, pp. 564–569, Feb. 2017.

[31] D. T. Nguyen et al., "Radiofrequency ablation using an open irrigated electrode cooled with half-normal saline," JACC: Clin. Electrophysiol., vol. 3, pp. 1103–1110, Oct. 2017

ISSN : 2582-7405

Smart Artificial Soft Tissue- Application to a Hybrid Simulator for Training of Laryngeal Pacemaker Implantation

Thomas Thurner , Benjamin Esterer , David Fürst, Marianne Hollensteiner , Member, IEEE, Sabrina Sandriesser, Peter Augat, Roland Pruckner, Daniela Wirthl, Martin Kaltenbrunner, Andreas Müller, Gerhard Förster, Claus Pototschnig, and Andreas Schrempf

ABSTRACT

Surgical simulators are safe and evolving educational tools for developing surgical skills. In virtual and hybrid simulators are preferred due to their detailedness, customization and evaluation capabilities. To accelerate the revolution of a novel class of hybrid simulators, a Smart Artificial Soft Tissue is presented here, that determines the relative position of conductive surgical instruments in artificial soft tissue by inverse resistance mappings without the need for a fixed reference point. This is particularly beneficial for highly deformable structures when specific target regions need to be reached or avoided. The carbon-black-silicone composite used can be shaped almost arbitrarily and its elasticity can be tuned by modifying the silicone base material. Thus, objective positional feedback for haptically correct artificial soft tissue can ensured. This is demonstrated by the development of a laryngeal phantom to simulate the implantation of laryngeal pacemaker electrodes. Apart from the position-detecting larynx phantom, the simulator uses a tablet computer for the virtual representation of the vocal folds' movements, in accordance with the electrical stimulation by the inserted electrodes. The possibility of displaying additional information about target regions and anatomy is intended to optimize the learning progress and illustrates the extensibility of hybrid surgical simulators.

Index Terms—Artificial tissue, hybrid medical simulation, laryngeal pacemaker, electrode positioning, haptical realistic, soft sensor, position detection.

I. INTRODUCTION

SURGICAL simulation has proven to be an essential train ing method to significantly improve skills, especially of young physicians, or when practicing innovative new surgical approaches without risk to patients [1], [2]. As a result of constantly advancing research, various types of simulators have been developed that can simulate increasingly complex processes [3]. A rough distinction can be made between four categories: simulation using animal trials, experiments on human cadavers, simulations with synthetic replicas of anatomies, and electronically enhanced or visual replicas [4]. The latter category also includes virtual reality (VR)-based simulators and hybrid simulators that combine different technologies to optimize training. Many new simulators belong to the latter group [1], [5],

[6], [7], [8], [9].

Despite all advantages of purely visual simulators, haptic components often remain indispensable [5]. In particular, instrument handling and the haptic perception of different tissue layers during cutting or penetration represents a critical core competence. The aim of a hybrid simulator is therefore to seamlessly combine animations and evaluations of virtual simulators [6], [10] including their level of detail, with realistic haptic components of passive simulators [11], [12], [13]. Also, the chance of using real surgical instruments with all their capabilities should be taken. Such a combination of different systems can deliver good results in terms of learning success, as already shown in first publications [7], [8], [14], [15].

Typically optical or electromagnetic systems are used for instrument tracking. In optical tracking systems, visual markers are placed on the instruments and the patient phantom.

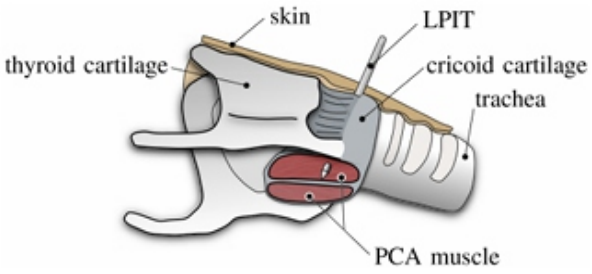

Fig. 1. Anatomy of the larynx showing PCA muscle and LPIT.

Their positions are captured by cameras and the position and orientation of the instrument relative to the camera system is determined [16], [17]. This position data can be embedded in virtual animations. Especially when interacting with artificial soft tissue, representing muscles or connective tissue, optical systems fail to provide accurate results, since in most cases the markers cannot be placed directly on or inside the deformable phantom parts. Electromagnetic tracking systems, on the other hand, obtain the position and orientation of small target coils within a generated magnetic field [18], where these small coils can be directly applied to the deformable artificial tissue. However, the coils are expensive, alter the haptics of soft tissue and require a cable connection between each coil and the tracking system, which limits their usage in hybrid simulators. In addition, this technique brings limitations to the use of metals in the detection area, as they affect the electromagnetic field and thus the tracking accuracy.

This work describes a cost-effective alternative to complex tracking systems, the development of "Smart Artificial Soft Tissue," tissue-mimicking patient phantom parts which provide realistic haptic feedback and integrated sensing capabilities. The objective is to develop an intelligent artificial human larynx that focuses on the cricoid region and posterior cricoarytenoid muscles to provide a realistic training environment for the most critical part during the implantation of a laryngeal pacemaker (LP) system (MED-EL Elektromedizinische Geräte Gesellschaft m.b.H., Innsbruck, Austria).

Apart from preclinical evaluation of the LPsystem[19],functional testing is also usually performed on animals to evaluate the evoked responses to electrical stimulation. Not only ethical concerns might arise from animal testing but also high costs might be associated. Considering the 3R principle for replacement, refinement and reduction in preclinical testing, using a simulator for training purposes is even more preferable.

Such a surgical simulator needs to meet specific requirements to be a real alternative. Haptic perception when advancing an LP Insertion Tool (LPIT) through different soft tissue layers such as skin, mucosa, cartilage and muscle tissue is a key skill to learn (Fig. 1). The correct positioning of the electrode into the posterior cricoarytenoid (PCA) muscle ultimately determines whether the vocal fold can be opened correctly by neuromuscular stimulation. For this purpose, it is essential to determine instrument position on deformable phantom parts. The hybrid simulator to be presented aims to include an artificial larynx with different, haptically realistic tissue layers and an artificial PCA muscle realized as Smart Artificial Soft Tissue. To achieve the key learning objectives, the focus will be on the fusion of position recognition and haptic realism in a hybrid environment.

II. MATERIALAND METHODS

A. Laryngeal Pacemaker and Electrode Implantation

The LP System [20] was developed by MED-EL to treat patients with bilateral vocal fold paralysis and is based on the concept of selective neurostimulation of terminal abductor branches of the recurrent laryngeal nerve (RLN) [21]. The LP-System requires to find a sensitive area, a so-called hotspot, on the PCA muscle in order to control the opening of the vocal fold. During implantation ,hot spot identification and electrode fixation are the most critical steps and hence are thought to be most beneficial to train in a hybrid simulator. To target the hotspot, the LPIT is used to allow a minimally invasive electrode placement into the PCA. The LPIT is a bipolar electrode consisting of a trocar and a canula. After a small horizontal skin incision over the cricoid, the LPIT is advanced across the upper border of the cricoid arch and pushed sub mucosally along the inner surface of the arch towards the cricoid lamina. Penetrating the lamina requires advancing the LPIT gradually and gently, applying slight rotary movements, until the PCA muscle is reached and a hotspot hopefully found (Fig. 1). For verification, electrical stimulation is used under video lary goscopic monitoring of the vocal fold movements[20]. If necessary, the LPIT position can be changed by retracting it from the lamina, repositioning it, and advancing it again until the hotspot (with the best abduction of the vocal fold) is found in the PCA.

B. Haptically Realistic Artificial Tissue

1) Tissue Development: The challenge of developing an artificial larynx with a cricoid cartilage lies in the interaction of materials of different hardness and toughness. Therefore, the haptically realistic design has only been created for those structures that are actually relevant during surgical simulation or need to be penetrated by the LPIT. Here, these are the outer skin, the cartilage itself and the tissue directly surrounding it.

The development of the artificial cricoid was based on expert opinions and material tests. First, the outer shell of the cricoid cartilage was 3D printed using Ultimaker TPU95 A (Ultimaker B.V.,Utrecht, The Netherlands) filament.The print had a general wall thickness of 1mmanda layer height of 0.1mm without any filling. Only the wall thickness on the side facing the injection site was reduced to 0.3mm by decreasing the number of 3Dprinted layers. In addition, the same side was covered with athin layer (0.2mm)ofsuperglue(LoctiteSuperGlueLiquid,Henkel AG & Co. KGaA, Düsseldorf, Germany) to generate a small, sharp first insertion force peak. This empty shell was filled with an urethane rubber (PMC780fromSmooth-On,Inc.,Macungie, PA, USA)mixedwithsilicone oil (AP100 fromWacker Chemie AG, München, Germany) at a ratio of 30:9 by weight to reduce the friction of the LPIT while sliding through the urethane rubber. To ensure a better connection between soft tissue and

Fig. 2. Cricoid cartilage and surrounding tissue - real cricoid of a human versus artificial, simplified replica; (a) measuring forces while penetrating cricoid cartilage, (b) rendering of an artificial, simplified cricoid cartilage (white) with soft tissue (pink) and sensor mat ("Smart Artificial Soft Tissue," black) underneath (soft tissue partially removed to reveal cartilage).

cartilage, polyester wadding was glued to the inner surface of the cricoid with silicone glue (Sil-Poxy from Smooth-On, Inc., Macungie, PA, USA). Similar to other simulators [22], [23], the soft tissue around the cartilage was casted with silicone (Ecoflex 0030 from Smooth-On, Inc., Macungie, PA, USA) (Fig. 2(b)).

The skin covering the larynx is made of DRAGON SKIN 20 with embedded POWER MESH (both from Smooth-On, Inc., Macungie, PA, USA). This mesh serves to increase the tear resistance of the silicone when it is spread, making the skin more durable.

2) Animal and Human Specimens: In order to evaluate the haptic requirements of an artificial cricoid cartilage, the core of the physical haptic simulator, the forces applied to the LPIT during penetration were measured.For this purpose,porcineand human specimens were used as references. Ten larynges of 180-day-old pigs (sex unknown) provided by a farmer (Schickmair Florian

,Schickmair Ab-Hof-Vermarktung KG, Gunskirchen, Austria) served as reference structures (byproduct of meat processing). The porcine samples were tested in accordance with the Austrian Federal Act on Hygiene Requirements for Animal By-products and Materials Not Intended for Human Consumption (Tier materia liengesetz–TMG, BGBl. I Nr. 141/2003) at the University of Applied Sciences Upper Austria (Linz, Austria). The larynges were prepared and measured with in 24 hour safter slaughter (storage<4◦C,packed airtight). For the measurement, the surrounding soft tissue was removed and only the cricoid cartilage itself was measured. Due to deviations or damages during preparation, only 6 of them were actually measured.The specimens were fixed by casting the cricoid anterior arch with urethane casting resin (Smooth-cast 65D, Smooth-On, Inc., Macungie, PA, USA), taking care of not staining the areas to be tested due to the heat generated during curing.

The human larynges were provided by the Anatomy Donation Program of the University of Hamburg-Eppendorf, Germany, in accordance with the Human Tissue Act [24]. The sample measurements at the Institute for Biomechanics of BGU Murnau were approved by the Ethics Committee of the State of Bavaria, Germany. The Declaration of Helsinki has always been respected [25].

The measurements (n =12) of the human samples (age and sex unknown) were performed on a total of 18 human samples, excluding those of obviously damaged or deformed larynges (forensic medicine donations). Samples were stored at −37◦C, thawed 24h before preparation, embedded in polyurethane (Rencast FC53 A/B, Huntsman Advanced Materials, Basel, Switzerland) immediately after preparation (by pouring the cricoid anterior arch) and measured to avoid tissue altering “freeze-thaw” cycles [26]. Care was taken not to alter the relevant tissue by the polyurethane resin.

3) Force Measurement and Testing: Penetration of the cricoid cartilage occurred at the lamina, lateral to the central vertical ridge, in the middle of the depressions and in the direction from posterior to anterior (Fig. 2(a)). The angle of penetration was chosen perpendicular to the cartilage surface. This approach ensures no additional forces other than those in the insertion direction, also because the LPIT is stable enough not to deform. A K-wire with a diameter of 1.6mm was chosen as penetration tool, as it corresponds to the geometry of the LPIT used for surgeries. The tool was attached directly to the load cell with a needle holder, co-centric to the load cell with identical force axes. The test speed was at 10mm/min with a preload of 0.1N, and the specimens were positioned in such a waythat the entire cartilage was pierced when the measurement was completed. Thus the entire tip of the penetration tool was visible on the opposite side. During the measurements of one type of specimen, the penetration tool was not changed. The force curve was recorded as a function of the penetration depth into the cartilage. All measurements were performed according to this principle.

The measurement data of porcine larynges (n =12, two measurements from each of six samples, one on each side of the almost symmetrical larynxes) as well as those of the artificial cricoids (n =6, same

fixation as the porcine samples) were generated with a uniaxial testing machine (Zwick Z005, Zwick/Roell GmbH & Co. KG, Ulm, Germany) with a force transducer (Zwick/Roell Xforce HP 200 N, Zwick/Roell GmbH &Co.KG,Ulm,Germany which meets the criteria of accuracy classes according to ISO 7500-1). The measurement of the humanlaryngeal samples was carried out in the same way asthe porcine samples except that the testing machine was a Zwick Z010 (Zwick/ZO10,GmbH & Co. KG, Ulm, Germany)

In addition, experts (otorhinolaryngology surgeons collaborating with the MED-EL company) also assessed the haptics of the artificial cricoid cartilages.

C. Smart Artificial Soft Tissue

The central element of the simulator is an artificial soft tissue layer, positioned behind the cricoid cartilage instead of the PCA muscle, determining LPIT's position within it.

1) Hardware: The basic idea is to achieve electrical conductivity of an artificial soft tissue layer in order to use it as resistive sensor mat and detect voltage-carrying tools. Such a soft and elastic layer can be realized by incorporating conductive particles like carbon black into silicone [27]. In principle, various silicones corresponding to the mechanical requirements of the tissue to be imitated can be used, but it should be noted that the modulus of elasticity of the composite also increases as the carbon black content increases [28]. The more carbon black is added to the silicone, the better the conductivity [29]. The base material used here is Ecoflex 35 fast (58wt%, from Smooth-On, Inc., Macungie, PA, USA). In addition, isooctane (25wt%, 2,2,4-Trimethylpentan (≥ 99%) from Sigma-Aldrich, Inc., St. Louis, USA), Thinner (8.7wt%) and Slo-Jo (0.8wt%) (both from Smooth-On, Inc., Macungie, PA, USA) were added. Isooctane and Thinner reduce the viscosity of the liquid silicone , and Slo-Jo prolongs the polymerization time to ensure complete mixing before the silicone is cured. Carbon black (7.5wt%, XPB545POWDERfromORIONEngineeredCarbonsGmbH, Frankfurt, Germany), low dosed to hardly affect the haptics of the silicone, was used as conductive phase. Homogeneous mixing [30] was achieved using a speedmixer (DAC 600.2 VAC-PfromSynergy Devices Limited, High Wycombe, United Kingdom)andlowpressure(350hPa).ThisresultedinaSpecific Conductance of $\sigma = 10 mS \cdot m^{-1}$ for conductive layers (sensor mats).

Various tasks can be covered by such sensor mats. In the simplest case, only a basic circuit is closed by a contact between a sensor mat and an insertion tool to detect when the tool reaches a certain position in the artificial tissue. By dividing the sensor mat into several areas, a first approach for localization, similar to Esterer et al. [31] can be realized. Therefore, only one electrode per sensor mat is sufficient.

In a next step, one-dimensional position detection can be obtained by using the conductive silicone composite as a rectangular layer with two elongated electrodes on opposite sides. Insertion tools can be used to apply voltage somewhere between the electrodes. This allows the measurement of currents that

are inversely proportional to the ratio of the distances between the insertion point and the electrodes. Alternatively, by applying an electrical gradient field via the electrodes, a voltage, corresponding to the distances between the electrodes, can be tapped by insertion tools, similar to a potentiometer. This approach can also be extended to the two-dimensional case by using two orthogonal layers [32], [33]. To achieve a two-dimensional resolution, it is possible to use four punctual measuring electrodes (Pi, I =1...4), inserted in the corners of a single ,rectangular sensor mat as shown in Fig.3. This method is used in the LP-simulator and is considered in more detail. In contrast to O'Neill et al. [34], no voltages are injected into the electrode pins when determining the position, but a constant voltage UN is injected into the sensor mat by a voltage-carrying injection tool (the LPIT)at point PN. This variant closely represents real conditions, in which the muscles are stimulated by electrical currents from the LPIT. The distribution of partial currents on electrode pins are measured by voltages Ui on shunt resistors RS. Additionally, contact resistances Rci between sensor mat and electrode pins as well as LPIT RCN must be taken into account. By these measurements, resistances Ri, which depend on the distances ri between LPIT tip and electrode pins can be utilized for position determination.

2) Framework for Position Detection: Four resistance mappings Ri(pN) are assumed for the resistances between LPIT

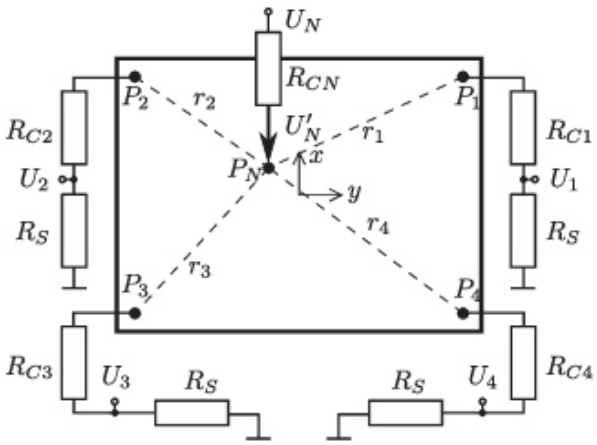

Fig. 3. Electrical circuit diagram of the sensor mat with electrode pins $P_i, i = 1 \ldots 4$ and LPIT insertion point P_N. Distances r_i are defined by $\overline{P_N P_i}$ and measured pin voltages are given by U_i. Specific contact resistances for pins and LPIT are R_{Ci} and R_{CN} respectively. R_S denotes a known shunt resistance.

tip and the electrode pins Pi depending on LPIT tip position pN =(x,y),withthecoordinate origin in the sensor mat center (Fig. 3). These mappings can be obtained either from resistivity measurements, from finite element simulations, or from simplif ied model considerations. From them, the LPIT x-coordinate can be estimated by a general position reconstruction field

$$\vec{f}(\vec{p}_N) = \vec{\phi}\,(R_1(\vec{p}_N), \ldots, R_4(\vec{p}_N)) \qquad (1)$$

to be defined, which depends on all Ri(pN), where its com ponents must be strictly monotonic with respect to the x- and y-coordinate respectively. The LPIT tip position can then be reconstructed from φ

by inversion pN = f−1(φ(R1,...,R4)) or better by approximation of the inverse mappings with suitable functions. The freedom to define function φ in (1) can be used to achieve a position reconstruction mostly independent from unknown and typically varying contact resistances RCi and RCN respectively. Finally the sensor resistances Ri are not measured directly and thus they are estimated by pin voltage readings Ui. Contact resistances RCi are obtained from a calibration routine (chapter II-C6), which has to be executed before using the sensor system.

3) Finite Element Simulation: In order to gain the resistance mappings Ri(pN) the smart artificial soft tissue was simulated with the Finite Element Method. A two-dimensional approach for the unwound mat was chosen since the thickness of the mat(s =1.5mm)is small compared to its outer dimensions. Moreover, the cylindrical, gold-plated electrodes with smooth surface completely penet rate the mat,whichiswhythegeometry to be simulated is constant in the Z-direction. The simulation wascarriedoutwithMatlab'sPartialDifferentialEquationToolbox[35]withGauss'slawdescribingelectro staticsofconductive materials

$$\sigma \nabla^2 V = 0 \text{ in } \Omega \qquad (2)$$

with $\vec{n} \cdot \nabla V = 0$ on $\partial\Omega_B$, $\vec{n} \cdot (\sigma \nabla V) = -\sigma_i V$ on $\partial\Omega_E$ and $V = U'_N$ on $\partial\Omega_N$. Hereby $V(x, y)$ is the electric potential, σ

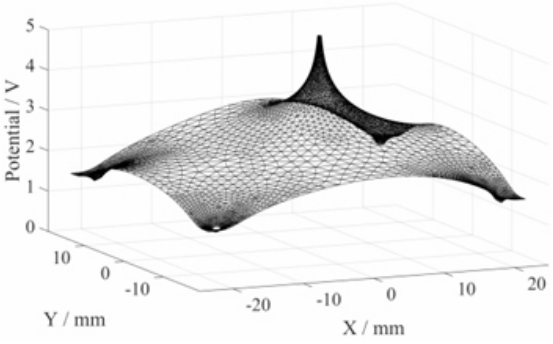

Fig. 4. Finite element simulation of the electrical potential field $V(x, y)$ in the sensor mat. The LPIT penetration point was at $x = 6$ mm and $y = 5$ mm. The dimensions of the sensor mat are 45 mm $\times 35$ mm where the electrode pins are placed 2.5 mm away from the outer edges of the mat in each direction achieving $L = 20$ mm and $W = 15$ mm respectively.

the conductivity of the sensor mat and σi the conductivity of electrode pin Pi. The pin diameter was chosen as d =1mmand the rectangular area spanned between the pins as 2L × 2W, Ωdenotes the entire sensor domain and n is the normal vector to the boundary ∂Ω. The free border of sensor mat ∂ΩB as well as electrodes ∂ΩE were Neumann boundary conditions, where the current density for shunt and contact resistance is defined by σiV. The pin conductivity σi was obtained from series connection of RCi and RS. On LPIT contact point ∂ΩN a Dirichlet boundary condition defined the injected LPIT voltage UN. Fig. 4 shows the field V(x,y) for a rectangular sensor domain.Due to shunt resistors RS,the pote ntialis

drawn towards ground at the four electrode pins located at sensor mat corners, while the voltage-carrying LPIT pulls the electrical potential towards supply voltage.

4) Position Reconstruction Field: A possible choice for the reconstruction field φ relies on the simplified model assumption that the electrical resistances Ri between LPIT tip PN and electrode pin locations (Pi, I =1...4) as illustrated by Fig. 3 are proportional to the corresponding distances ri = PNPi.By simple geometrical considerations the normalized coordinates xn =x/Landyn = y/W can be obtained from distances ri as follows

$$x_n = \frac{r_1^2 - r_2^2}{(2L)^2} = \frac{r_4^2 - r_3^2}{(2L)^2}, \qquad (3)$$

$$y_n = \frac{r_3^2 - r_2^2}{(2W)^2} = \frac{r_4^2 - r_1^2}{(2W)^2}, \qquad (4)$$

where 2L and 2W are the distances between the electrodes respectively. Since Ri = ρ/A ri, where ρ denotes the specific electrical resistance and A a cross-sectional area assumed to be constant, distances in (3)–(4) can be approximated by corresponding resistances. In order to achieve a reconstruction f ield which is mainly independent on contact resistances the following strictly monotonic field φ =(φx,φy) is proposed

$$\phi_x = \frac{1}{2}\left(\frac{\Delta\alpha_1^2 - \Delta\alpha_2^2}{\Delta\alpha_{hor}^2} + \frac{\Delta\alpha_4^2 - \Delta\alpha_3^2}{\Delta\alpha_{hor}^2}\right), \qquad (5)$$

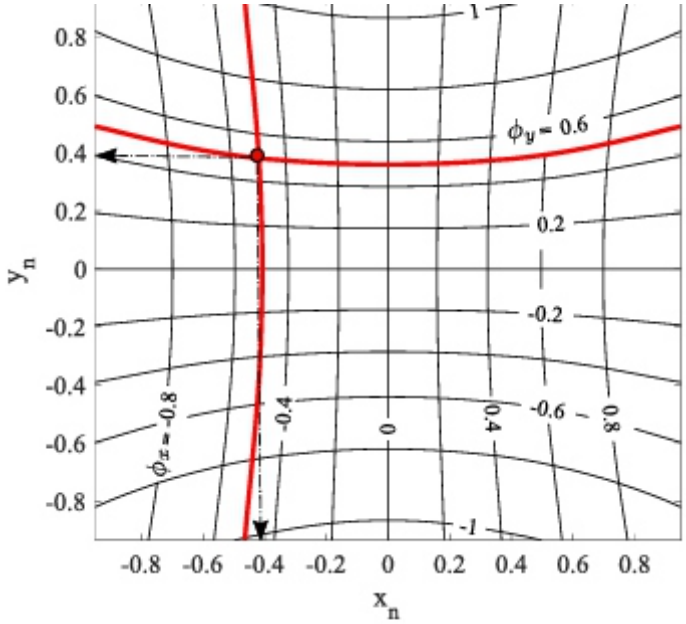

Fig. 5. Contour plot for position reconstruction field components ϕ_x and ϕ_y depending on normalized LPIT coordinates x_n and y_n. The location of intersection of the contour lines $\vec{\phi} = (-0.5, 0.5)$ corresponds to the desired normalized LPIT coordinates $\vec{p}_N = (-0.4, 0.4)$.

$$\phi_y = \frac{1}{2}\left(\frac{\Delta\alpha_3^2 - \Delta\alpha_2^2}{\Delta\alpha_{ver}^2} + \frac{\Delta\alpha_4^2 - \Delta\alpha_1^2}{\Delta\alpha_{ver}^2}\right). \qquad (6)$$

Here $\Delta\alpha i = \alpha i - \alpha i,min$ denotes the range of the position dependent resistance ratio αi for pin Pi with

$$\alpha_i = \frac{\hat{R}_i}{\sum_{i=1}^{4} \hat{R}_i},\ \hat{R}_i = R_i(\vec{p}_N) + R_{Ci} + R_S. \qquad (7)$$

The value $\alpha i,min$ is the resistance ratio αi if the LPIT is placed next to pin Pi, where the position dependent resistance Ri will tend to zero. The mean horizontal range $\Delta\alpha hor = mean(\Delta\alpha 1,hor,\Delta\alpha 4,hor)$ considers with $\Delta\alpha i,hor = \alpha i,max - \alpha i,min$ the horizontal distances of the electrodes. Here, $\alpha i,max$ is obtained when the LPIT is placed next to the horizontally adjacent pin of Pi such that the position-dependent resistance Ri is maximized (for purely horizontal deflection). Consequently $\Delta\alpha ver = mean(\Delta\alpha 3,ver,\Delta\alpha 4,ver)$ defines resistance ratio ranges between vertical adjacent pins. All these values can be obtained during a calibration procedure prior to the usage of the sensor system as discussed in the sequel.

Fig. 5 shows the contour plot of φx and φy respectively obtained from simulation of the sensor mat with conductivity ratio $\gamma = \sigma i/\sigma = 1.0$. Since φx and φy obtained from (5)–(6) are closely related to normalized coordinates xn and yn,thereconstruction field components can be utilized to reconstruct the LPIT position. Observing the contour lines for $\varphi = (-0.5,0.5)$ highlighted in Fig. 5, it can be perceived that the x− and y−coordinates of their intersection (−0.4,0.4) are the desired LPIT coordinates. If the grid defined by the contour lines of reconstruction field defined a regular, orthogonal grid, the normalized LPIT coordinates would bedirectly taken from the field components φx and φy respectively. However, due to boundary effects this is only true in a small region around the center of the sensor mat. Near to the edges of the sensor the contour lines are distorted. Therefore for position reconstruction the inverse of f provides the desired instrument coordinates. Since there sistance mappings for there construction field are available, its inversion can be approximated by suitable functions to obtain the instrument coordinates as

$$x_n = f_x^{-1}(\phi_x, y_n) = \left(a_x + b_x\phi_x^2 \exp(c_x y_n^2)\right)\phi_x \qquad (8)$$

$$y_n = f_y^{-1}(x_n, \phi_y) = \left(a_y + b_y\phi_y^2 \exp(c_y x_n^2)\right)\phi_y \qquad (9)$$

with parameters $\theta = (ax,...,cy)$ to be determined by fitting these functions to data obtained from simulation. To account for different sensor mat conductances σ and pin conductances σi numerous simulations for different ratios $\gamma = \sigma i/\sigma$ in the interval $\gamma \in [0.1,2.5]$ were performed. In case of a quadratic sensor domain with L = W the parameters were equal for both reconstruction fields due to symmetry reasons, therefore ax = ay, bx = by and cx = cy. For reasons of clarity, the parameter estimation was performed for such quadratic sensor domains with different values for L in the interval $L \in [30,100]$mmwith step size of 5mm.

For each simulation setup and therefore conductivity ratio γ and L the unknown parameter vector $\theta(\gamma,L)$ was determined by a nonlinear least squares method (Levenberg-Marquardt Algorithm, [35]).

The model quality for all performed parameter estimations was quantified by q =1− min(ˆ y−y / y ,1) where y denotes used reference values and ˆ y the fitted ones. Assuming a given conductivity ratio γ, then the latter defined inverse functions were derived by obtaining the parameter vector θ(γ,L) from computed parameter vectors by linear inter polation. Thus the position detection method is able to adopt to a current system setup, where the sensor mat conductivity, as well as pin contact resistances may have been changed since last the application. In turn the instrument position can be obtained by solving equation system (8)–(9) for xn and yn respectively, which is practically obtained by computing the intersection of both equations.

5) Voltage Readings: Pin voltages Ui are measured by means of four shunt resistors RS with a 10 b analogue digital converter of the micro controller (ATMEGA 32U4, Atmel Corporation, San Jose, USA). From the electrical circuit diagram in Fig. 3 one can conclude that ˆ Ri =UN/Ui ·RS. Therefore the ratio αi as defined by (7) can be obtained directly from voltage readings as

$$\alpha_i = \frac{U_i^{-1}}{\sum_{i=1}^{4} U_i^{-1}}, \qquad (10)$$

which becomes completely independent from UN and thus from LPIT contact resistance RCN. From a practical perspective this is critical for success, since the LPIT contact resistance depends on the intensity of LPIT contact or penetration as well as on non-conductive particles which may influence the conductivity between LPIT tip and sensor mat. These influences would have a strong impact on the accuracy of the position reconstruction.

6) Calibration: Before as imulated surgical procedure using the Smart Artificial Soft Tissue for LPIT position tracking can be started, a newly inserted sensor mat has to be calibrated to compensate for any deviations of the sensor mat's conductivity or changed contact resistances. Since the contact resistance between the electrodes and the car bon black-silicone composite depends mainly on the geometry and material of the elements and particles in contact [36], a constant and equal contact resistance RCi = RC for I =1...4 is assumed. The fact that the sensor matis fixed in the area of the electrode pins by a fastening clamp and thus very limited deformations or movements are possible in these areas supports this assumption. Further it is assumed that the conductivity σ of the sensor mat remains constant over a normal period of usage.

For calibration the LPIT is placed onto the sensor mat as closely as possible to each of the four electrode pins Pi which provides ratios αi,min and αi,max as required by equations (5)(6) where ratio αi is obtained from voltage readings according to (10). Hereby several voltage readings are averaged over a certain time period in order to obtain more robust results. All other ratios for Δαhor and Δαver can be obtained accordingly.

In addition, it is important that all contact resistances Rci are equal and sufficiently small. This can be checked by the micro controller's general purpose I/O pins. If the LPIT is placed next to a pin it is set to

the supply voltage U0 while all others pins are set to ground. Switching the I/O pin connected to the LPIT to high impedance in put allos to measure the mat voltage Uniby the LPIT tip. Denoting the mat resistance between active pin Pi and all other pins with R||, which is serial to the contact resistance RCi, results in

$$\frac{R_{Ci}}{R_{mat}} \approx \frac{1}{3}\left(\frac{U_0}{U_{Ni}} - 1\right). \qquad (11)$$

This assumes that R|| ≈ 1/3Rmat and thus the resistance to all adjacent pins is approximately equal. This ratio can be utilized to estimate the size of the contact resistance. If the ratio in (11) is below 0.1, the contact of the sensor mat is considered to be sufficient.

Another characteristic parameter of the sensor mat to be determined is the conductivity ratio γ, which is the ratio of pin conductivity σi to mat conductivity σ. The pin conductivity is related to the series connection of contact and shunt resistance. Simulation experiments revealed that this ratio can be estimated from

$$\gamma = k\left(\frac{1}{U_i/U_j - u_0} - 1\right) \qquad (12)$$

the voltage driven LPIT is placed in its immediate proximity and Ui denotes the voltage measured at the diagonal adjacent pin Pi. Hereby the parameters k and u0 can be obtained by nonlinear least squares estimation from simulation experiments for different γ. Since the required voltage readings in (12) can be obtained during the calibration procedure, the conductivity ratio is defined for the sensor mat in use. Consequently the parameters for inverse functions (8)–(9) can be obtained from linear interpolation which in turn allow to compute the LPIT position by the proposed framework.

7) Verification and Validation: The proposed position reconstruction method was verified by simulation experiments

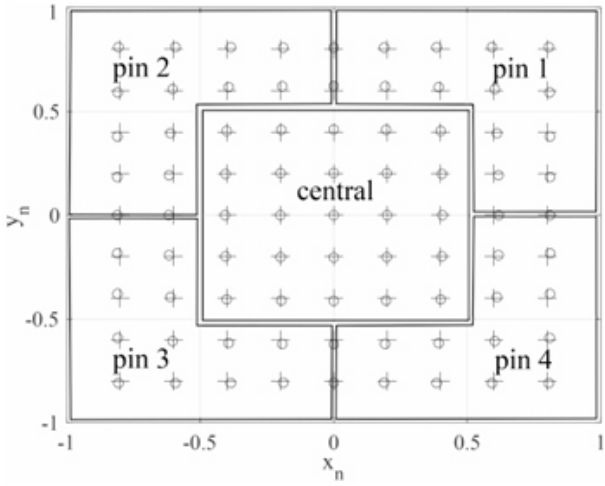

Fig. 6. Comparison of predefined and reconstructed LPIT positions: (+) denotes the exact and (o) the reconstructed position. The sensor mat is divided into a central and four pin regions in order to compute the region specific accuracy.

TABLE I
SIMULATED POSITION RECONSTRUCTION ACCURACY: MEAN ERROR AND STANDARD DEVIATION IN % OF NORMALIZED COORDINATES FOR CENTRAL AND PIN REGIONS

case	central	pin 1	pin 2	pin 3	pin 4
I	0.23±0.14	0.72±0.10	0.72±0.10	0.72±0.10	0.72±0.10
II	0.29±0.20	0.76±0.26	0.76±0.26	0.76±0.26	0.76±0.26
III	2.20±1.31	1.25±0.35	3.00±1.41	6.46±1.51	3.61±1.28
IV	1.88±1.11	1.13±0.60	2.57±1.12	4.74±0.96	2.77±1.31
V	3.79±1.89	1.89±1.05	4.43±2.10	9.98±2.27	7.65±2.33

The accuracy of the position reconstruction was quantified by the mean error with respect to desired, normalized positions. In order to investigate the results from different parameter studies the sensor mat was divided into five regions, one central region and four electrode pin regions as indicated in Fig. 6. Especially the central region was important for the application in mind, since the PCA muscle resides in this region and thus an accurate LPIT position was important for hotspot detection. Within these regions the average of the mean error and its standard deviation were computed. Hence, it was possible to investigate the influence of different parameter settings on the accuracy of the reconstruction method. Five different cases were examined for this purpose, which will be discussed in more detail in the description of Table I (chapter III-B1).

For validation purposes the proposed position detection method was implemented on ATMEGA 32U4 in C++. A template with 7 ×9 equidistant positions in a range of 32mm ×26mm around the origin was printed and placed over the sensor mat inside the opened simulator case. Then the LPIT was placed on the predefined positions where the computed LPIT position in turn was transmitted over the serial interface to the simulator software and stored for further processing .These measurements were repeated on twelve identically manufactured sensor mats. The mean error and the corresponding standard deviation were computed for the referenced regions.

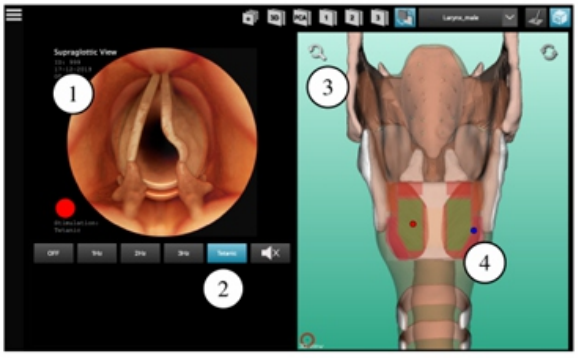

Fig. 7. Software as virtual part of the simulator. (1) Vocal fold animation, (2) Stimulation control buttons, (3) 3D-view of the anatomy, (4) Display of insertion points (blue and red dot).

D. Virtual Simulator Components

The software for the hybrid simulator as shown in Fig. 7 is based on Qt-C++ Framework (Version 5.12.4) using VTK (Version 8.2.0) for 3D-visualization. The user interface is divided into different

areas. On the left, during the initial part of the insertion phase, a live video stream of an endoscope is shown in order to monitor the tunneling of the LPIT under the synthetic mucosa of the laryngeal phantom. When penetrating the cricoid surface, one can proceed to a virtual simulation of the end oscopically observed vocal folds (1). Depending on the position of the LPIT, different movement patterns of the vocal folds are induced by electrical stimulation. When the hotspot is reached by the LPIT, the vocal folds move laterally and thus simulate an opening of the glottis. Otherwise the simulation shows an adverse reaction e.g. closing of the vocal fold or a mixed reaction of closing and opening. Buttons for controlling the electrical stimulation (OFF/1 Hz/2 Hz/3 Hz/Tetanic) are positioned underneath (2). Optionally anacoustic signal indicating the stimulation impulses can be enabled. Both, endoscope view and control elements for electrical stimulation are typically available for the real surgical intervention. The right side of the user interface provides additional information to support teaching and learning. The 3D anatomy view of the larynx (3) can berotated, moved and zoomed by the trainee which supports learning anatomy or helps to identify critical anatomic regions. The core task, the correct positioning of the LPIT into the PCA muscle, can be facilitated by the view of target areas (4). The positions of the LPIT tip in the PCA muscle are indicated by red and blue dots, since two electrodes are supported and thus the correct positioning of the instrument tips can be verified easily. The target areas or hotspots are colored green while sub-optimal areas are colored orange or red.

E. Physical Simulator Components

A phantom combining hybrid requirements as well as haptics and position recognition with their component sis shownin Fig.8 (Housing and support structures made of 3D-printed Ultimaker Tough PLA from Ultimaker B.V., Utrecht, Netherlands). The

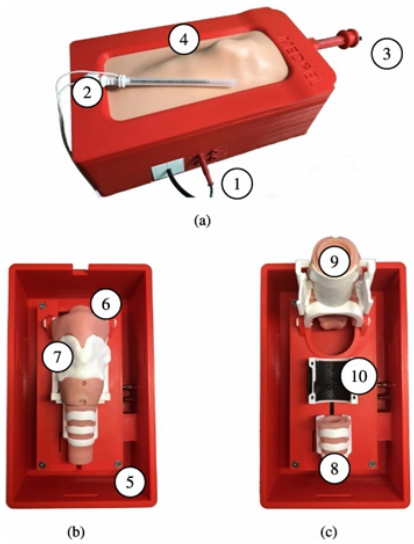

Fig. 8. Inner structure of the physical simulator part, housing dimensions ($L \times B \times H$): $L = 200$ mm, $B = 120$ mm, $H = 70$ mm; (a) closed and ready to use system, (b) opened simulator, (c) disassembled inner anatomies. (1) connections for LPITs and USB-interface, (2) LPIT, (3) USB-endoscope, (4) artificial skin, (5) base plate with integrated circuits, (6) simplified representation of thyroid membrane, hyoid bone and epiglottis, (7) thyroid cartilage, (8) ligamentum cricotracheale with cartilage rings, (9) artificial, replaceable cricoid cartilage, (10) sensor mat.

physical simulator can be connected to the other simulator components via the laterally mounted connectors (1). A micro USBport connects the micro controller to the computer and the simulator software. The LPITs (2) are connected via 1.5mm banana plugs (1). Four connectors allow to connect two LPITs consisting of canula (outer part) and trocar (inner part) each. The canula shows a backward offset of 3mm and is electrically insulated from the trocar. Thus the canula can be used to detect whether the LPIT was inserted too deeply representing apenetration of the esophagus.AUSB-endo scope(3) provides a sub-and supra-glottic view into the simulator's interior. By removing the artificial skin (4), the inner structures of the simulator become visible. The base (5) contains the electronic circuits and the micro controller. The elements (6), (7) and (8) are not penetrated during simulation. Thus they are made of more durable material. In contrast, the cricoid with its adjacent tissue (9), which has to be changed regularly, as well as the sensor mat underneath (10) require arealistic haptic perception when inserting the LPIT into the artificial anatomy.These wear parts can be replaced by lifting the parts (6) and (7) upwards and sliding the artificial trachea

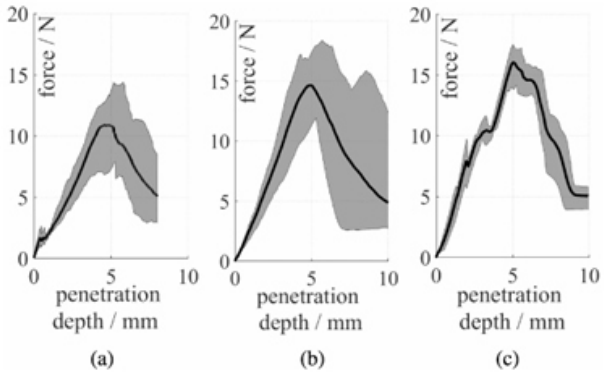

Fig. 9. Force measurements during penetration of the cricoid cartilage with a needle geometrically corresponding to the LPIT. The arithmetic mean (black line within the gray area), minima (lower boundary of the gray area) and maxima (upper boundary of the gray area) are shown. (a) Measurements from human samples, (b) measurements from porcine samples (c) measurements from artificial cricoid.

(8)downwards.After reassembly ,the structure sare covered with synthetic skin (4) and soft tissue again.

III. RESULTS

A. Tissue Measurements

The artificial cricoids and the human and porcine specimens were compared on the basis of four characteristics: Maximum force, number of dominant peaks, peak distance and the morphology of the measurement curve (Fig. 9). For haptic evaluation, in both the human (Fig. 9(a)) and the porcine samples (Fig. 9(b)), one dominant peak between 10 N and 15 N was detected. Thereby the forces in the porcine samples (maximum of mean force curve ˜ fmax =14.7N; [range 12.0−18.4 N]) were slightly

higher than in the human samples(˜ fmax =10.9N; [range 7.9−14.4N]),although the force ranges of the individual measurements partially overlapped. In addition, a characteristic, small and sharp peak at the beginning of the measurement curve (< 1mm)wasnoticedinthehumansamples.Fromthedistance between the two peaks or from onset to the dominant peak, sample thickness of about 5mm can be estimated.

With the help of surgical experts, different material compositions were evaluated and the artificial cricoid introduced in chapter II-B1 was identified as the most realistic imitation (Fig. 9©). As with the human samples, the artificial cricoid (Fig. 9©) proved the second peak (˜ fmax =16.02N; [range 14.1−17.4N]) to be more dominant than the first. Furthermore, spacing between the two peaks was similar to the human samples. Although similarly sharply edged, the first peak of the artif icial was somewhat higher than the human one. The maximum force corresponds to those of the biological references.

B. Smart Artificial Tissue

1) Simulation: The parameters for the inverse functions ac cording to (8)–(9) were computed for 16 different dimensions of the sensor mat with 16 different conductivity ratios γ for

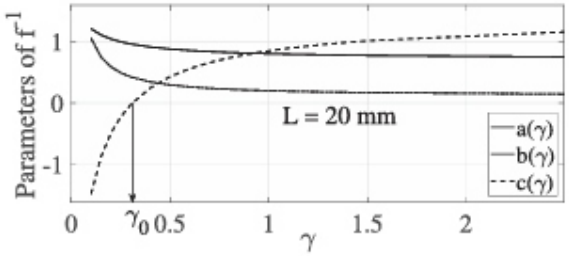

Fig. 10. Parameters for approximation of f_x^{-1} and f_y^{-1} for a quadratic sensor domain as a function of conductance ratio γ. The different conductance ratios were obtained by changing conductances of pin contact resistance and sensor mat accordingly.

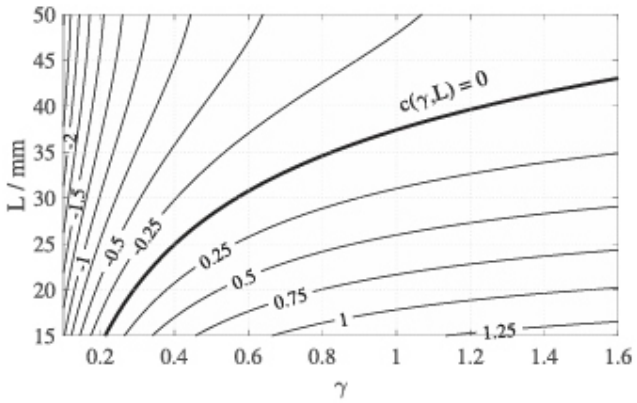

Fig. 11. Contour plot of parameter field $c(\gamma, L)$. The conductivity ratio where the parameter field c is zero is denoted as $\gamma_0(L)$. For this configuration the distortion of the reconstruction grid is minimized.

each simulation case. The mean value of the model quality q for all 256 models obtained from nonlinear optimization was 97.04 ± 0.46% for f−1 x andf−1 y respectively.

Generally, the parameters a,b and c for a quadratic sensor domain with L =20mm depending on the conductivity ratio γ are depicted in Fig. 10. The parameter c is directly related to the distortion of the grid given by the contour lines of the reconstruction field φ as depicted in Fig. 5.Forc<0 a concave grid distortion results from rather high pin contact resistances and for c>0 a convex distortion is obtained for lower contact resistances. If parameter c =0, then the distortion of the reconstruction grid is minimized. Fig. 11 depicts the contour lines for the parameter field c(γ,L). The contour line where c =0denoted by γ0(L) represents an adjusted sensor system, where the distortion of there construction gridis minimized. The adjustment can be done by changing the shunt resistances so that the conductivity ratio γ = γ0(L).Parametera is connected to the slope of the reconstruction field around the origin and parameter b represents boundary effects along the edges of the sensor domain. Both parameters and the diagonal voltage ratio Ui/Uj are shown in Fig. 12(a) for an adjusted sensor system along γ0 for different sensor domain dimensions L. The diagonal voltage ratio according to (12) represents the ratio between smallest and highest possible pin voltages. The smaller this ratio, the higher the sensitivity of the position reconstruction method.

The conductivity ratio γ, which turned out to be a characteristic parameter, can be estimated by (12) for different sizes L of the sensor domain by means of calibration readings. The mathematical model was fitted to simulation data. The result is depicted in Fig. 12(b) and shows the conductivity ratio depending on diagonal voltage ratio for different dimensions L. Hereby a model quality of 99.74% was achieved. Concluding, the proposed position reconstruction algorithm is summarized by the following steps: i) First perform the calibration routine and obtain the conductivity ratio γ according to Fig. 12(b), then ii) from parameter fields a (γ,L),b(γ,L)andc(γ,L)asdepicted in Fig. 11 and 10get the reconstruction field parameters, and iii) compute function (8)–(9) from voltage readings according to (10) and obtain the normalized instrument coordinates xn and yn respectively.

This algorithm was performed for different simulation cases, where the mean and standard deviation of the position reconstruction error in different regions of the sensor domain is summarized in Table I. The dimension L of the quadratic sensor domainwasL =20mm.Thusa10%errorinnormalized coordinates was an absolute error of 0.1L =2mm. For case I, III-V the conductivity ratio was γ =0.15, for case II γ =0.3. Case I and II used a nominal contact resistance equal for all pins. Case III had 10% contact resistance increase at pin P4, case IV a 10% decrease at pin P1 and case V a 10% decrease at pin P2 in combination with a 10% increase at pin P4.For simulation cases I and II, where the pin contact resistance was equal for all pins, the accuracy in the central region was below 0.3 ±0.2% in % of normalized coordinates. The error in the pin regions was approximately 2.5-fold higher as in the central region. Simulation cases III–V showed theeffect of different pin contact resistances. The largest error

was observed for case V in region pin 3 with 9.98 ± 2.27% in normalized coordinates. Hereby the pin contact resistance was reduced by 10% at pin P2 and at the diagonal adjacent pin P4 the contact resistance was increased by 10%.

2) Validation: To validate the position reconstruction using measurement data, twelve sensor mats were analyzed using a grid with 7 × 9 holes for predefined LPIT positions (Fig. 13). Based on these measurements, the mean errors and corresponding standard deviations in % of normalized coordinates (or in absolute values) were 7.04 ± 3.28% (1.23 ± 0.59mm) for the central region, 9.52 ± 5.33%(1.59 ± 0.85mm)forpin1region,

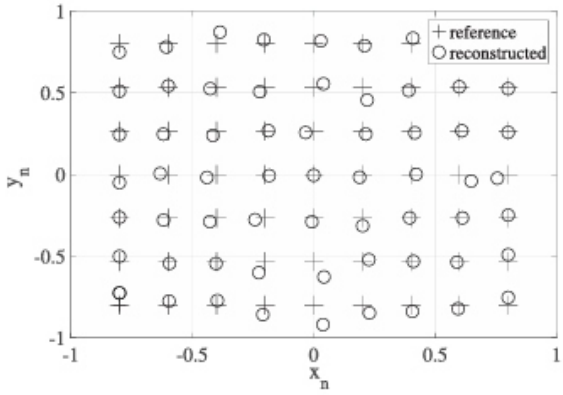

Fig. 13. Comparison between real position values (+) and measured positions (o) as average of 12 measurements. A grid of 7 x 9 with a grid size of 4mm in each direction was used.

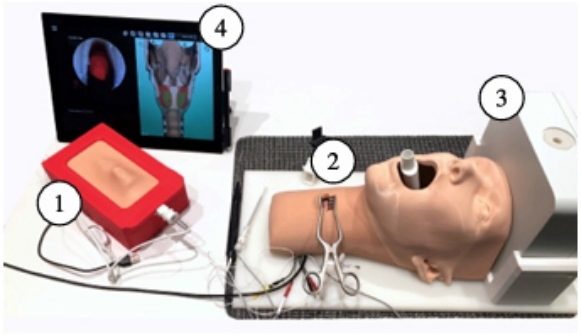

Fig. 14. Final simulator with all components; (1) simulator in box, (2) simulator with head and neck replica for more realism (high fidelity trainer), (3) electromagnetic position tracking system, (4) tablet-computer for virtual extension.

C. Final Setup

The complete setup with two different versions of the simulator can be seen in Fig. 14. Either the simplified, more mobile version can be used (1), or the more advanced version (2), which is additionally equipped with electromagnetic tracking (3) (NDI Aurora, Planar 20-20 V2 from NDI Europe GmbH, Radolfzell, Germany) of the LPITs. The movements of the LPIT induced by the trainees can be tracked throughout the simulation and subsequently evaluated. This is achieved via

sensor coils attached directly to the LPIT or other tools. The simulator's internal hardware, which enables realistic haptics as well as position detection of the insertion LPITs in the sensor mat, is identical for both variants. In the advanced variant, however, the use of a medical endoscope is possible, which can be inserted into the patient phantom via the replica of alaryn geal mask. In the simpler variant, the endoscope is replaced by a movable, inexpensive USB-endoscope. The software adapts to the variant used and can be integrated via an ordinary computer (4). To achieve the hybrid character of the simulator, the visual simulation of the vocal fold movement on the screen adapts to the position of the LPIT. Consequently, this connects the virtual and physical component, which, in turn, enables feedback on the surgery performed on the physical part. As shown in Fig. 14 (below (2)), additional surgical instruments such as spreader, forceps and needle holders can be used without limitation. Also sutures can be placed to mimic and train the implantation procedure more accurately.

IV. DISCUSSION

A. Usability and Haptics

Fig. 13. Comparison between real position values (+) and measured positions (o) as average of 12 measurements. A grid of 7 x 9 with a grid size of 4mm in each direction was used. Fig. 14. Final simulator with all components; (1) simulator in box, (2) simulator with head and neck replica for more realism (high fidelity trainer), (3) electromagnetic position tracking system, (4) tabletcomputer for virtual extension. 9.44 ± 6.02%(1.57 ±0.94mm)forpin2region,9.18 ± 5.18% (1.51 ± 0.82mm) for pin 3 region and 9.57 ±5.11% (1.61 ± 0.82mm) for pin 4 region respectively. C. Final Setup The complete setup with two different versions of the simulator can be seen in Fig. 14. Either the simplified, more mobile version can be used (1), or the more advanced version (2), which is additionally equipped with electromagnetic tracking (3) (NDI Aurora, Planar 20-20 V2 from NDI Europe GmbH, Radolfzell, Germany) of the LPITs. The movements of the LPIT induced by the trainees can be tracked throughout the simulation and subsequently evaluated. This is achieved via sensor coils attached directly to the LPIT or other tools. The simulator's internal hardware, which enables realistic haptics as well as position detection of the insertion LPITs in the sensor mat, is identical for both variants. In the advanced variant, however, the use of a medical endoscope is possible, which can beinserted into the patient phantom via thereplica of alaryngeal mask. In the simpler variant, the endoscope is replaced by a movable, inexpensive USB-endoscope. The software adapts to the variant used and can be integrated via an ordinary computer The main objective was to develop synthetic tissue with position evaluation capabilities (Smart Artificial Soft Tissue) with an associated easy-to-use surgical simulator for demonstration. The physical patient phantom with its realistic haptic perception during LPIT insertion must fulfill three prerequisites that are challenging to combine. First, all relevant anatomical parts

should be manufactured as realistic as possible. Second, manufacturing effort should be kept as low as possible to be cost-effective. Third, the phantom must be easy to disassemble so that the wear parts, sensor mat and cricoid, can be easily replaced and the simulator can be simply reassembled after wards (time consumption is less than two minutes). This ensures the reusability of most of the simulator, which is unfortunately not achieved by many other physical simulators [8]. These, as well as other previously mentioned requirements of the involved surgical experts and their feedback were integrated throughout this work. The needle insertion forces were mainly influenced by their experience [37] and verified by biomechanical measurements, also because no references from clinical practice are yet available due to the novelty of the intervention. Application examples of the simulator including videos can be found in the supplementary material. Regarding the reusability of penetrated parts such as the cricoid, it is known from Esterer et al. [31] that a significant drop in insertion forces occurs after 10-15 penetrations at identical insertion points. This behavior was also observed with the artificial cricoid. Since subsequent trainings on the simulator hardly lead to identical penetration points, it is proposed to change the cricoid and sensor mat after every 20-30 simulations.

The software is simple, symbolic, and can be operated entirely via touch screens. Like in real surgery procedures, various surgical instruments can be used additionally. This ensures maximum realism in terms of dexterity and haptics.

According to the experts, both peaks in the force progression of the artificial cricoid are essential, as two pressure points are always clearly notable when penetrating the cricoid. An optimisation of the force profile was achieved by the reduction of the wall thickness and the additional coating mentioned in chapter II-B1. This led to the crucial first peak. Thus, both the expert knowledge and the information of the measurement data were incorporated. As some natural spread is always present in organic tissues, the artificial cricoids are considered haptically similar enough (especially with regard to the characteristics mentioned in chapter III-A) to ensure realistic training.

The success of a surgery completed on the simulator can be read directly from the position of the inserted electrodes. The quality of the surgery can be quantified by the number of retractions or too deep penetrations. With the high-fidelity version, it is also possible to record the tool path directly inside the phantom for detailed analysis and discussion in a debriefing session.

B. Calibration and Contacting Problems

The calibration of the sensor should compensate for in homogeneities and take the changes of the contact resistances into account after replacing the sensor mat. High resistance contacts are caused, for example, by the concentration, distribution and shape of the conductive carbon black particles embedded in the silicone as well as the geometry of the contact point [36]. In contrast to others [34], the contact resistance between sensor mat and the electrodes was reduced by increasing the contact

pressure of the clamp holding the sensor mat and by using gold electrodes. Increasing the diameter of the electrodes and thus the contact area also had a positive effect on the undesired resistances. Calibration requires to open and disassemble the simulator and to place the LPIT beneath the electrode pins. Calibration with out manual intervention of the user could be realized with four double electrodes ,which allows to measure the contact resistance directly. However, this would lead to considerably higher cabling and electronic hardware costs, especially if more than one sensor mat will be operated simultaneously.

C. Positioning Accuracy and Further Application

In contrast to other, contact-based position sensing in hybrid simulators [31], the developed Smart Artificial Soft Tissue offers the advantages of continuous, two-dimensional position detection. The accuracy of the proposed position reconstruction method depends strongly on the conductivity ratio between electrode pins and sensor mat. Therefore it is recommended to adjust the shunt resistors accordingly to achieve a mostly undistorted reconstruction grid. The estimation of the conductivity ratio by means of calibration measurements allows to optimally adjust there construction method to current operation conditions. The calibration routine should be performed once a day, typically when starting the simulator. Thus the usability is only slightly affected by performing the calibration procedure. The reconstruction accuracy is sufficient with an average deviation of 1.23mm in the central region for accurate hotspot detection. Larger errors only occur along the borders of the sensor domain due to unavoidable local stresses on the sensor mat or in homogeneities due to manufacturing inaccuracies. However, errors in these areas are not critical and hardly pose any problems for the simulated intervention. Since the optimal areas in the PCA muscles vary for different patients and have a size of about 9 × 18 mm, the accuracy is sufficient for an efficient training. Additional averaging of several measurements further increases the accuracy.

Bending of the car bon black-silicone composite hardly affects the results due to the thinness of the sensor mat in relation to the bending radius and the method of position determination. The resistance changes due to low strain and compression resulting from bending partially compensate ,although not completely due to non linearity [28], [29]. The remaining minimal change in resistance is uniformly distributed over the mat an dis compensated by the calibration (fitting the system to the general resistance conditions). These assumptions are confirmed by the results, since the morphology of the determined positions corresponds to that of the real positions.

With the actual setup, the pin voltages are measured directly with a 10-bit ADC of the used micro controller, which limits the position accuracy, especially when small position changes occur or the LPIT is near the boundary of the sensor domain. The absence of more complex electrical circuitry is intended to demonstrate the robustness of this technology even under unfavorable conditions. To

establish it as a basic element for future hybrid surgery simulators, the functionality was demonstrated with the simplest possible elements. A possible improvement would be the usage of differential amplifiers with programmable gains. This would allow to adopt the gains to maximize measurement resolution. A further accuracy improvement would be possible by introducing additional measuring electrodes along the boundary of the sensor mat. However, this would be accompanied by a higher system complexity and an increased number of components.

For future projects, the Smart Artificial Soft Tissue developed here can be used for various biopsy simulators or similar, in which conductive tools are inserted into tissue. This would provide a new basic element to accelerate the development of future hybrid surgical simulators as well as a post-simulation automatic evaluation capability that is missing in many physical simulators [8].

V. CONCLUSION

Smart Artificial Soft Tissue offers a fundamental key element for hybrid simulators which was demonstrated by a surgical simulator for implanting the electrode so falary geal pacemaker. The sensor technology is based on the inversion of resistance mapping between a conductive sensor layer made of carbonblack-silicone composite and a voltage carrying surgical instrument in contact. With this type of sensor technology ,it is possible to extract relative position data from surgical instruments in haptically adapted soft tissue-mimicking artificial anatomies with sufficient accuracy.

ACKNOWLEDGMENT

This work has been made possible by the support of Johannes Kagerer and Natalie Ing from MED-EL. Furthermore, the authoeers would like to thank Martin Winkler for his support in the preparation of the human specimens, Markus Samrykit for his support in the measurement of porcine specimens and Stefan Gabauer for his support with the initial prototype.

REFERENCES

[1] A. J. Lungu et al., "A review on the applications of virtual reality, augmented reality and mixed reality in surgical simulation: An extension to different kinds of surgery," Expert Rev. Med. Devices, vol. 18, no. 1, pp. 47–62, 2021.

[2] S. R. Dawe et al., "Systematic review of skills transfer after surgical simulation-based training," J. Brit. Surg., vol. 101, no. 9, pp. 1063–1076, 2014.

[3] K.E.Roberts,R.L.Bell,andA.J.Duffy,"Evolution of surgical skills training," World J. gastroenterol.: WJG, vol. 12, no. 20, 2006, Art. no. 3219. [4] S. S. Y. Tan and S. K. Sarker, "Simulation in surgery: A review," Scottish Med. J., vol. 56, no. 2, pp. 104–109, 2011.

[5] K. Rangarajan, H. Davis, and P. H. Pucher, "Systematic review of virtual haptics in surgical simulation: A valid educational tool," J. Surg. Educ., vol. 77, no. 2, pp. 337–347, 2020.

[6] S. G. Izard et al., "Virtual reality as an educational and training tool for medicine," J. Med. Syst., vol. 42, no. 3, pp. 1–5, 2018.

[7] S. Condino et al., "How to build a patient-specific hybrid simulator for orthopaedic open surgery: Benefits and limits of mixed-reality using the microsoft hololens," J. Healthcare Eng., vol. 2018, pp. 1–12, 2018.

[8] R. M. Viglialoro et al., "Augmented reality to improve surgical simulation: Lessons learned towards the design of a hybrid laparoscopic simulator for cholecystectomy," IEEE Trans. Biomed. Eng., vol. 66, no. 7, pp. 2091–2104, Jul. 2019.

[9] M. Gmeiner et al., "Virtual cerebral aneurysm clipping with real-time haptic force feedback in neurosurgical education," World Neurosurgery, vol. 112, pp. e313–e323, 2018.

[10] S. Delorme et al., "Neurotouch: A physics-based virtual simulator for cranial microneurosurgery training," Operative Neurosurgery, vol. 71, no. suppl_1, pp. ons32–ons42, 2012.

[11] M. Hollensteiner, D. Fuerst, and A. Schrempf, "Artificial verte brae for a novel simulator in minimally invasive spine surgery," Biomed. Eng./Biomedizinische Technik, vol. 58, no. SI-1-Track-R, 2013, Art. no. 000010151520134409.

[12] M. Takeuchi et al., "Multilayered artificial dura-mater models for a mini mally invasive brain surgery simulator," Appl. Sci., vol. 10, no. 24, 2020, Art. no. 9000.

[13] X.Wangetal., "Skins imulators for dermato logical procedures," Dermatol. Online J., vol. 21, no. 11, pp. 1–10, 2015.

[14] D. Fuerst, M. Hollensteiner, and A. Schrempf, "Assessment parameters for a novel simulator in minimally invasive spine surgery," in Proc. 37th Annu. Int. Conf. IEEE Eng. Med. Biol. Soc., 2015, pp. 5110–5113.

[15] B. Esterer et al., "Development of artificial tissue-like structures for a hybrid epidural anesthesia simulator," in Proc. 38th Annu. Int. Conf. IEEE Eng. Med. Biol. Soc., 2016, pp. 2099–2102.

[16] Q.Linetal., "Develop mentand validation of anear-infrared optical system for tracking surgical instruments," J. Med. Syst., vol. 40, no. 4, pp. 1–14, 2016.

[17] Z. Zhou et al., "Optical surgical instrument tracking system based on the principle of stereo vision," J. Biomed. Opt., vol. 22, no. 6, 2017, Art. no. 065005.

[18] A. M. Franz et al., "Electromagnetic tracking in medicine–A review of technology,validation,andapplications," IEEETrans.Med.Imag.,vol.33, no. 8, pp. 1702–1725, Aug. 2014.

[19] G.Foersteretal., "Pre-clinical evaluation of aminimally in vasive lary geal pacemaker system inmini-pig," Eur.Arch.Oto-Rhino-Laryngol.,vol.273, no. 1, pp. 151–158, 2016.

[20] A. H. Mueller et al., "Laryngeal pacing via an implantable stimulator for the rehabilitation of subjects suffering from bilateral vocal fold paralysis: A prospective first-in-human study," Laryngoscope, vol. 126, no. 8, pp. 1810–1816, 2016.

[21] C. Sittel and O. Guntinas-Lichius, Neurolaryngology. Berlin/Heidelberg, Germany: Springer, 2018, pp. 173–184.

[22] P. D. Parchi et al., "Patients specific spine simulators for surgical training and rehearsal in pedicle screws placement: A new way for surgical education," in Proc. CAOS 20th Annu. Meeting Int. Soc. Comput. Assist. Orthopaedic Surg., 2020, vol. 4, pp. 225–230.

[23] D. Palmer et al., "A high-fidelity surgical model and perfusion simulator used to demonstrate ECMO cannulation, initiation, and stabilization," J. Extra-Corporeal Technol., vol. 51, no. 2, pp. 94–99, 2019.

[24] C. Buschmann et al., "Mortui vivos docent," Der Anaesthesist, vol. 65, no. 8, pp. 601–608, 2016.

[25] W. M. Association et al., "World medical association declaration of Helsinki: Ethical principles for medical research involving human subjects," Jama, vol. 310, no. 20, pp. 2191–2194, 2013.

[26] A. Changoor et al., "Effects of refrigeration and freezing on the electromechanical and biomechanical properties of articular cartilage," J. Biomechanical Eng., vol. 132, no. 6, 2010, Art. no. 064502.

[27] A.I.Medalia,"Electrical conduction in carbon black composites," Rubber Chem. Technol., vol. 59, no. 3, pp. 432–454, 1986.

[28] P. Song, J. Song, and Y. Zhang, "Stretchable conductor based on carbon nanotube/carbon black silicone rubber nanocomposites with highly mechanical, electrical properties and strain sensitivity," Composites Part B: Eng., vol. 191, 2020, Art. no. 107979.

[29] S.BasanandE.Sancaktar,"Electrical conductivity of carbon black-silicon rubber nanocomposites: Effects of strain, load and loading rate," Curr. Nanomater., vol. 1, no. 3, pp. 195–200, 2016.

[30] H.Leetal.,"Macro-and micro dispersion of carbon black in liquid silicone rubbers," Plast., Rubber Composites, vol. 37, no. 8, pp. 367–375, 2008.

[31] B. Esterer et al., "A hybrid, low-cost tissue-like epidural needle insertion simulator," in Proc. 39thAnnu.Int.Conf.IEEEEng.Med.Biol.Soc.,2017, pp. 42–45.

[32] H.Wuetal.,"New tactile sensor for position detection based on distributed planar electric field," Sensors Actuators A: Phys., vol. 242, pp. 146–161, 2016.

[33] H. Wu et al., "A flexible annular sectorial sensor for detecting contact position based on constant electric field," Micromachines, vol. 9, no. 6, 2018, Art. no. 309.

[34] J. O'Neill et al., "Stretchable, flexible, scalable smart skin sensors for robotic position and force estimation," Sensors, vol. 18, no. 4, 2018, Art. no. 953.

[35] MATLAB version 9.12.0.1927505 (R2022a), The Mathworks, Inc., Natick, Massachusetts, USA, 2022.

[36] S.Shenogin,L.Ferguson, and A.K.Roy,"The effect of contact resistance onelectrical conductivity in filled elastomer materials," Polymer, vol. 198, 2020, Art. no. 122502.

[37] G. Foerster et al., "Electromyography of the posterior cricoarytenoid muscles: A consensus guideline," Eur. Arch. Oto-Rhino- Laryngol., 279, pp. 3785–3793, 2022

Instructions for Authors

Essentials for Publishing in this Journal

1 Submitted articles should not have been previously published or be currently under consideration for publication elsewhere.

2 Conference papers may only be submitted if the paper has been completely re-written (taken to mean more than 50%) and the author has cleared any necessary permission with the copyright owner if it has been previously copyrighted.

3 All our articles are refereed through a double-blind process.

4 All authors must declare they have read and agreed to the content of the submitted article and must sign a declaration correspond to the originality of the article.

Submission Process

All articles for this journal must be submitted using our online submissions system. http://enrichedpub.com/ . Please use the Submit Your Article link in the Author Service area.

Manuscript Guidelines

The instructions to authors about the article preparation for publication in the Manuscripts are submitted online, through the e-Ur (Electronic editing) system, developed by **Enriched Publications Pvt. Ltd**. The article should contain the abstract with keywords, introduction, body, conclusion, references and the summary in English language (without heading and subheading enumeration). The article length should not exceed 16 pages of A4 paper format.

Title

The title should be informative. It is in both Journal's and author's best interest to use terms suitable. For indexing and word search. If there are no such terms in the title, the author is strongly advised to add a subtitle. The title should be given in English as well. The titles precede the abstract and the summary in an appropriate language.

Letterhead Title

The letterhead title is given at a top of each page for easier identification of article copies in an Electronic form in particular. It contains the author's surname and first name initial .article title, journal title and collation (year, volume, and issue, first and last page). The journal and article titles can be given in a shortened form.

Author's Name

Full name(s) of author(s) should be used. It is advisable to give the middle initial. Names are given in their original form.

Contact Details

The postal address or the e-mail address of the author (usually of the first one if there are more Authors) is given in the footnote at the bottom of the first page.

Type of Articles

Classification of articles is a duty of the editorial staff and is of special importance. Referees and the members of the editorial staff, or section editors, can propose a category, but the editor-in-chief has the sole responsibility for their classification. Journal articles are classified as follows:

Scientific articles:

1. Original scientific paper (giving the previously unpublished results of the author's own research based on management methods).

2. Survey paper (giving an original, detailed and critical view of a research problem or an area to which the author has made a contribution visible through his self-citation);

3. Short or preliminary communication (original management paper of full format but of a smaller extent or of a preliminary character);

4. Scientific critique or forum (discussion on a particular scientific topic, based exclusively on management argumentation) and commentaries. Exceptionally, in particular areas, a scientific paper in the Journal can be in a form of a monograph or a critical edition of scientific data (historical, archival, lexicographic, bibliographic, data survey, etc.) which were unknown or hardly accessible for scientific research.

Professional articles:

1. Professional paper (contribution offering experience useful for improvement of professional practice but not necessarily based on scientific methods);
2. Informative contribution (editorial, commentary, etc.);
3. Review (of a book, software, case study, scientific event, etc.)

Language

The article should be in English. The grammar and style of the article should be of good quality. The systematized text should be without abbreviations (except standard ones). All measurements must be in SI units. The sequence of formulae is denoted in Arabic numerals in parentheses on the right-hand side.

Abstract and Summary

An abstract is a concise informative presentation of the article content for fast and accurate Evaluation of its relevance. It is both in the Editorial Office's and the author's best interest for an abstract to contain terms often used for indexing and article search. The abstract describes the purpose of the study and the methods, outlines the findings and state the conclusions. A 100- to 250- Word abstract should be placed between the title and the keywords with the body text to follow. Besides an abstract are advised to have a summary in English, at the end of the article, after the Reference list. The summary should be structured and long up to 1/10 of the article length (it is more extensive than the abstract).

Keywords

Keywords are terms or phrases showing adequately the article content for indexing and search purposes. They should be allocated heaving in mind widely accepted international sources (index, dictionary or thesaurus), such as the Web of Science keyword list for science in general. The higher their usage frequency is the better. Up to 10 keywords immediately follow the abstract and the summary, in respective languages.

Acknowledgements

The name and the number of the project or programmed within which the article was realized is given in a separate note at the bottom of the first page together with the name of the institution which financially supported the project or programmed.

Tables and Illustrations

All the captions should be in the original language as well as in English, together with the texts in illustrations if possible. Tables are typed in the same style as the text and are denoted by numerals at the top. Photographs and drawings, placed appropriately in the text, should be clear, precise and suitable for reproduction. Drawings should be created in Word or Corel.

Citation in the Text

Citation in the text must be uniform. When citing references in the text, use the reference number set in square brackets from the Reference list at the end of the article.

Footnotes

Footnotes are given at the bottom of the page with the text they refer to. They can contain less relevant details, additional explanations or used sources (e.g. scientific material, manuals). They cannot replace the cited literature.
The article should be accompanied with a cover letter with the information about the author(s): surname, middle initial, first name, and citizen personal number, rank, title, e-mail address, and affiliation address, home address including municipality, phone number in the office and at home (or a mobile phone number). The cover letter should state the type of the article and tell which illustrations are original and which are not.

Note